

HOT STARS IN THE ULTRA METAL-POOR BLUE COMPACT DWARF GALAXY I Zw 18

MASTER THESIS

Ángela Abad Martín

Contact:

angela.abad2000@gmail.com
anab2425@student.su.se

Supervisor: Göran Östlin
Co-Supervisor: Giacomo Bortolini

July 1, 2025



Stockholm University
Astronomy Department, Galaxy Group

Contents

Abstract	1
1 Introduction	2
2 Theoretical Framework	4
2.1 Background on Dwarf Galaxies	4
2.1.1 Early Type Dwarf Galaxies	5
2.1.2 Late Type Dwarf Galaxies	6
2.2 The Relevance of Metallicity	7
2.3 I Zw 18 and its Companion	7
2.4 Fundamentals of Color-Magnitude Diagrams (CMDs)	9
2.5 Effects of Dust Extinction	10
3 Observations and Methodology	11
3.1 Previous Studies and Current Observational Setup	11
3.2 PSF Photometric Analysis	12
3.2.1 DOLPHOT 2.0 and Catalog Compilation	13
3.3 Data Filtering	15
3.3.1 Region Characterization	15
3.3.2 Parameter Culling	17
4 Color-Magnitude Diagram (CMD) Analysis	19
4.1 Artificial Star Tests: Setup and Purpose	20
4.2 CMDs	23
4.3 Isochrones and Evolutionary Tracks	27
4.3.1 Isochrone Fitting: MIST and PARSEC Models	27
4.3.2 MIST Isochrones Rotation Fitting	30
4.3.3 MIST Evolutionary Tracks Fitting	31
4.4 CMD Segmentation: He-burning (HeB) Stars	32
5 Color-Color Diagrams (CCDs)	37
6 Star Formation Histories (SFHs)	43
7 Conclusions and Future Work	52
Acknowledgements	56
Appendix	56
References	57

Abstract

Throughout this thesis we investigate the distant blue compact dwarf galaxy I Zw 18. Known for its densely packed stellar population, notable ongoing star formation, and metallicity deficiency, I Zw 18 has been extensively analyzed in previous studies, serving as a perfect laboratory for understanding star formation and evolution in galaxies resembling primordial systems in the early Universe.

In this work, we principally focus on the detection and examination of the bluest, youngest stars within the galaxy. This is accomplished using HST/WFC3/UVIS data retrieved from the GO program 17129 (PI: G. Östlin), targeting the UV/blue part of the spectrum. Utilizing point-spread function (PSF) photometry with the DOLPHOT2.0 software, we performed color-magnitude diagram (CMD) analyses using filters F225W and F438W where we conducted isochrone and evolutionary track fitting adopting MIST and PARSEC models. We ended up revealing a resolved stellar population with an age span from $\approx (2.5 - 40)$ Myr and a characteristic clump of bright stars with masses up to $\approx 140 M_{\odot}$, including potential Wolf Rayet (WR) star candidates. Further analyses were carried out on the spatial distribution of stars within I Zw 18's main body and its companion galaxy, Component C. Distinct patterns were identified, with the youngest stellar populations concentrating in the northwest (NW; Population A) and southeast (SE; Population C) areas – characterized with the highest star formation rates (SFRs) – and the slightly more evolved populations distributed around the outskirts. Component C was characterized as missing the youngest and brightest stellar component present in I Zw 18.

Reddening effects by dust were additionally evaluated through color-color diagrams (CCDs) by introducing a third filter (F336W) and through the application of the Milky Way (MW) and Small Magellanic Cloud (SMC) extinction laws. We confirmed that a modest and relatively uniform internal extinction was present within the main target, with a typical A_V value ranging from ≈ 0.1 (for those stars solely affected by the foreground reddening) to ≈ 0.25 (those affected by an intrinsic extinction value).

Finally, we reconstructed the recent star formation histories (SFHs) of I Zw 18, Component C and Populations A and C, through the implementation of a synthetic CMD fitting routine called SFERA2.0. While the observational and modeled CMDs were in overall agreement, fitting challenges were evident – especially the most massive stellar clump, the reddest sources or those laying around the MS area of the isochrones were difficult to model, mainly due to completeness corrections, crowding effects and reddening assumptions. The SFHs indicate a strong burst in I Zw 18 over the last ≈ 10 Myr, with the most recent activity occurring in the NW region, followed by the SE area. This supports the idea that this stellar outburst could be driven by pristine in-falling gas from its companion, which itself shows signs of a relatively older stellar population and a decline in stellar formation for the past 10 Myr.

Future work could benefit from spectral energy distribution (SED) fitting to better constrain the intrinsic stellar parameters of the brightest, bluest stellar clumps. Further analysis of the SFHs of the galaxy, as well as its inner spatial regions, could be developed to ensure for more consistent models and better fitted results.

Keywords: Color-Magnitude Diagram (CMD) – Galaxy: dwarf, evolution, star formation – Point Spread Function (PSF) Photometry – Reddening – Star Formation History (SFH)

1. Introduction

Star-forming galaxies (SFGs) are defined by their active stellar formation at the time of observation. This process relies on the availability of cold gas, particularly molecular hydrogen (H_2), which serves as the primary fuel for star formation. Among SFGs, those with a stellar mass $M_\star < (10^8 - 10^9) M_\odot$ are classified as dwarf galaxies (Tolstoy (2009), Cimatti et al. (2019), Diehl et al. (2022)). Despite their relatively low mass, these galaxies are abundant and widespread throughout the Universe (Annibali & Tosi (2022)). This is reflected in the galaxy luminosity function ($\phi(L)$), which indicates that low-luminosity galaxies are exponentially more common than bright massive ones (Cimatti et al. (2019)). Dwarf galaxies influence is rooted in the early stages of cosmological evolution. Following the Epoch of Recombination ($z \approx 1000$), when the Universe transitioned from a fully ionized plasma to neutral gas, matter and radiation decoupled, giving rise to the cosmic microwave background (CMB) radiation. As the Universe continued to cool, gravitational collapse led to the formation of the first luminous sources ($z \approx (20 - 30)$). These early dwarf galaxies, characterized by low metallicity and intense ultraviolet (UV) emission, began enriching and ionizing the surrounding intergalactic medium (IGM), marking the beginning of the Epoch of Reionization (EoR) (Longair (2008); Giallongo et al. (2015); Cimatti et al. (2019)).

As a consequence, dwarf galaxies are usually considered as part of the main contributors to the EoR and the precursors to larger and more complex structures. Therefore, they could contribute to the identification of mechanisms that shape galactic evolution (Annibali & Tosi (2022)). Among dwarf galaxies, those that exhibit recent starburst activity and have a luminosity below $M_B \approx -17$ (Kunth & Östlin (2000)) are classified as blue compact dwarfs (BCDs). This is the case of I Zw 18 (also known as Markarian 116), first identified by Swiss astronomer Fritz Zwicky in 1966 (Zwicky (1966), Kunth & Östlin (2000)). It was initially classified as a dwarf irregular galaxy and, after the author coined the term "compact galaxies" in his work Zwicky (1965), I Zw 18 was introduced as number 18 in his first "*Catalogue of Selected Compact Galaxies and of Post-Eruptive Galaxies*" (Zwicky & Zwicky (1971)), hence its name.

I Zw 18 is located at a distance of $D = (18.2 \pm 1.5)$ Mpc, equivalent to a distance modulus of $(m - M)_0 = (31.30 \pm 0.17)$ mag (Aloisi et al. (2007)), and still holds the record of the most distant galaxy with a star formation history (SFH) derived from the color-magnitude diagram (CMD) of its resolved stellar populations (Annibali & Tosi (2022)). It is identified for presenting an extremely high star formation rate (SFR) for its mass, as high as $\approx 1 M_\odot/\text{yr}$ in its most crowded region (northwest (NW) clump in Figure 1) (Searle & Sargent (1972), Annibali et al. (2013)). Furthermore, I Zw 18 is characterized by a low dynamical mass of the order of $(2 - 3) \cdot 10^8 M_\odot$ (Petrosian et al. (1995); Lelli et al. (2012); Annibali et al. (2013)) and a high fraction of highly ionized gas, which constitutes approximately 70% of its total mass (Annibali et al. (2013)). These characteristics have led to its frequent comparison with primordial high-redshift galaxies. Moreover, its exceptionally low metal abundance, ranging between $(1/30) Z_\odot$ and $(1/50) Z_\odot$ (Searle & Sargent (1972), Skillman & Kennicutt (1993), Bortolini et al. (2024b) and references therein), causes it to be categorized as an extremely metal-poor (XMP) dwarf. This range in metallicity is not associated with variations in I Zw 18 but rather with changes in the solar reference oxygen abundance – which has been modified over the past years (e.g. see Anders & Grevesse (1989), Asplund et al. (2004)), most recently varying from $12 + \log(O/H) = 8.76 \pm 0.02$ (Steffen et al. (2015)) to $12 + \log(O/H) = 8.80 \pm 0.03$ (Armas et al. (2020)). Consequently, based on the comparison between I Zw 18 and the solar reference value, it seems reasonable to state that our target has an oxygen abundance of around $3\% Z_\odot$. According to Skillman & Kennicutt (1993), I Zw 18 was classified as having the smallest fraction of metals estimated among all SFGs studied in the nearby Universe. Some more recent studies, as in the case of Izotov et al. (2018), show that its most crowded and luminous region (NW) ranks as the fifth lowest in oxygen abundance ($12 + \log(O/H) = 7.16 \pm 0.01$). Overall, I Zw 18 is classified among the most metal-poor SFGs known.

Recent studies on I Zw 18 by Bortolini et al. (2024b) focus on the evolutionary history of the galaxy using high-resolution infrared images from the James Webb Space Telescope near-infrared camera (JWST/NIRCam). Through CMDs and state-of-the-art point spread function (PSF) photometry techniques using DOLPHOT 2.0 (see Section 3.2.1 for reference), they analyze the galaxy's stellar populations and reconstruct its SFH over the past billion years. While previous studies suggested that I Zw 18 might be a newly-born young galaxy (Sargent & Searle (1970), Searle & Sargent (1972), Izotov & Thuan (2004)) or an old one (Aloisi et al. (1999); Östlin (2000)) with slow star formation ("slow cooking scenario"; see Legrand et al. (2000, 2001); Aloisi et al. (2007); Ramos et al. (2011); Annibali et al. (2013)), the findings in Bortolini et al. (2024b) reveal a low SFR for most of the galaxy's history, followed by two recent outbursts, likely triggered by gravitational interactions with its satellite galaxy, Component C (see Figure 1 for reference).

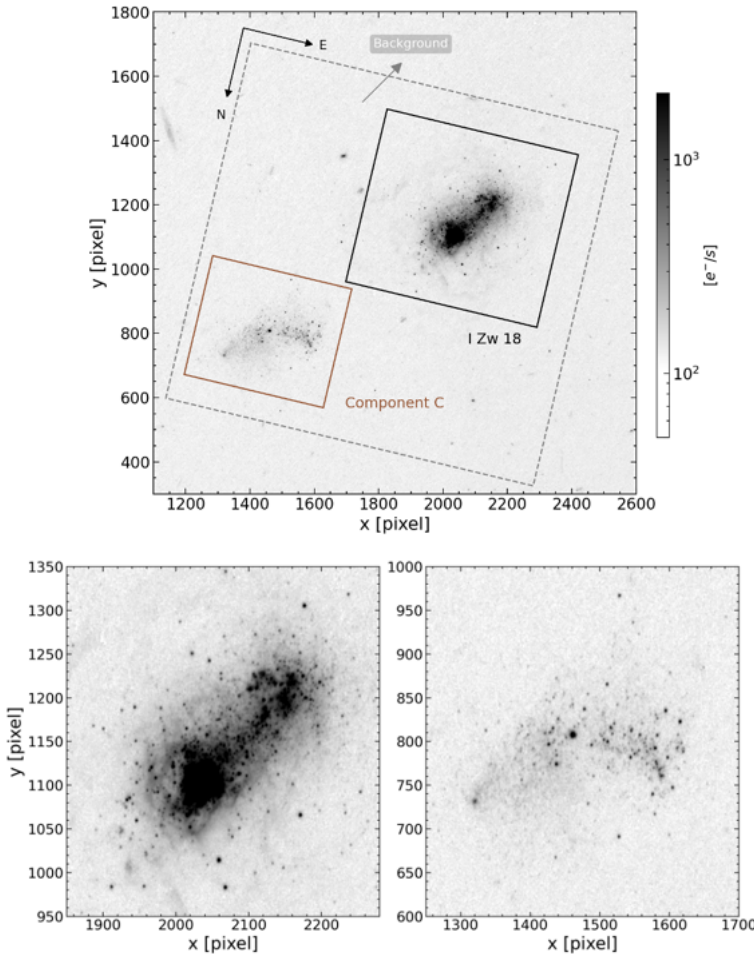


Figure 1: Top panel: HST/WFC3/UVIS F438W drizzled reference image cutout showing I Zw 18's main body (black box), its galactic companion Component C (brown box) and the background area (gray dashed box). The northwest (NW) and southeast (SE) regions within I Zw 18 (most densely populated) correspond to the starburst areas. Bottom panels: zoom on I Zw 18 (left) and Component C (right).

This project is driven by the exciting opportunity to study I Zw 18, a unique galaxy whose unusual properties make it a valuable laboratory for understanding stellar and galactic evolution in metal-poor environments, similar to the extreme conditions in the early Universe. It builds upon the work of Bortolini et al. (2024b) but focuses on the young, hot blue stars in I Zw 18. Past studies of the galaxy carried out with the Hubble

Space Telescope (HST) (see [Izotov & Thuan \(2004\)](#), [Aloisi et al. \(2007\)](#)) focused on the age and distance of the target, utilizing the V and I-bands for detecting the old red giant branch (RGB) stars. While ideal for this purpose, they had limited power for characterizing young, blue massive stars. Consequently, new deep imaging in the UV and blue part of the spectrum is required. Thus, here we employ new data obtained with HST using the Wide Field Camera 3 (WFC3) ultraviolet and visible (UVIS) light detector (program 17129; PI: G. Östlin). This enables us to gain a clearer view of the galaxy's recent SFH ($\approx (1 - 60)$ Myr ago), specifically targeting its youngest stellar populations. Additionally, valuable insights into the effects of dust extinction and reddening, and potential interactions between the main body and its companion are inferred.

This project is structured as follows. Section 2 outlines the scientific foundation, including background theory on dwarf galaxies, galactic metallicity, our main target I Zw 18 and the fundamentals of CMDs and dust extinction. Section 3 details the implemented methodology, starting with an overview of the previous research done on the field regarding I Zw 18 and followed by the procedure undertaken to obtain the photometric dataset used for this project, with the application of the software DOLPHOT 2.0 and the description of the construction and filtering process of our photometric catalog based on parameter and region selections. Section 4 presents the analyses of the CMDs performed throughout the thesis, including artificial star tests, isochrone and evolutionary track modeling and a study of the spatial distribution of the helium-burning (HeB) phase stars. Color-color diagrams (CCDs) are presented in Section 5 to further explore reddening laws and infer, from reddening vectors, the effects of dust extinction within our galaxy. Section 6 is reserved for a preliminary analysis of synthetic CMDs with the use of the routine SFERA 2.0 (see [Bortolini et al. \(2024b\)](#)) to determine the SFH of I Zw 18 and its companion. Finally, Section 7 provides a discussion of the main results and suggestions for future work.

2. Theoretical Framework

2.1. Background on Dwarf Galaxies

Galaxies are complex gravitationally bound systems composed of stars and stellar remnants, interstellar gas and dust and a dominant component of dark matter. They formed through a sequence of evolutionary stages that began soon after the Big Bang and following the era of recombination, where dark matter and neutral gas provided the foundation for the formation of the first luminous sources, initiating the gradual build-up of galaxies ([White & Rees \(1978\)](#), [Frenk et al. \(1988\)](#), [White & Frenk \(1991\)](#), [Kravtsov et al. \(2004\)](#), [Cimatti et al. \(2019\)](#)).

Among them, dwarf galaxies are particularly significant. They represent the most numerous, dominant type of galaxy in the Universe based on cold dark matter (CDM) cosmology ([White & Rees \(1978\)](#)) and observations ([Kravtsov et al. \(2004\)](#)), presenting a wide range of morphologies and having been defined in multiple different ways by scientists throughout history. Their low luminosities (hindering their detections), highly environment-influenced nature and wide variety of configurations and properties (some of which are overlapped with neighbor companions) are only some of the reasons why their categorization still remains a subject of ongoing debate within the scientific community ([Sacchi et al. \(2018\)](#)). As a result, this makes them difficult to be classified in a consistent and universally accepted manner. According to [Tolstoy \(2009\)](#), a reasonable approach when characterizing dwarf galaxies is by taking into consideration their ability to retain baryonic mass – that is, everything including their gas, dust and stellar component. [Annibali & Tosi \(2022\)](#) defines dwarf galaxies as systems with baryonic masses not exceeding $10^9 M_{\odot}$. This is due to the fact that dwarf galaxies form within inherently low-mass dark matter halos, which have shallower potential

wells. These, in turn, make it more difficult for dwarf galaxies – which already present relatively low baryonic content from the beginning – to retain it when exposed to feedback processes such as the effects of supernova (SN) winds and/or tidal interactions. As a consequence, these can potentially reduce their baryonic mass even more over time (Tolstoy (2009), Cimatti et al. (2019)). Figure 2 shows the comparison between the morphological classes in dwarf galaxies with those of other galaxy types in the surface brightness-luminosity plane. As we can see, dwarf galaxies span a well-fitted linear sequence, from the lower right area (faint and diffuse) towards the central part (brighter and more compact). Near the central part of the diagram we also find late-type disk and spiral galaxies. Towards the upper-left side there are giant ellipticals while globular clusters can be found in the right region of the plot.

A common and straightforward approach is to categorize dwarf galaxies based on two main features: their stellar activity and/or their morphological characteristics. Based on stellar activity, we can distinguish between star-forming galaxies (SFGs) or passive/quenched galaxies. On the other hand, according to morphology dwarf galaxies can be classified as early-type (ET) or late-type (LT) galaxies (Cimatti et al. (2019), Annibali & Tosi (2022)).

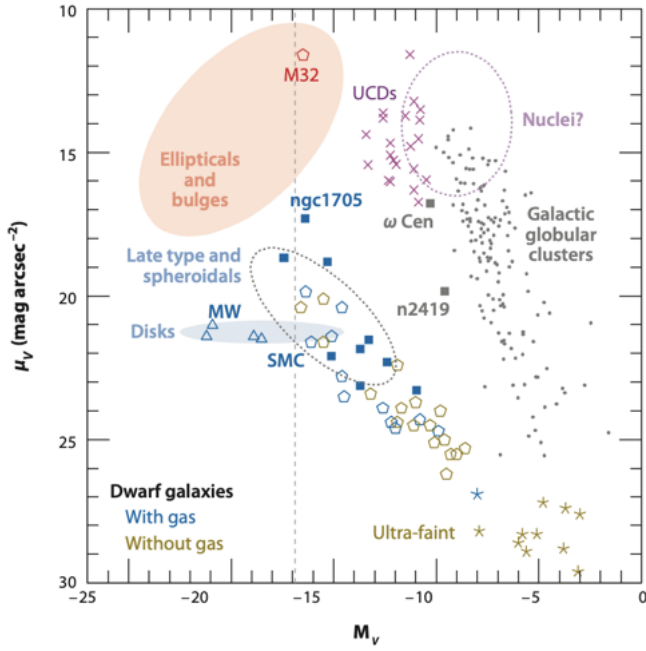


Figure 2: Adapted figure from Tolstoy (2009), representing the various galaxy types based on their central surface brightness (μ_V) compared to their absolute magnitudes (M_V) in the V-band. The dashed line indicates the dwarf galaxy limit, as defined in Tolstoy (2009).

2.1.1. Early Type Dwarf Galaxies

ET dwarf galaxies tend to present weak or absent star formation, little cold gas and the lack of stellar discs and spiral arms. They can be classified according to their morphologies into three different types: dwarf spheroidals (dSphs), dwarf ellipticals (dEs) or ultra faint dwarfs (UFDs) (see Figure 3). dSphs present a uniform rounded structure and are usually characterized by being faint and diffuse, with little gas reservoir. dEs, on the other hand, present more compact configurations and appear relatively luminous although still poor when it comes to recent stellar formation. Furthermore, UFDs have been recently discovered by Simon & Geha (2007) and represent the faintest and smallest dwarf galaxies, some even containing only a few

hundred stars. These latter ones share properties with the previous categories analyzed, such as the lack of gas, although UFDs tend to be several magnitudes fainter (Cimatti et al. (2019)).

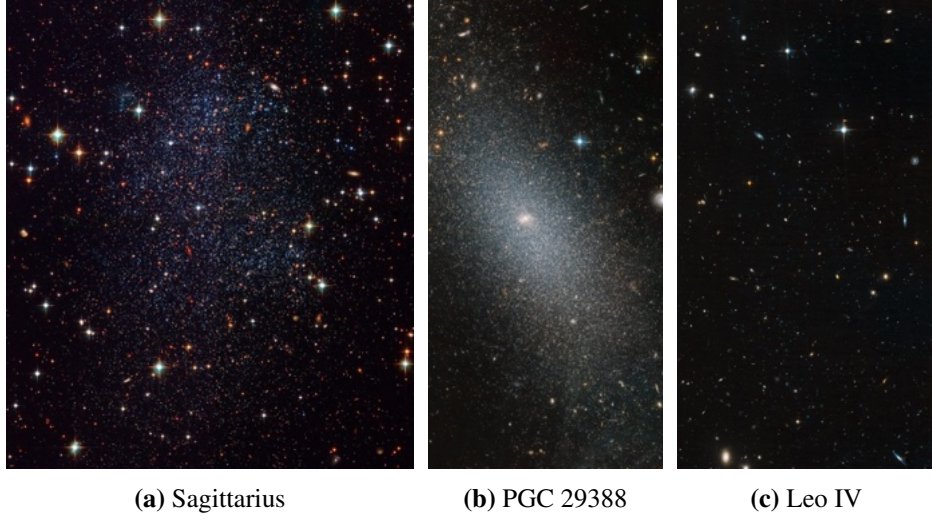


Figure 3: Examples of ET dwarf galaxies: (a) dSph, (b) dE and (c) UFD. Images retrieved from the official NASA website.¹

2.1.2. Late Type Dwarf Galaxies

On the other hand, most LT dwarf galaxies are characterized for presenting ongoing star formation and can be categorized as dwarf irregulars (dIrrs) or blue compact dwarfs (BCDs) (see Figure 4). According to Cimatti et al. (2019), BCDs and dIrrs are thought to be different manifestations of the same family of galaxies since their most evident difference is that BCDs have a star formation activity, both in total rate and in spatial concentration, which is significantly more elevated than that of dIrrs. We can also interpret dIrrs as gas-rich dSphs – i.e. dSphs resemble dIrrs that have lost their gas – although more disk-like in shape.

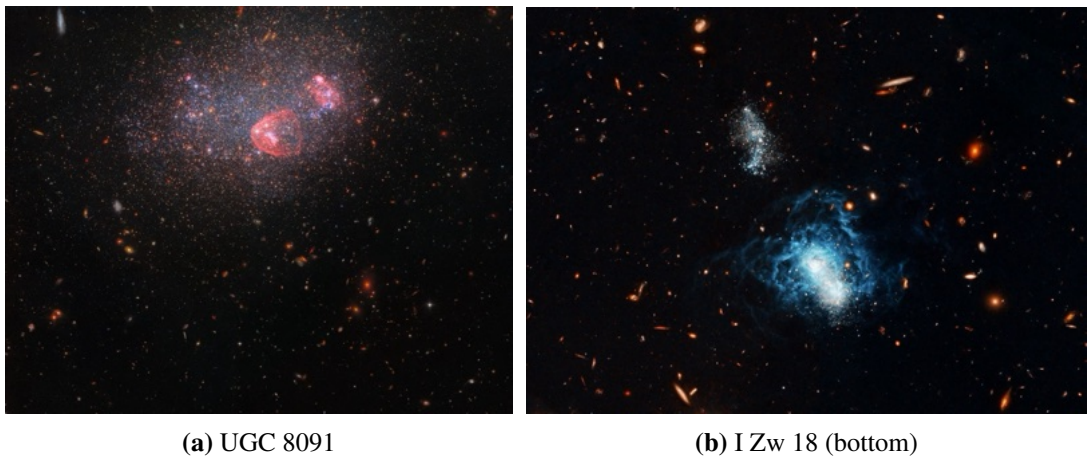


Figure 4: Examples of LTDGs: (a) dIrr and (b) BCD. Images retrieved from the official NASA website.¹

¹<https://www.nasa.gov>

2.2. The Relevance of Metallicity

In astronomy, the chemical elements heavier than hydrogen (H) and helium (He) are referred to as metals (Z). The bulk of metals are synthesized by massive stars during their evolutionary phases. For those stars with masses $M_\star \gtrsim 8 M_\odot$, the culmination of their short lifespans is marked by SN explosions, through which the nucleosynthetic byproducts are dispersed into the surrounding gas (Ferrara (2016), Goswami et al. (2022)). Other ways in which the interstellar medium (ISM) can be enriched is through the stellar winds of the most massive and evolved stars (Woosley et al. (2002)) (see Section 2.3).

According to authors such as Wheeler et al. (1989), Marigo (2001) and Hirschauer et al. (2024), the chemical enrichment history of a galaxy reflects the gradual accumulation of heavy elements through successive cycles of stellar feedback. That is, the metal production of the current stellar population in a galaxy is influenced by the contributions of the prior generation. This means that not only the cold gas is relevant and related to star formation but also metallicity has a strong impact. When gas clouds collapse under the effect of a gravitational potential, they are heated up. According to Smith et al. (2008), the presence of metals increases the number of available atomic and molecular transitions, which consequently releases energy in the form of radiation, cooling the gas and enhancing stellar formation. In the case of low-metallicity environments, star formation does not simply stop. Instead, what happens is that cooling becomes generally less efficient. However, it is important to recall that other factors – i.e. turbulence (generating density pockets of gas that can collapse to form stars) or even the presence of H₂ (radiating energy through vibrations and rotations, cooling down the gas) – also influence star formation, making the process more complex. Furthermore, hydrodynamical simulations have shown that star formation in very low-metallicity environments is expected to generate stars of the order of $M_\star \approx 100 M_\odot$, as evidenced by Lamers (2005). This is supported by Smith et al. (2008), who states that fragmentation is more prone to occur when the gas can both dissipate heat faster than the time it would take the system to collapse under its own gravitational pull – also known as dynamical time – and when it is thermally unstable. Metal-rich environments with low densities and temperatures trigger the formation of these instabilities, which means that scenarios like that of I Zw 18, with metal abundances ranging between [1/30, 1/50] Z_⊙, challenge our current understanding of star formation. For all the reasons stated above, metals are considered to play a crucial role in the process of star formation.

On the other hand, it is important to state that the galactic metallicity depends on the regions of study. This means that the metal content of the gas component usually differs from the metallicities of the galaxy's stellar population (Kunth & Östlin (2000)). Besides, within the gas we can find different phases with varying metal compositions, as stated in Lebouteiller et al. (2013). Their study shows that in BCDs, most chemical analysis focus on the ionized gas of the H_{II} regions – close to where star formation occurs. However, neutral gas regions (H_I) represent a greater fraction of the galaxy in terms of mass and reflect its long-term enrichment history. Therefore, the authors suggest that comparing both regions provides insights into the spread of heavy elements and their influence in star formation.

2.3. I Zw 18 and its Companion

As already introduced in Section 1, I Zw 18 has long intrigued astronomers as a rare and extreme laboratory for studying star formation and chemical evolution under conditions reminiscent of the early Universe. However, its distance (at around 18 Mpc away from the Milky Way (MW)) places it outside of the Local Group (≈ 1 Mpc in size; Cimatti et al. (2019)), making it even more affected by crowding effects and consequently more challenging when resolving its stellar population (Tolstoy (2009)).

Interest in BCDs like I Zw 18 began with the study of Sargent & Searle (1970), where they identified its spectrum as being dominated by strong emission lines from ionized gas and an exceptionally low metallicity.

This led them to suggest that this galaxy could be genuinely young, undergoing its first major episode of star formation. However, recent observations by Bortolini et al. (2024b) have revealed that I Zw 18 harbors an underlying older stellar population, challenging the notion that BCDs are pristine galaxies formed recently. Legrand (1999), on the one hand, remarked that a scenario based on the premise of multiple starburst events followed by metal loss through strong winds was not entirely valid to support the metal-poor abundance feature of I Zw 18. This scenario would imply that the stellar population would appear progressively redder due to the accumulation of older, cooler stars, contrary to indications by observational data where the galaxy is seen as distinctively blue. Consequently, he supported the idea that a mild, continuous mode of star formation – driven by local fluctuations exceeding the density threshold – was a more reliable approach that accounted for the chemical and photometric properties of I Zw 18. Analysis by Bortolini et al. (2024b) recently argued that I Zw 18 actually presented a faint, extended halo of ancient stars. This supported the "slow cooking" dwarf galaxy scenario (Garnett et al. (1997)), where limited but sustained star formation leads to this specific galaxy state. Additionally, Bortolini et al. (2024b) demonstrated through photometric analysis using JWST/NIRCam's data that I Zw 18 is now experiencing its strongest burst of star formation with a SFR of $\approx 0.6 \text{ M}_\odot/\text{yr}$ located in the NW region (see Figure 1 or population A in Figure 7b; check Section 3.3.1 for more information).

The identification of the mechanisms that can initiate these recent strong bursts of star formation, as well as their impact on the galaxy's evolution, is still unclear (Sacchi et al. (2018)). Potential agents contributing to stellar formation have been discussed in previous studies (Lelli et al. (2014)), including tidal interactions and mergers – both related to the gravitational interplay between the system and its host companion, potentially triggering the starburst due to a redistribution of the gas reservoir. Another option is gas accretion – suggesting gas exchange with the surrounding environment. On the other hand, the classification of the mechanisms by which the galaxy, despite presenting recent star formation, remains metal-poor, is still a challenging task where multiple scientists have contributed with suggestions such as stellar winds, SN feedback and galactic outflows (Mac Low & Ferrara (1999), Hopkins et al. (2012)) as well as the inflow of pristine H_I gas (Lebouteiller et al. (2013)).

Another of the peculiarities of I Zw 18 is that the deep spectra of H₂ star-forming regions revealed the presence of Wolf Rayet (WR) stars (Legrand et al. (1997), Izotov et al. (1997)). WR stars are described as being compact sources with high temperatures and luminosities. They are intimately affected by intense stellar winds and their spectra shows broad emission lines (Crowther (2007)). Stellar winds – which contribute to the enrichment of the IGM through the deposition of heavy elements synthesized in evolved stars – depend on the metal abundance in the surrounding medium which, at the same time, influences the composition of the new forming stars (Yoon et al. (2006), Woosley & Heger (2006), Vink & de Koter (2005)). Consequently, in a metal-poor galaxy such as I Zw 18 one would anticipate that there would not be enough heavy elements to generate significant stellar winds. However, the discovery of WR stars in this galaxy implies a significant finding. According to Kunth & Östlin (2000), it was thought that in low-metallicity galaxies ($Z = 1/20 \text{ Z}_\odot$) only massive stars ($M_\star > 80 \text{ M}_\odot$) could reach this stage since they could contribute to sufficiently strong stellar winds compared to lower-mass stars. As a result, these detections offer valuable insights into the formation of massive stars in XMP galaxies and suggest that the initial mass function (IMF) – which describes the distribution of stellar masses during a starburst event at a given location in a galaxy and which typically favors the formation of low-mass stars – may be unusually top-heavy in metal-poor environments, potentially containing a higher fraction of massive stars.

Furthermore, it has been suggested that binary stellar evolution mechanisms may provide a solution to this problem (Kunth & Östlin (2000)). In these systems, the most massive partner can lose its outer H_I envelope to its companion as soon as it overflows its Roche lobe – i.e. the region surrounding the star that is still gravitationally bound to it. However, it seems that this alone might not be enough to explain the strong stellar

wind properties, which is why the formation of WR stars in such low metallicity environments still remains poorly understood (Shenar et al. (2020)).

Besides this, some H _{α} studies – which are generally used to analyze the morphological details within galaxies and as star-formation tracers (Weistrop et al. (1995), Valluri & Anupama (1996)) – demonstrated that there was a separate galaxy at approximately the same redshift as I Zw 18 (Dufour & Hester (1990)) and only a few kpc away (Kunth & Östlin (2000)). This structure was later on confirmed through spectroscopic analysis by Petrosian et al. (1996) and has been commonly referred to as Component C (Bortolini et al. (2024b)). According to van Zee et al. (1998), Component C is positioned within the same H_I cloud as that of I Zw 18, also confirmed by later studies (Lelli et al. (2012)). H_I is distributed around galaxies as highly diffuse in-falling gas, contributing to the system's reservoir and energy balance, and its shielding role positively influences star formation, enabling the necessary conditions for the survival and collapse of molecular hydrogen (H₂), which is why it is considered an essential during star formation (McClure-Griffiths et al. (2023)). Due to all of the above, and although our target in this project is I Zw 18, we place some emphasis on Component C given its close connection with the main body.

2.4. Fundamentals of Color-Magnitude Diagrams (CMDs)

While pinpointing the exact causes of stellar bursts remains challenging, innovations in modern space telescopes with advanced spatial resolution and sensitivity are available to help scientists discern individual point-like sources within a distance of around 20 Mpc (Bortolini et al. (2024a)). When it comes to recovering the stellar populations within galaxies in the Local Volume and estimating their SFHs, we can rely on a powerful tool known as color-magnitude diagram (CMD). According to Cignoni & Tosi (2010), "*The CMD of a stellar system is in fact the best information desk on the system evolution, because it preserves the imprinting of all the relevant evolution parameters (age, mass, chemical composition, initial mass function)*".

CMDs are constructed, as their name suggests, using the colors and magnitudes of the individual stars detected within the galaxy of interest (I Zw 18 in our particular case). Apparent magnitudes (m) represent, on the one hand, measurements of how bright a source is as observed from Earth (the brighter the source, the lower the apparent magnitude and vice-versa). Colors, on the other hand, are defined as the difference in apparent magnitudes between two wavelength filters, as indicated in Eq. 1, where m_{F_{1,2}} represents the apparent magnitude in each filter (F₁ and F₂) and $\mathcal{F}_{F_{1,2}}$ indicates the corresponding detected fluxes. Furthermore, absolute magnitudes (or luminosities) (M) are defined as the apparent magnitudes that sources would have had they been located at a distance of 10 pc (see Eq. 2, where the absolute magnitude for a given "X-filter" (M_{F_X}) is defined with respect to the apparent magnitude detected in that filter (m_{F_X}), the proper distance to the source (d) and the foreground extinction measured in the "X-filter/band" (A_{F_X})). We usually resort to the definition of distance modulus ($\mu = m_{F_X} - M_{F_X}$) as a measure of the distance at which a galaxy is and we will go back to this in the following sections. Additionally, for consistency purposes, during this project we prefer using A _{λ} instead of A_{F_X}. This is merely a question of notation: since every filter we work with is associated with an effective wavelength, A_{F_X} is equivalent to A _{λ} , with $\lambda \equiv F_X$ representing the filter's specific wavelength.

$$\text{color} = m_{F_1} - m_{F_2} = -2.5 \log \left(\frac{\mathcal{F}_{F_1}}{\mathcal{F}_{F_2}} \right) \quad (1)$$

$$M_{F_X} = m_{F_X} - 5 \log \left(\frac{d}{[\text{pc}]} \right) - A_{F_X} \quad (2)$$

CMDs are essential for studying the different stellar populations within galaxies. This is so because they incorporate not only stellar colors – which are subject to strong degeneracies (see Section 6 for further information)– but also stellar brightnesses, providing additional constraints to help disentangle stellar properties (see Section 4). It is true that building CMDs for Local Group dwarf galaxies allows us to define more precise reconstructions of their SFHs, but thanks to the current instrumentation and observational developments we have today we are able to analyze the resolved stellar populations of galaxies outside our local neighborhood, as in the case of I Zw 18.

2.5. Effects of Dust Extinction

Colors and luminosities are some of the most basic properties that can be inferred when detecting a star, and they provide valuable information about the galaxy’s internal properties. This is so because they depend on the ages of the stellar populations and the abundance of heavy elements, among other properties. On average, early-type galaxies tend to have the reddest colors, unlike late-type galaxies, which are bluer due to the presence of younger stellar populations. Nevertheless, dust extinction plays a very relevant and far from trivial role here. Interstellar dust is composed of solid particles distributed throughout the ISM and especially concentrated within molecular and atomic gas clouds. These grains, varying in size, interact to a greater extent with the UV radiation emitted by nearby hot, blue stars – particularly O and B type – and re-emit the energy in the mid-infrared (MIR; smaller grains) and/or the far-infrared (FIR; larger grains). The effect of this is the extinction of starlight since the dust absorbs and scatters short wavelength radiation more efficiently than the longer wavelength one. Consequently, this makes the light that ultimately reaches us appear redder than it originally was emitted. This phenomenon is called reddening and, although present in early-type galaxies, it is stronger in late-type galaxies due to the higher gas and dust content, as well as the active stellar formation present there (Draine (2011), Cimatti et al. (2019)). The specific way in which the extinction varies with respect to wavelength is described by the reddening law and the general tendency is that A_λ decreases with increasing wavelength (at least in the optical regime, as suggested by Stahler & Palla (2008)). Color-excess, on the other hand, is also a useful parameter that indicates the difference between the intrinsic and observed color indices (see Eq. 3, where $(B - V)_{\text{int}}$ and $(B - V)_{\text{obs}}$ follow the exact same form as Eq. 1 but with a varying notation, representing the difference in magnitudes between two filters, and $A_{B,V}$ indicates the extinction in the B and V bands). Additionally, the fiducial ratio between the extinction in the V-band (A_V) and the color excess ($E(B - V)$) is denoted as R_V (see Eq. 4). It represents the slope of the extinction law at visible wavelengths and is a fundamental piece of information when modeling the influence of dust extinction.

$$E(B - V) = (B - V)_{\text{int}} - (B - V)_{\text{obs}} = A_B - A_V \quad (3)$$

$$R_V = \frac{A_V}{E(B - V)} \quad (4)$$

As with CMDs, equal attention must be given to the effects of reddening caused by dust extinction. Taking this into account allows for a more accurate characterization of the physical properties of the stellar population, leading to a much more precise understanding of the galaxy’s structure and evolution (see Section 5).

3. Observations and Methodology

3.1. Previous Studies and Current Observational Setup

Among the earliest analyses of I Zw 18, which has been the subject of numerous extensive studies in the past, Hunter & Thronson Jr (1995) marked a pioneering effort detailing the first CMD of the galaxy's main body based on optical data from HST Wide Field and Planetary Camera 2 (WFPC2²) observations (this instrument provided high resolution images over a relatively wide field of view (FOV) and a wavelength range between (1150 – 11000) Å). They especially focused on broadband images for the examination of the massive stellar population and found a broad main sequence (MS) of massive stars, blue and red supergiants (BSG and RSG, respectively) and found no indication of stars significantly older than the few tens of Myrs characterizing the recent starburst episode. A similar approach was followed by Aloisi et al. (1999). Assuming a distance of 10 Mpc, they suggested an ongoing star formation within the galaxy for the last (0.5 – 1) Gyr and a more recent and intense activity taking place between 15 and 20 Myr ago. Following studies by Östlin (2000) analyzed the galaxy's CMD using HST Near Infrared Camera and Multi-Object Spectrometer (NICMOS³; this instrument covers a wavelength range of (0.8 – 2.5) μm) assuming a distance of 12.6 Mpc. They maintained the idea of I Zw 18 being a rather old system with a population of (10 – 20) Myr of RSGs and an asymptotic giant branch (AGB) ranging between (0.1 – 5) Gyr. We now know that, in all these previous studies, the estimated distance to the galaxy was underestimated. As a consequence, this led to the target being mistakenly considered much older than it really was, overestimating its age (Bortolini et al. (2024b)).

Subsequent CMD studies were performed with HST Advanced Camera for Surveys (ACS⁴) – third-generation instrument offering wide-field coverage, high resolution and UV imaging capabilities. Izotov & Thuan (2004), on the one hand, supported the idea that I Zw 18 was a *bona fide young galaxy* (that is, genuinely young) due to the absence of red giant branch (RGB) stars. They could, on the other hand, prove the presence of blue MS stars with ages \lesssim 30 Myr, BSGs and RSGs (\in (10, 100) Myr) and an older population of AGB stars (\in (100, 500) Myr). Later, Aloisi et al. (2007) showed the presence of RGB stars, from which they inferred a more appropriate distance to the galaxy of $D = (18.2 \pm 1.5)$ Mpc. Subsequent studies, such as Ramos et al. (2011), indicated that the galaxy may contain stars as old as 13 Gyr, alongside populations of intermediate-age and very young stars. They proved the presence of thermally pulsing AGB (TP-AGB) and carbon stars and detected around 20 objects that could potentially be unresolved star clusters.

The most recent study by Bortolini et al. (2024b) takes advantage of JWST⁵, a high-resolution observatory with an unparalleled near-infrared (NIR) sensitivity, useful for the analysis of distant galaxies in greater detail than ever before. Here, they identify three main stellar populations: one associated with the NW region with a population younger than \approx 30 Myr, an intermediate-age stellar population in the SE area ranging between (100 – 800) Myr, and finally an old red population forming a faint stellar halo with ages exceeding 1 Gyr and possibly as ancient as 13.8 Gyr. They observed a steady growth in star formation within the galaxy, with two recent star bursts around 10 and 100 Myr ago.

In this project, we focus on the analysis of the dwarf galaxy I Zw 18 using HST/WFC3/UVIS⁶ images. This instrument offers an improved resolution over a wider FOV compared to earlier data. Furthermore, it provides a broader waveband compared to ACS and the use of the ultraviolet and visible channel (UVIS; (200 – 1000) nm) helps target the UV-blue part of the spectrum. This approach aids in the charac-

²<https://www.stsci.edu/hst/instrumentation/legacy/wfpc2>

³<https://www.stsci.edu/hst/instrumentation/legacy/nicmos>

⁴<https://hst-docs.stsci.edu/acsihb/chapter-1-introduction>

⁵<https://science.nasa.gov/mission/webb/>

⁶<https://esahubble.org/about/general/instruments/wfc3/>

terization of the very young, blue stellar population, a perspective that had not yet been explored and which could shed light into the mechanisms affecting recent star formation, complementing the findings from studies more sensitive to the optical/redder part of the spectrum. This project is developed as part of the GO 17129 program (PI: Göran Östlin), from which we have access to a wide range of images from different filters. In our particular case, we focus primarily on the wide filters F225W, F336W and F438W. Additional images acquired with other filters (F140LP, F469W, F555W, F606W and F814W) are also available to us – the last two being obtained using the HST/ACS detector. Figure 5 shows a clear wavelength coverage, comparing the filters we use in this analysis to some extra ones, including those used in Bortolini et al. (2024b) (F115W, F200W, F356W, F444W).

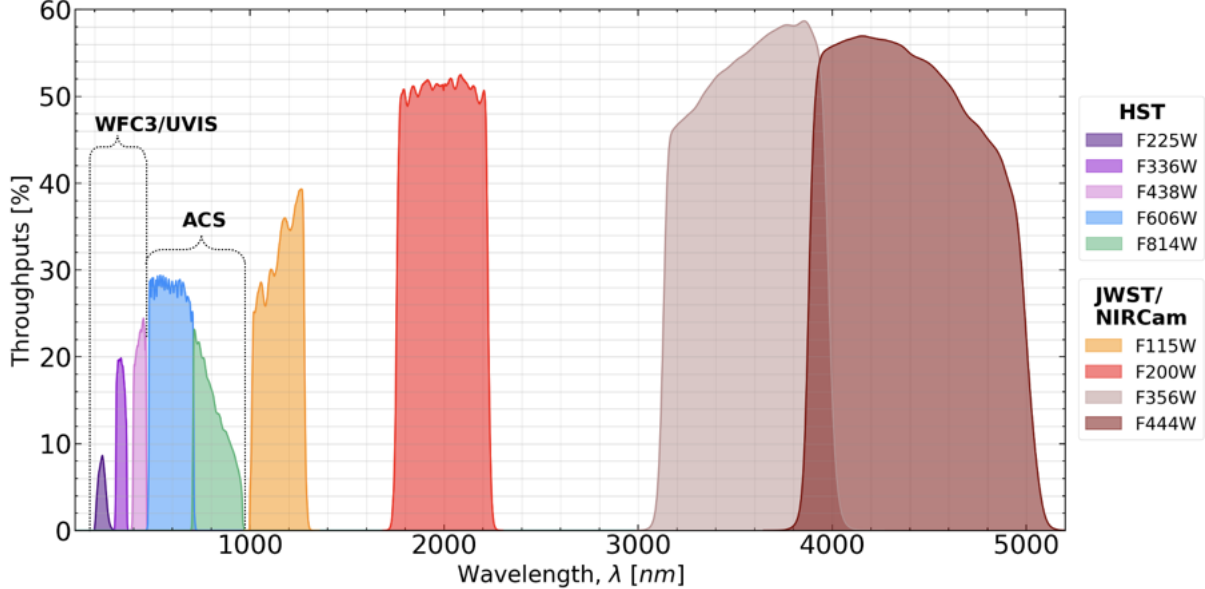


Figure 5: Illustration of the various integrated system throughputs of the filters used along this project (HST/WFC3/UVIS1 wide-band filters: F225W, F336W, F438W), allowing for comparison with HST/ACS F606W and F814W, as well as with those used in Bortolini et al. (2024b) (JWST/NIRCam wide-band filters: F115W, F200W, F356W and F444W).

Data retrieved from: STScI System Throughput Tables⁷ and JWST + NIRCam Throughput Curves.⁸

3.2. PSF Photometric Analysis

Throughout this project, we presented a series of photometric data in the form of scientific frames, along with their corresponding drizzled reference images. These latter ones are the result of a combination of multiple, slightly offset frames to produce high-resolution, geometrically corrected images that preserve flux and enhance accuracy for subsequent PSF photometry (see Section 3.2.1). In this project, the scientific motivation for the use of images detected with filters F225W, F336W and F438W is driven by fundamental astrophysical principles, particularly black-body radiation and stellar evolution. According to the black-body radiation approximation (Cimatti et al. (2019)), a star's peak emission wavelength (λ_{peak}) is inversely proportional to its temperature (T), given by the Wien's law (see Eq. 5).

⁷<https://www.stsci.edu/hst/instrumentation/wfc3/performance/throughputs>

⁸<https://jwst-docs.stsci.edu/jwst-near-infrared-camera/nircam-instrumentation/nircam-filters#NIRCamFilters-Filtertransmissions>

Massive, young O and B-type stars have high surface temperatures of approximately a few multiples of 10^4 K, therefore emitting the bulk of their radiation in the UV-optical range of the spectrum (Cimatti et al. (2019)). Due to the fact that these stars have relatively short lifespans (from 3 to a few hundred Myr), their detection suggests ongoing or very recent star formation. Thus, these filters enable the detection and characterization of the younger stellar population within the galaxy, contributing to a broader understanding of the galaxy's properties and aligning with the primary objective of this study. At NIR wavelengths, as found in Bortolini et al. (2024b), young massive stars do not stand out as prominently because the flux contribution from older, lower-temperature stars becomes significant.

$$\lambda_{\text{peak}} \approx 0.290 \left(\frac{T}{K} \right)^{-1} \text{ cm} \quad (5)$$

3.2.1. DOLPHOT 2.0 and Catalog Compilation

When trying to determine the brightness of astronomical sources, scientists usually rely on a technique called aperture photometry. As stated in Chromey (2016), aperture photometry consists of generating and centering circular perimeters around the desired objects of study – e.g. stars. Since the size of the aperture must be sufficient to include most of the light from the source, it is usually inevitable that pixels associated with the background emission fall within the source's aperture. To account for this, a technique called "sky annulus" is usually applied. It consists of the generation of a ring-shaped region surrounding the aperture. The flux within this annulus is used to estimate the background level near the source, which is then subtracted from the flux measured within the original aperture to obtain an accurate aperture photometry result for the source. However, this method lacks the amount of precision required in regions where overlapping, source-blending and intense crowding rule (Kaur & Joshi (2022)), as in the case of I Zw 18.

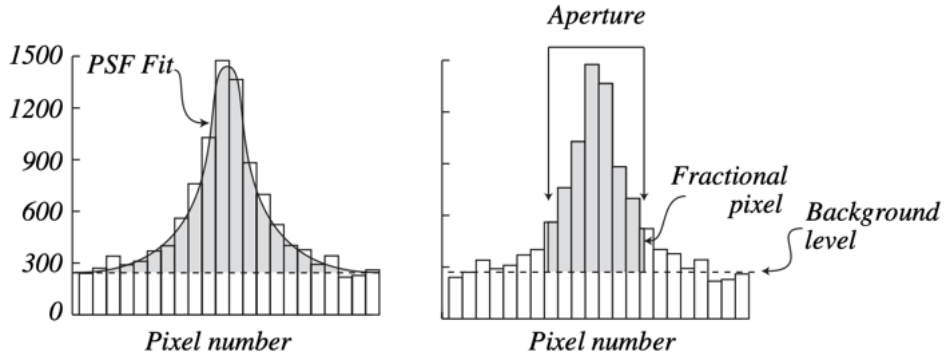


Figure 6: Comparison between PSF fitting photometry (left) and aperture photometry (right). Both images show the brightness of the pixels (y-axis) as a function of the pixels' positions across the source's image (x-axis). The background level is indicated as a dotted line. For the PSF fit (left), a smooth Gaussian curve and the background limit are used to infer the amount of light coming out of the source (shaded region). For the aperture fit (right), the total flux (shaded region) is estimated based on the aperture diameter, missing a greater fraction of the source's contribution towards the edges. Image retrieved from Chromey (2016).

An alternative technique consists on fitting the point-spread function (PSF). Continuing with the previous example of stars and supposing that they are perfectly round (for simplicity purposes), we would ideally expect them to be detected as point-like sources. However, the reality is quite different and stars' light profiles appear blurred due to the detector's optics and other distortion effects. For this reason, PSF fitting routines focus on

the modeling of the telescope's PSF – i.e. "*how the flux of a point source is spread by an imaging system as a function of position on the image plane*", Cimatti et al. (2019). These routines first attempt to approximate the instrument's PSF by modeling the light distribution of a bright star in the image (as isolated as possible) using analytical functions such as Gaussian profiles. However, this serves as a first approximation, while the final PSF reflects the specific characteristics of the instrument in question (Chromey (2016)). Foundations are established with bright sources because they provide sufficient signal to better define the PSF, especially around the wings. Then, the model is adapted in order to fit the rest of the stars by adjusting its parameters in the most suitable way for each case. Consequently, PSF fitting photometry has proven to accurately measure magnitudes from individual sources in crowded fields, where stars are closely spaced (see Heasley (1999) and supplementary references^{9,10}), serving as a much more appropriate tool for this project (see Figure 6).

In this thesis, we make use of the stellar photometry software package DOLPHOT 2.0 (Dolphin (2000), Dolphin (2016), DOLPHOT 2.0 modules¹¹), that employs PSF photometry for analyzing images of densely populated stellar fields. DOLPHOT 2.0 has been widely tested and is frequently used in the astronomical community to produce photometry for millions of stars in hundreds of galaxies in the Local Group, supporting modules for several instruments (Thilker et al. (2022), Weisz et al. (2024)).

This software requires a reference image, a set of science frames, and some user-defined parameters as input. In our particular case, the reference image for our analyses is the drizzled frame in the F438W filter because it detects both the very young and blue stellar populations as well as the slightly more evolved ones, covering the blue spectrum while not solely focusing on the UV. Its greater sensitivity to a broader range of stellar properties allows for consistent identification of stars throughout the analysis. This frame not only sets the basis for the detection of the point-like sources but also serves as a reference for the final coordinate system and is used to align all the other science frames.

On the other hand, before running DOLPHOT 2.0 the program requires a parameter file that contains a long list of settings that control how the software performs photometry on our data (see the manual¹²). Some of these parameters need to be adjusted on the basis of the specific dataset and the instrument used when obtaining the science frames. As already stated in Section 3.1, the science frames taken with filters F225W, F336W and F438W were detected using HST/WFC3/UVIS channel, whereas those taken using F606W and F814W filters were detected with HST/ACS. Therefore, it seems reasonable that a good choice of parameters can significantly impact the quality of the photometry. For a complete analysis, we used Williams et al. (2014) as a reference and performed multiple tests to refine our approach. After this process, we adopted the parameters listed in Table I.

Upon providing the software with the appropriate images, as well as the reference frame and the selected input parameters, we run DOLPHOT 2.0. When running the program with multiple filters simultaneously – as in this case, using F225W, F336W and F438W frames – the output consists of a cross-matched catalog of sources based on their spatial positions. Specifically, the software identifies only those stars for which it can perform a reliable PSF fit and which, in turn, appear in the same location across all selected filters. This approach eliminates the need for a manual cross-match, which would have been necessary had the filters been processed separately.

However, this method comes with a trade-off: a loss of detected sources. For instance, F225W is more sensitive to the UV part of the spectrum whereas F438W extends further into the blue visible part (recall from Figure 5). As a result, the very blue sources that are visible in F225W may be too faint to appear in F438W,

⁹ <https://boyce-astro.org/point-spread-function-psf/>

¹⁰ https://photutils.readthedocs.io/en/latest/user_guide/psf.html

¹¹ <http://americano.dolphinsim.com/dolphot/>

¹² https://physics.mcmaster.ca/~harris/dolphot_primer.txt

and conversely, moderately blue or redder sources – such as helium burning (HeB) stars (see Section 4.4) – may be visible in F438W but fall below the detection threshold in F225W. Nevertheless, we consider this approach to be suitable enough given the main objective of this thesis, providing us with a robust initial catalog of raw data with 24,863 sources. Apart from being cross-matched in position, these stars are accompanied by relevant photometric information that is used throughout this analysis.

Parameter	Value	Parameter	Value
img_RAper	3	FSat	0.999
img_RChi	2	Zero	24.98
img_RSky	15 35	RCombine	1.5
img_RPSF	15	CombineChi	0
img_aprad	20	SigPSF	5.0
img_apsky	15, 25	MinS	1.0
RCentroid	2	MaxS	9.0
SigFindMult	0.85	MaxE	0.5
SigFinal	3.5	Rotate	1
MaxIT	25	SecondPass	5
EPSF	G+L	Force1	1
PSFPhot	1	PSFres	1
PSFPhotlt	2	ApCor	1
FitSky	2	WFC3useCTE	0
SkipSky	2	WFC3UVISpsfType	1
SkiSig	2.25	Align	2
NoiseMult	0.10	UseWCS	1

Table 1: Primary input parameters used in DOLPHOT 2.0 for processing data detected in filters F225W, F336W, and F438W using the HST/WFC3/UVIS detector.

3.3. Data Filtering

While DOLPHOT 2.0 is a highly effective and widely used tool for photometric analysis, it is not without limitations. It may occasionally misidentify spurious detections and background objects as genuine point-like sources within our galaxy, contaminating the data sample with contributors other than the target stars. To refine the resulting catalog while maintaining a substantial sample size, we applied a spatial characterization of the observed region (see Section 3.3.1), followed by a set of parameter constraints aimed at filtering our dataset (see Section 3.3.2). The former was performed to enable for a more precise analysis of the distinct areas within the galaxy in subsequent stages of the project. The latter was executed with the objective of minimizing contamination, ensuring a more robust and representative stellar catalog.

3.3.1. Region Characterization

The classification of distinct regions within I Zw 18’s main body facilitates a more accurate study of the stellar populations in terms of their spatial distribution and properties. To achieve this, we first examined the reference F438W drizzled image (see Figure 1) to gain an understanding of the galaxy’s structure and its position, as well as that of its companion, Component C. At first glance, it is evident that I Zw 18 (black box) contains two main regions characterized for their intense stellar crowding (darker regions in the NW and

SE areas within the galaxy), surrounded by a more diffuse region that extends slightly outward, as already suggested by previous studies (Ramos et al. (2011), Bortolini et al. (2024b) and references therein). These two zones mainly indicate areas of elevated stellar formation.

To ensure greater consistency throughout our analyses, a series of contours were generated around the galaxy at various luminosity thresholds, generating isophote profiles to aid in the characterization of different stellar regions for subsequent examinations. As shown in Figure 7a, both areas characterized by the highest stellar crowding are identified as exhibiting one of the most intense levels of brightness ($\approx 7.55 \cdot 10^2 e^-/s$), corresponding to the most active star-forming areas, as expected. Based on these features, we chose to develop a more tailored partitioning of the galaxy, allowing for a simpler characterization and providing a greater flexibility in selecting specific areas of interest (see Figure 7b).

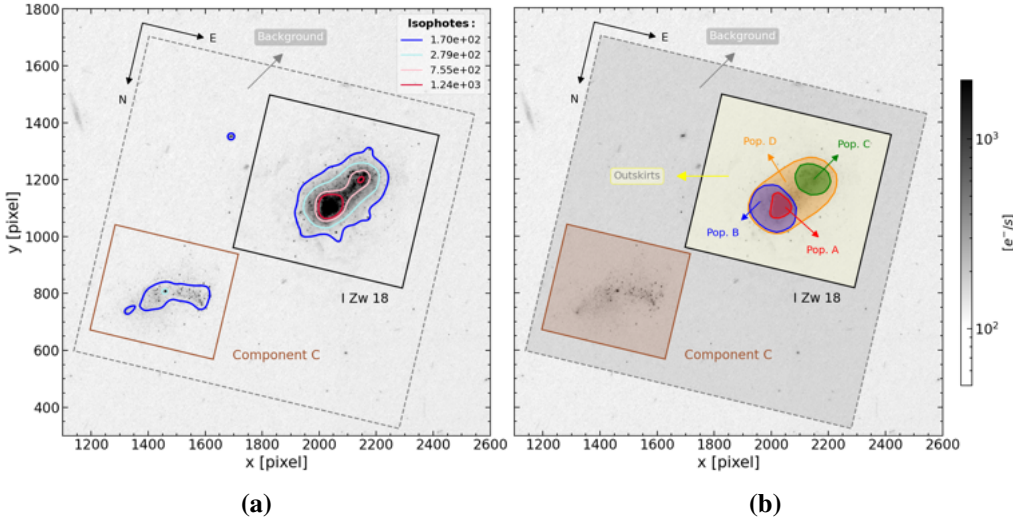


Figure 7: HST/WFC3/UVIS F438W drizzled reference image cutout showing: (a) the representation of a series of smoothed isophotes ($\sigma = 15$) through the application of a Gaussian filtering and (b) the final selection of the different spatial regions for both I Zw 18 and its companion, Component C, guided by the location and shape of the isophote contours.

We first distinguished between the two main galaxies in the plane: I Zw 18 is defined by the black box (including all the sources laying within the boundaries) whereas Component C is analogously defined by the brown box. Within I Zw 18 we characterize smaller, individual areas: Population A (Pop. A) comprises the red region (NW region with the strongest SFR); Population B (Pop. B) is defined by the blue area excluding Pop. A; Population C (Pop. C) is defined by the green area (SW region with the second strongest SFR); Population D (Pop. D) covers everything within the orange perimeter and outside Pops. A, B and C; the outskirts area is painted in yellow and contains the sources within I Zw 18 while excluding Pops. A, B, C and D; finally the background region covers everything within the gray-dashed perimeter, avoiding regions I Zw 18 and Component C. With respect to Component C, it appears somewhat more challenging to distinguish between regions with differing stellar properties and crowding in this case. For this reason, after confirming through isophote analysis that its distribution is relatively homogeneous in terms of brightness, we ultimately decided to examine the entire area within the brown square region as a single unit. Conversely, the background region is of significant interest primarily for refining the quality of our data samples, allowing us to check for spurious sources or potential background galaxies unrelated to our targets that may be influencing the analyses (see Section 4.2).

3.3.2. Parameter Culling

Once the different regions are defined, we proceed with the catalog filtering following some of the indications described in the DOLPHOT 2.0 user's guide¹⁰. We primarily focus on the following parameters: sharpness, crowding, signal-to-noise ratio (SN), object type and photometry quality flags.

As a brief overview, we start with sharpness, which is defined as zero for a perfectly-fit star. Values differing from this one, either positive or negative, respectively represent overly sharp profiles (i.e. cosmic rays) or excessively broad appearances (i.e. blends, clusters or galaxies). For this reason, it is quantified as the square of its absolute value ($|\text{sharpness}|^2$). On the other hand, crowding indicates how much brighter the star would have been detected had nearby stars not been fitted simultaneously. Consequently, for an isolated star, we would be looking for a value close to zero. In contrast, SN is required to be maximized as it is directly related to the ability to accurately measure the signal from the stars while minimizing noise from surrounding and background sources. We additionally have the object type parameter, which is defined to be 1 for "good" stars, whereas higher values indicate faint, elongated or extended sources, among others features. Finally, the photometry quality flags, also known as error flags, are indicators of errors detected during data processing by DOLPHOT 2.0. A value of zero means that the star was recovered extremely well in the image; 1 indicates an aperture photometry extending off the chip, 2 signals too many bad pixels detected and higher values indicate saturated detections or extreme cases of the above.

However, we know that I Zw 18 is not defined by isolated sources but rather by a densely packed field, which hinders the identification and accurate characterization of stars. Before selecting the final set of values for the parameters, we conducted a series of tests through the generation of multi-panel plots, varying pairs of parameters along the x and y axis while fixing the rest. This allowed us to observe how the data sample behaved in the CMD. As an initial test, we decided to plot the CMDs using the combination of colors $m_{F225W} - m_{F438W}$ for the x-axis and m_{F438W} as the selected magnitude for the y-axis (see Section 4 for a further explanation of this decision). Additionally, our parameter selection was guided by previous work, particularly that of Bortolini et al. (2024b), to support a well-reasoned choice.

Figures 8 and 9 represent two of the final tests carried out, with the red boxes highlighting the panels corresponding to the combination of parameters ultimately selected and adopted for this study (see Table 2), showing their effect in the CMD for I Zw 18's main body. In both figures, certain parameters are held fixed to isolate the effects of the variables of interest that are being analyzed. Specifically, object type is chosen to present a value of ≤ 1 in order to retain only the best-quality stars. Regarding the error flag, although the documentation¹⁰ recommended lower values for high-precision photometry, we opted for a slightly more relaxed criterion, with a threshold of ≤ 2 . This allows us to maintain a robust sample without compromising the photometric quality severely. Additionally, both figures vary the SN parameter, which increases from left to right. Figure 8 explores the variation of the sharpness parameter, which decreases from top to bottom, while fixing the crowding to its final value (< 2). Similarly, Figure 9 shows the variation of crowding, also decreasing from top to bottom, while fixing the sharpness to its final value ($|\text{sharpness}|^2 \leq 0.15$).

Focusing first on Figure 8, we observe that increasing the SN threshold beyond a value of 3 results in the loss of a significant number of stars, affecting the statistical power of our sample. On the other hand, decreasing the sharpness threshold to ≤ 0.15 brings it sufficiently close to zero to be considered acceptable, while still preserving a reasonable number of sources. According to the official documentation¹⁰, in an uncrowded field, well-measured stars typically have sharpness values between ± 0.3 . Since we are analyzing a very crowded field, our choice seems fully warranted.

Parameter Conditions

$|\text{sharpness}|^2 \leq 0.15$
 crowding < 2
 $\text{SN} > 3$
 object type ≤ 1
 error flag ≤ 2

Table 2: Culling conditions imposed aiming to remove spurious sources and enhance the reliability of the sample.

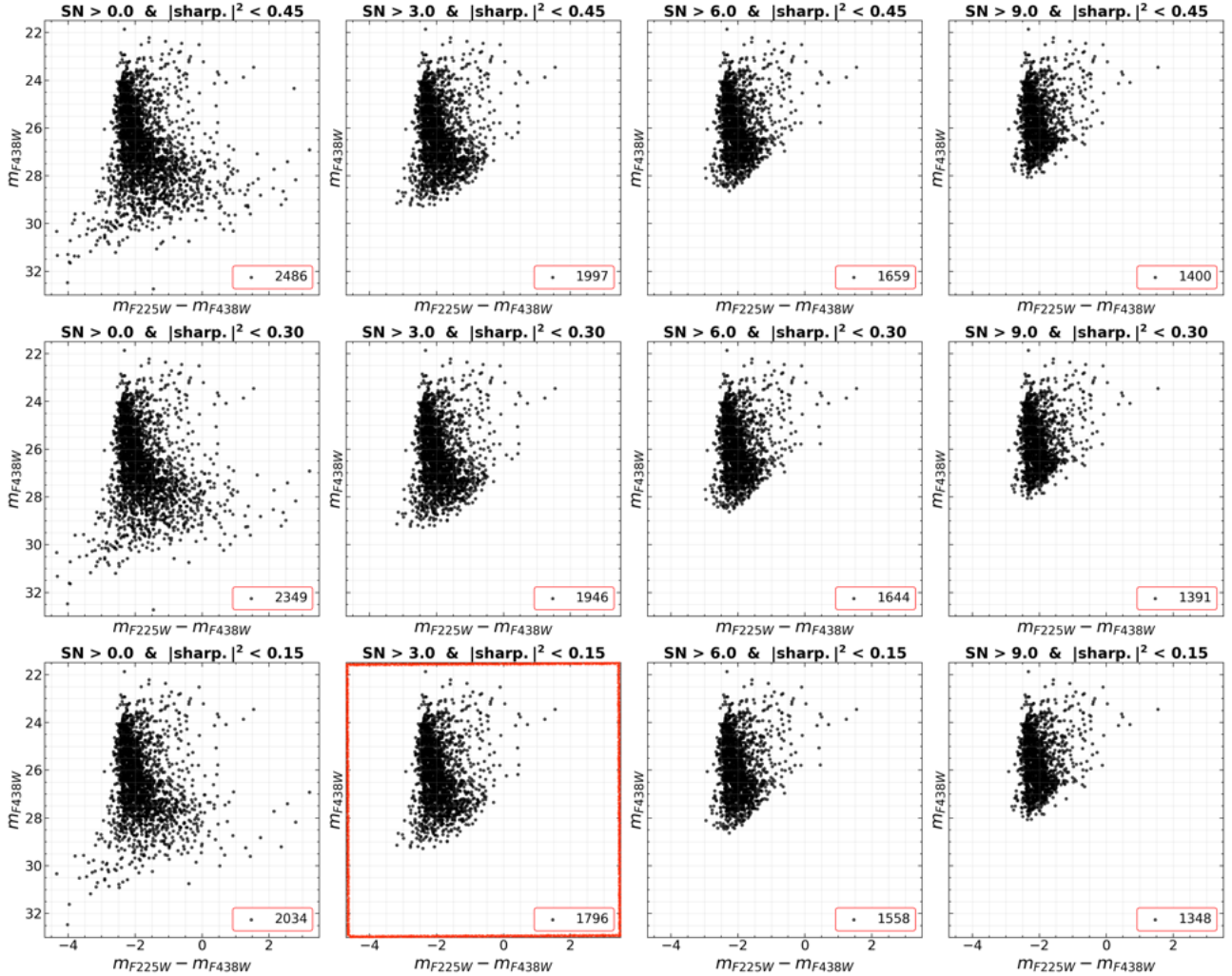


Figure 8: Representation of the variation of SN and sharpness: SN increases from left to right and sharpness decreases from top to bottom. In all these tests we fix crowding < 2, object type ≤ 1 and error flag ≤ 2 . The figure outlined in red represents the selected CMD for I Zw 18's main body (see Figure 7b), used in further analyses.

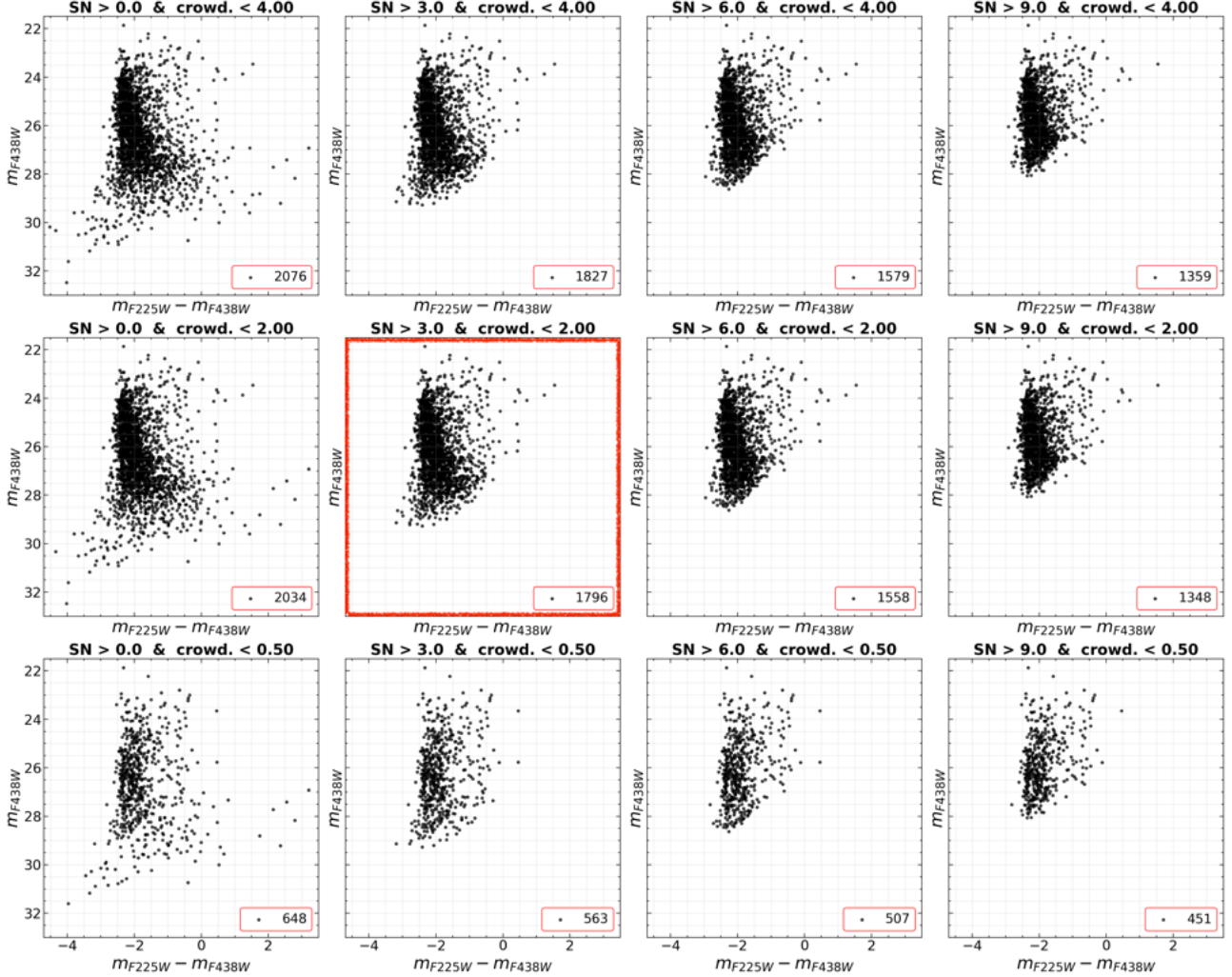


Figure 9: Representation of the variation of SN and crowding: SN increases from left to right and crowding decreases from top to bottom. In all these tests we fix $|\text{sharpness}|^2 \leq 0.15$, $\text{object type} \leq 1$ and $\text{error flag} \leq 2$. The figure outlined in red represents the selected CMD for I Zw 18’s main body (see Figure 7b), used in further analyses.

Turning to Figure 9, we find that setting a crowding threshold lower than 2 results in a drastic reduction in sample size. This is expected, given the nature of I Zw 18, which is characterized by a high density of stars, with sources packed tightly together. This feature makes it difficult to distinguish between individual stars, which is why applying a very strict cut in crowding in this particular case would severely compromise the analysis, as opposed to the strict value of zero recommended by the guidelines in the manual¹⁰ for isolated stars in uncrowded fields. Therefore, we adopt a threshold of < 2 , which maintains an equilibrium between selecting accurately measured stars and managing a reasonable sample.

4. Color-Magnitude Diagram (CMD) Analysis

In Section 3.3, we described the data reduction procedure, in which the stellar population was divided into a set of different regions and culling parameters were applied to refine the dataset. This produced a more reliable

catalog that we now proceed to further analyze. More specifically, we now study the stellar populations across the different regions within I Zw 18, as well as its companion. To do so, we use CMDs, which serve as a fundamental tool for interpreting stellar properties and provide insights into the evolution of the stellar populations. As previously noted in Section 2.4, CMDs are constructed through the combination of apparent magnitudes – reflecting the brightness of sources – and colors – indicating stellar properties such as temperature. In our particular case, we explored CMDs focusing mainly on the different color combinations using the three UV/blue filters from which we had previously generated our catalog (F225W, F336W and F438W; see Section 3.2). To be more precise, our initial analysis focused on comparing the effectiveness of the color index $m_{F225W} - m_{F438W}$ with that of $m_{F336W} - m_{F438W}$, both represented in Figure 10 against m_{F438W} .

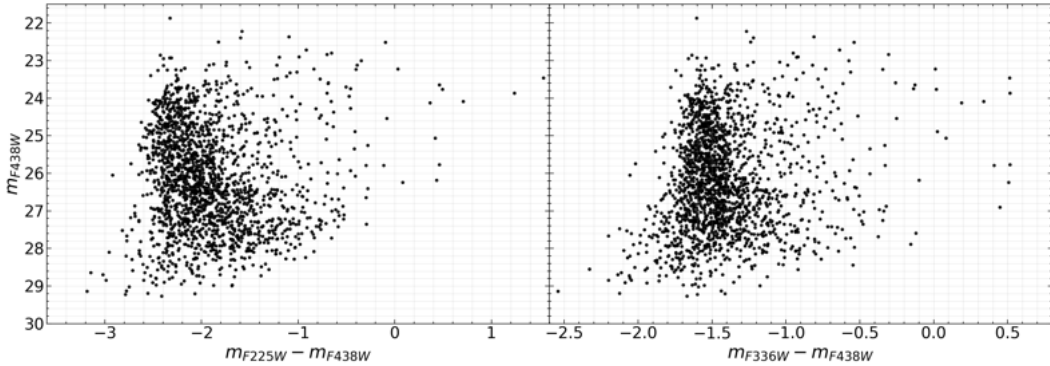


Figure 10: Comparison of the CMDs for the region associated with I Zw 18, using two different color combinations: $m_{F225W} - m_{F438W}$ (left) and $m_{F336W} - m_{F438W}$ (right).

While both representations reveal similar overall morphologies, the diagram using $m_{F225W} - m_{F438W}$ (left panel) presents a wider color range, as expected, improving the sensitivity to temperature differences, making subtle variations in stellar properties more discernible compared to the color combination $m_{F336W} - m_{F438W}$ (right panel). Hotter stars, which emit most strongly at shorter wavelengths, appear more evenly distributed and less clumped in the left panel, representing the most negative values in color. As a result, this combination offers a clearer distinction between young, bluer stars and older, redder populations, essential for our investigation. Furthermore, the selection of the F438W filter for the apparent magnitude in the y-axis is justified, as it effectively represents the overall brightness of a star – that is, a reliable picture of a star’s general luminosity. For this reason, we base our CMD analysis on the color-magnitude combination indicated in the left panel. We will return to filter F336W further ahead when exploring color-color diagrams (CCDs; see Section 5).

4.1. Artificial Star Tests: Setup and Purpose

The high-density profile of point-like sources within galaxies such as I Zw 18 can compromise the construction of a reliable PSF, even when using specialized software programs like DOLPHOT 2.0. The close proximity of stars, particularly in the most crowded star-forming (SF) regions (NW and SE), can challenge the accuracy of the PSF modeling, making it difficult to obtain precise magnitude measurements for the detected sources in each filter. To account for observational limitations and assess photometric completeness and measurement uncertainties, we perform the so-called artificial star tests (ASTs; methodology that has been previously implemented in works such as Stonkutė & Vansevičius (2015), Jang (2023) and Bortolini et al. (2024b), among many others).

The methodology is outlined as follows. Based on the CMD tests performed with our filtered catalog (see left panel in Figure 10), we were able to infer the range in colors and magnitudes of our dataset. After that, we were able to generate a set of artificial stars covering these same ranges along the x and y-axis and distributed according to the density profile of the galaxy (see Figure 7a). Following this, we ran DOLPHOT 2.0 on the science frames together with the artificial star sample, applying the same primary-input parameters to the software as the ones stated in Table I, as well as the same region characterization and threshold configuration as the one stated in Section 3.3. This step ensures a robust and consistent interpretation of the stellar content across all CMDs. Indeed, by initially distributing the artificial stars across the whole CMD range with fixed magnitudes and colors, we were able to assess the discrepancies between the input parameters (*inp*) – provided to DOLPHOT 2.0 – and the output values (*out*) – returned by the software. This is exactly the purpose of ASTs: to evaluate the accuracy of the photometry by helping estimate the photometric errors and completeness of our photometry as a function of position of the source in the image and in the CMD.

DOLPHOT 2.0 processes stars sequentially. This means that it retrieves one at a time, executes the photometric routines and once it finishes with that point-source it continues with the rest of the catalog, repeating the procedure until all the sample has been analyzed. In the case of the ASTs, this works the same way: the software individually introduces each artificial star into the science frames, runs the software, and continues until there are no more sources left. In our particular case, we decided to sample a catalog with one million artificial stars. Therefore, it is easy to figure that attempting to process them on a single run would be computationally expensive. For this reason, we equally organized them into 200 separate batches which are more manageable and enhance computational efficiency by enabling parallelization, maximizing CPU usage. Additionally, it is important to mention that this repetitive pattern is intentionally carried out within the software in order to mitigate crowding effects. Recovering artificial stars one at a time helps prevent contamination of the science frames, which could otherwise compromise photometric accuracy. Indeed, this approach is remarkably critical in densely populated astronomical sources, as the one analyzed in this project.

After this process, we ended up obtaining two main artificial stars' catalogs: the raw one (with the one million artificial stars provided to DOLPHOT 2.0 at the beginning) and the culled and spatially discretized one (with the artificial stars that had passed all the parameter criteria – that is, recovered artificial stars – and that laid in each of the spatial regions defined in the science frame). As discussed earlier, artificial stars were distributed following the light profiles of the real observational data (see Figure 7a). Consequently, the denser regions of the galaxy received proportionally more artificial stars compared to the less populated outskirts. Although recovering individual "real stars" in these high-densely populated areas is partially challenging, introducing artificial stars there aids in determining magnitude errors and provides us with a deeper understanding of the limitations inherent in their photometric measurements.

During this project, we estimated photometric errors using a grid-based approach. We namely focused on the most densely populated area in the CMDs regarding each region of the galaxy, where the majority of the sources were located (this is represented as a band in between red dashed lines in Figures 11 and 12). By doing this, we could concentrate on the most crowded areas within the CMDs and evaluate fairly enough estimates of how errors varied there, without placing excessive emphasis on more scattered sources (not representing the overall behavior of each spatial population). Subsequently, this color band was divided into magnitude cells. This way, we initiated the estimation of photometric uncertainties along the y-axis in the CMDs by comparing the input and output magnitudes of the culled artificial stars in the F438W filter, obtaining what we denote as Δm_{F438W} (see Eq. 6). Then we derived the standard deviation of these differences for the stars laying in each cell, that is, within each magnitude bin ($\text{np.std}(\Delta m_{\text{F438W,cell}})$). This reflects the spread in recovered magnitudes at given brightness levels (magnitude cells), which we can interpret as estimates of the typical uncertainty or error in the magnitude predictions around those areas in the CMD.

$$\Delta_{m_{F438W}} = m_{F438W\text{inp}} - m_{F438W\text{out}} \quad (6)$$

On the other hand, when estimating the color error bars along the x-axis, we chose not to use the formal error propagation method, which would involve computing the uncertainty via quadrature combination: $\sqrt{(np.\text{std}(\Delta m_{F225W}))^2 + (np.\text{std}(\Delta m_{F438W}))^2}$. While this approach is mathematically more rigorous, it heavily relies on the accuracy of the standard deviations which, although valid in our context, should be interpreted with caution. This is because they depend on the number of artificial sources recovered in each grid cell. When only a few are present, the standard deviation becomes statistically noisy and unstable, leading to inflated error estimates. This is an issue, especially when combining them in quadrature. Therefore, when calculating error bars in color we opted for a simpler and more empirical approach, based on the calculation of the difference between the input and output recovered colors (see Eq. 7). Then, following an analogous procedure to the calculation of the error bars in m_{F438W} , we derived the standard deviation of these Δ_{color} values within each cell ($np.\text{std}(\Delta_{\text{color}}_{\text{cell}})$). This method ensures that the error bars reflect both measurement uncertainty and how it varies across the CMD in our selected region, offering a useful approximation of how photometric errors behave in the most crowded areas within the CMDs, where such effects are often most pronounced. It also measures the uncertainty directly from the data without assuming symmetry.

$$\Delta_{\text{color}} = \text{color}_{\text{inp}} - \text{color}_{\text{out}} = (m_{F225W} - m_{F438W})_{\text{inp}} - (m_{F225W} - m_{F438W})_{\text{out}} \quad (7)$$

Apart from the application of artificial stars to perform photometric error analysis, we can utilize them to estimate the completeness level of our sample. Completeness estimation is a fundamental process in observational astronomy since it allows us to quantify the fraction of stars that we successfully detect and recover in the different regions of the CMDs. Because of observational limitations – i.e. instrumental sensitivity and noise – as well as crowding effects, fainter stars can be systematically lost. Moreover, the light from brighter stars can overshadow fainter ones, which translates into an overlap of sources with distinct characteristics that is challenging to resolve even using PSF fitting photometry.

For these reasons, completeness estimation is a tool that provides a reliability threshold for our observational dataset. We began by dividing the CMDs into a grid-space, similar to the approach used when calculating the photometric errors, only that this time we covered the full ranges in color and magnitude in the CMDs rather than focusing solely on the most crowded regions (which were previously defined between dashed red lines). This new approach ensured a comprehensive evaluation of completeness throughout the entire color-magnitude space. The principles of completeness are grounded in quantifying the fraction of artificial stars that are successfully recovered – that is, that pass the culling criteria – relative to the total number of artificial stars. This is done, as with the photometric errors, for each spatial region of the galaxy and within each cell of the defined grid in their corresponding CMDs. We compute the ratio of recovered input artificial stars ($N_{\text{recovered}}^{\text{cell}}$) to the total number of injected stars ($N_{\text{tot inp}}^{\text{cell}}$) in each cell, following Eq. 8. As can be easily appreciated, higher completeness values in each cell (C_{cell}) indicate a reasonable artificial star recovery compared to the initial input, while lower values suggest that fewer artificial stars passed the selection criteria in that specific cell. For the purpose of our analysis, we decided to adopt a conservative completeness threshold of 50%, meaning that only the cells where at least half of the initial artificial stars are recovered are included in the final dataset. This choice is guided by previous studies (Sacchi et al. (2018), Cignoni et al. (2019), Sacchi et al. (2021), Bortolini et al. (2024b), among others) and offers a balance between maintaining reliability while maximizing data inclusion. Once the completeness estimation is performed in each of the cells, we produce a spatial completeness map that we smooth to reduce statistical fluctuations and that is represented as a dark dashed curve under which the area is shadowed. All the stars laying above the threshold

(black dots) represent sources that have been recovered with a reliability of 50% or more, unlike the ones laying within the shadowed region (white dots), that have been recovered with less than a 50% reliability (see Figures I1 and I2). Failing to account for completeness can lead to biased comparisons between observations and theoretical models or simulations, which is why incorporating a good completeness correction ensures the reliability of our analysis, helping us discern between real resolved stars and features necessitating cautious interpretation due to high photometric errors and incompleteness.

$$\mathcal{C}_{\text{cell}} = \frac{N_{\text{recovered}}^{\text{cell}}}{N_{\text{tot inp}}^{\text{cell}}} \quad (8)$$

4.2. CMDs

Figure I1 represents the CMDs for I Zw 18's main body and its companion dwarf galaxy Component C. Figure I2, on the other hand, shows the CMDs associated with the distinct subregions within I Zw 18 and the background area surrounding both galaxies (see Figure 7b for reference). The various panels illustrate the distribution of stellar populations as a function of color ($m_{F225W} - m_{F438W}$) and magnitude (m_{F438W}), providing valuable insights into the characteristics of the stellar content across each of the different spatial regions. It helps determine whether star formation is localized in clusters or spread throughout the galaxy. We mainly focus on stars laying above the 50% completeness threshold (as previously stated in Section 4.1), indicated as black dots in our plots.

We clearly appreciate distinctions between the various plots. I Zw 18's main body (see left panel in Figure I1) reveals a strong concentration of bright, blue stars, reaching magnitudes as bright as $m_{F438W} \lesssim 22$ and predominantly occupying the color range $m_{F225W} - m_{F438W} \in (-3, -1)$, approximately. This distribution aligns with the presence of recent and ongoing star formation – as previously reported by Annibali et al. (2013) and Bortolini et al. (2024b) – and can be interpreted as a vertical prominent blue plume hosting what appears to be the upper MS, with stars that dominate in terms of luminosity within the CMD. The lower MS, on the other hand, extends up to magnitudes of the order of $m_{F438W} \approx 29$, beyond which the sources (white dots) become affected by increasing uncertainties due to several effects. In particular, crowding plays a crucial role. Brighter, bluer sources outshine fainter, redder (and potentially older) ones, making their detection difficult, not to mention the relevance of observational limitations. This is one of the reasons why the 50% completeness level remains reasonably faint at bluer colors, whereas it clearly increases as we move to redder regimes. Moreover, it is highly likely that, even if the telescope presented the optimal resolution and DOLPHOT 2.0 were able to detect the faintest sources, these would still fail to meet the strict parameter constraints we imposed when aiming at producing a clean dataset. This would explain the lack of sources in the shaded regions of the diagram, although, in reality, a significantly larger population of fainter sources would be expected to exist below the threshold. Error bars are also particularly interesting to study in these plots. Following the ASTs introduced in Section 4.1, it seems reasonable that, since fewer "real stars" are recovered below the completeness limit, fewer artificial stars are also recovered in that region. This, consequently, reduces the reliability of photometric error estimates, leading to visibly inflated error bars as we reach fainter magnitudes. Furthermore, when calculating the error bars, we focused on the most populated region of the CMD (enclosed between the color margins), minimizing contamination from scattered and potential spurious sources and improving the accuracy of the derived uncertainties. Additionally, there is a clear spread in the MS as we go down in brightness, visibly consistent with photometric errors: the extent of the broadening correlates in size with the error bars and is coherent given that the photometric error bars increase toward fainter (due to observational limitations) and redder sources. Lastly, it is interesting to observe that extending towards redder colors lies a group of stars likely associated with a more evolved phase – possibly helium-

burning (HeB) stars (see Section 4.4 for further discussion). Nevertheless, these HeB stars are less abundant due to stellar evolution post-MS being faster. Moreover, we are using a combination of UV/blue filters for the construction of the CMDs, favoring the detection of bluer and younger stars. Additionally, reddening may be playing an important role, potentially causing these redder clump to appear redder than they would have been detected had the effects of dust been absent (see Section 5 for further analysis).

On the other hand, Component C (right panel in Figure 11) displays a significantly fainter and less crowded stellar population. Most sources hardly reach magnitudes brighter than $m_{F438W} \approx 25$, with the exception of a single bright object laying at around $m_{F438W} \approx 22.4$, later discussed in Section 4.4. On this occasion, the highest concentration of stars appears approximately around $m_{F438W} \in (27 - 29)$, suggesting not only a fainter but potentially older population when compared to that of I Zw 18's main body. Indeed, Component C's CMD diagram resembles an underpopulated version of that of I Zw 18, with stars concentrated at fainter magnitudes and lacking the prominent blue, luminous stars characteristic of younger stellar populations. Furthermore, the completeness limit, as well as the photometric errors, behave similarly to those observed in the main body.

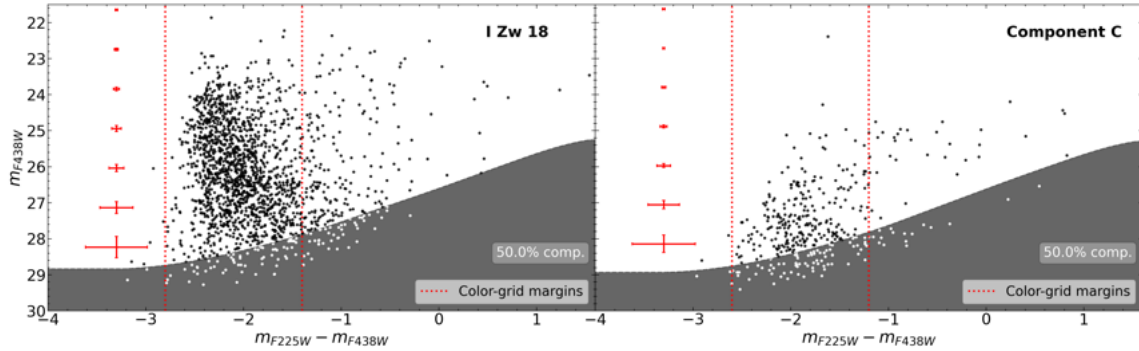


Figure 11: Representation of the CMDs executed using filters F225W and F438W for I Zw 18's main body and Component C defined in Figure 7b. The gray shaded area represents the 50% completeness limit (stars located below this region – white points – have been recovered with less than a 50% reliability). Photometric error-bars (in red to the left side) are estimated within the color-grid margins defined for each region (red dashed lines), focusing on the areas where the stars are more densely packed to gain a general intuition.

The next relevant region to consider is Population A (left panel in the top row of Figure 12) which, as noted in Figure 7b, corresponds to the most densely populated area within I Zw 18 (NW region), with the highest and most recent star formation rate (SFR). Indeed, we can perfectly appreciate an overdensity of stars covering a thinner blue range and reaching the brightest magnitudes seen in the main body, with the faintest sources appearing around $m_{F438W} \approx 26$. This is particularly interesting since this magnitude threshold is nearly the same as the brightest sources observed in Component C. As a result, this suggests that Population A harbors the bulk of the youngest, bluest and brightest stellar population in I Zw 18, as previously mentioned by Bortolini et al. (2024b) and which we are now confirming. On the other hand, stars that are potentially in more advanced evolutionary phases appear distributed toward redder colors, forming the red-dispersed clump that can be observed. These are further analyzed in Section 4.4. It is also important to note that the completeness level in Population A is significantly higher compared to the rest of the spatial regions (completeness begins to decline below 50% at $m_{F438W} \approx 26$). This anticipates that Population A is the most incomplete region, which is logical considering its high crowding conditions and the presence of blue sources that outshine the fainter ones.

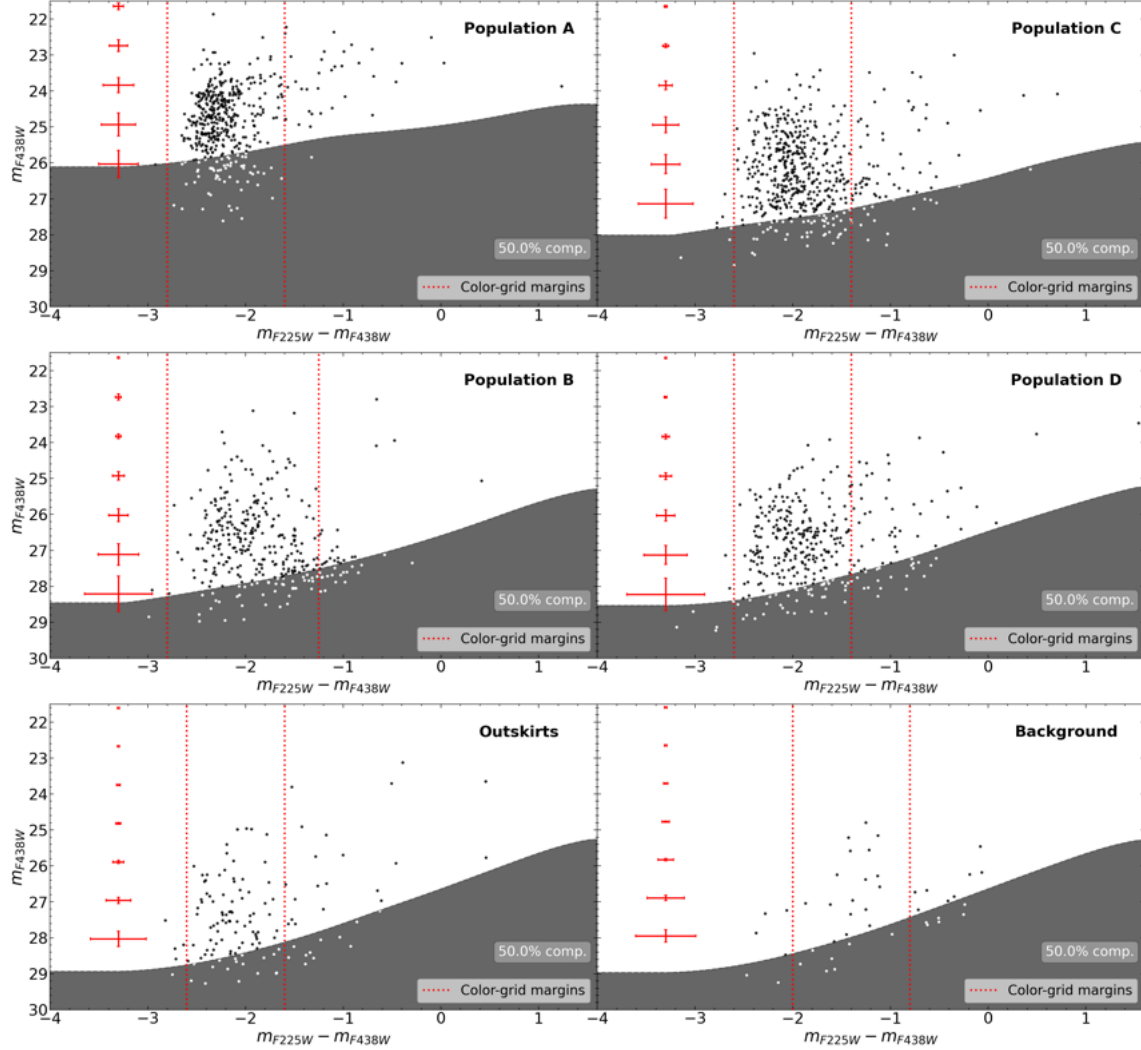


Figure 12: Representation of the CMDs executed using filters F225W and F438W for the subregions defined within I Zw 18 (Population A, B, C, D and the outskirts) as well as for the background surrounding I Zw 18 and Component C (see Figure 7b). For a detailed description see Figure 11.

Population C (right panel in the top row of Figure 12), on the other hand, was already introduced by Bortolini et al. (2024b) as the second most crowded and young stellar clump (SW area; see Figure 7b). Although it presents sources as much as two magnitudes dimmer than the faintest stars present in Population A, it still stands out for presenting blue bright stars reaching magnitudes of approximately $m_{F438W} \approx 23$. Considering that Population C spans over a slightly broader spatial region (see Figure 7b), it seems reasonable that its MS appears somewhat wider, yet it bears a strong resemblance to its counterpart, Population A. Additionally, this region shows more than a 50% completeness limit at around $m_{F438W} \approx 28$ which is reasonable taking into account that it is not as compacted as Population A.

To conclude, Populations B and D (left and right panels, respectively, in the middle row of Figure 12) represent the surrounding areas of Population A and of the combination of Populations A, B and C, correspondingly (see Figure 7b for reference). As a result, we expected these panels to show scarcely populated regions, reaching magnitudes of around $m_{F438W} \approx 29$ since these areas surround the peripheries of the star-forming regions and thus are less affected by the intense crowding of blue bright sources. Furthermore, in the case of the I

Zw 18's outskirts region (bottom-left panel in Figure 12), we detect not only the absence of bright sources but also the detection of redder ones which could be either more evolved stars or even spurious detections (sources that do not belong to the target itself).

In fact, within the background area (bottom-right panel in Figure 12) – which encloses both I Zw 18 and Component C – we can appreciate the highest shift towards redder colors in the detected sources. This highly suggests the detection of spurious sources or background galaxies at higher redshift. This issue can be addressed by examining the stars located above the 50% completeness threshold within the background region using a visualization application such as SAOImageDS9. This way, we can achieve a more accurate classification of the detections that, despite having passed the initial culling criteria, still appear as extended sources, complex systems or exhibit signs of a surrounding diffuse region, all of which suggest manifestations of anything but point-like sources within our targets. Through this detailed inspection, we find that of the 29 targets that lay above the completeness threshold, most of them cluster within particular spatial regions forming complex assemblies, or present a slightly blurred vicinity (all of these cases are enclosed by yellow circles in Figure 13). This way, we can estimate that within our background region we expect to observe at least 5 background sources. Based on this finding, and assuming that galaxies are distributed homogeneously and isotropically throughout the universe, we can estimate how many distant galaxies are likely to have fallen into each region, erroneously affecting the catalogs by impacting the reliability of their detections. This is accomplished through proportionality relationships: i.e. if 5 background sources lay within the background region which extends $1298.858 \text{ arcsec}^2$, then "x" spurious detections are expected to be found in region "Y", with area $A_Y [\text{arcsec}^2]$. We show the areas associated to each of the different regions in Table 3, all of which have been inferred from SAOImageDS9. Our results anticipate to discover around 2 spurious detections in I Zw 18's main body (more specifically in the outskirts area) and 1 background source in Component C. This leads us to conclude that, apparently, our catalog is reasonably well-defined, with highly reliable point-like sources.

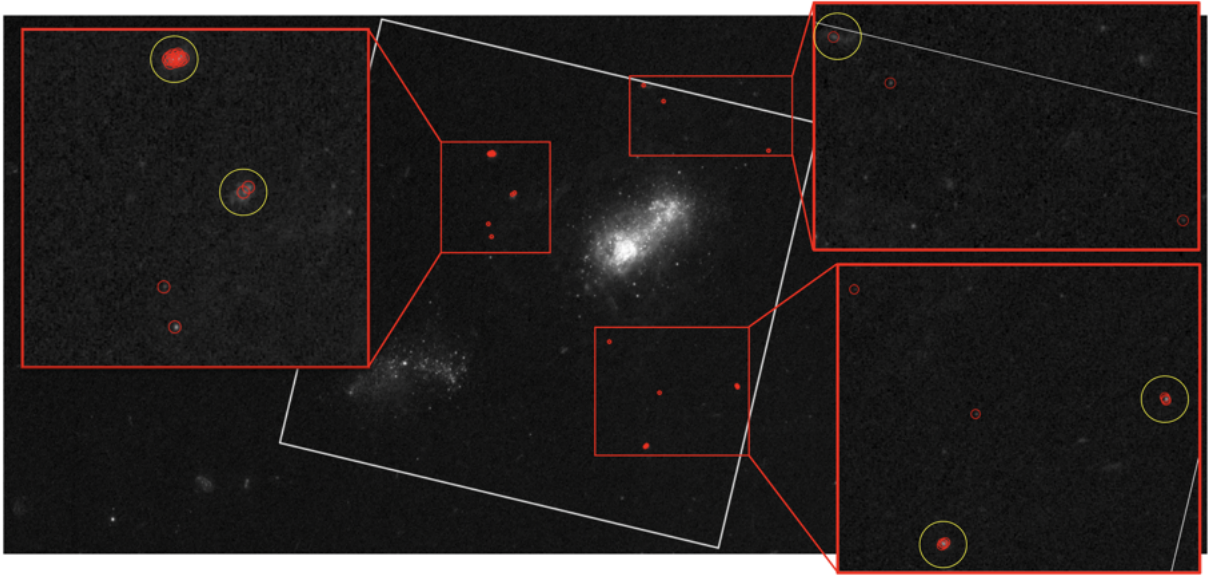


Figure 13: Representation of the boundaries of the background region (white box) with the sources laying above the 50% completeness level (29 targets) enclosed by red circles. The most extended sources or systems exhibiting signs of structural complexity in the surroundings have been circled in yellow, suggesting potential spurious detections or background galaxies.

	I Zw 18	Component C	Pop. A	Pop. B	Pop. C	Pop. D	Outskirts
Area [arcsec²]	528.994	265.028	5.376	24.680	15.292	40.297	443.349
Spurious Detections	≈ 2	≈ 1	≈ 0	≈ 0	≈ 0	≈ 0	≈ 2

Table 3: Areas (in arcsec²) of the different spatial regions within I Zw 18, as well as in Component C, and the corresponding expected number of spurious detections in each of them. The predicted values are derived by assuming direct proportionality to the number of background sources detected (5) within the designated background area (1298.858 arcsec²).

4.3. Isochrones and Evolutionary Tracks

After analyzing the CMDs for each region and characterizing the luminosity and color distributions of the stellar populations, we proceed to investigate further properties such as the range of stellar ages and masses. To this end, we employ two different sets of stellar evolutionary models: MIST and PARSEC.

MIST^{13,14} (Dotter (2016), Choi et al. (2016)) (MESA Isochrones and Stellar Tracks) models are based on the open-source MESA stellar evolution code. It produces extensive single-star evolutionary models, covering all evolutionary phases across a broad range of stellar masses and metallicities. PARSEC^{15,16} (Bressan et al. (2012)) (PAdova and TRieste Stellar Evolution Code) models, similarly, provide comprehensive stellar evolutionary tracks to compute stellar models from the pre-main sequence phase (PMS) to the most advanced stages of stellar evolution.

Using both MIST and PARSEC models allows us to robustly characterize I Zw 18’s stellar population by comparing the predictions of two independent modeling frameworks. One of their most significant differences relies on the fact that each model adopts a different convention for specifying metallicity. For the MIST 1.2 version, $[Fe/H] \equiv [Z/H] = \log_{10}(Z/Z_\odot)$ represents the initial bulk metallicity, with $Z_\odot = 0.0142$, based on the protosolar abundances of Asplund et al. (2009). On the other hand, PARSEC 1.2S employs a scaled-solar composition where $Z_\odot = 0.0152$. This way, our input metallicity varies between models, as outlined in Eqs. 9 and 10. For our case, we assume a metallicity of roughly 3% that of the Sun, justified by previous studies (Searle & Sargent (1972), Skillman & Kennicutt (1993), Bortolini et al. (2024b); see Section I).

$$\left[\frac{\text{Fe}}{\text{H}} \right]_{\text{MIST}} = \log_{10} \left(\frac{Z}{Z_\odot} \right) \approx \log_{10} \left(\frac{0.03 \cdot Z_\odot}{Z_\odot} \right) \Big|_{Z_\odot=0.0142} \approx -1.523 \quad (9)$$

$$Z_{\text{PARSEC}} \approx 0.03 \cdot Z_\odot \Big|_{Z_\odot=0.0152} \approx 4.56 \cdot 10^{-4} \quad (10)$$

4.3.1. Isochrone Fitting: MIST and PARSEC Models

We first began by fitting model isochrones to our CMDs. Isochrones, as defined in Cimatti et al. (2019), are curves that represent the luminosity (L) and effective temperature (T_{eff}) – or, in our case, the magnitude (m_{F438W}) and color ($m_{F225W} - m_{F438W}$) – of stars with a fixed age and metallicity. They provide an essential tool for tracing the evolutionary pathways of stellar populations. In our particular case, we decided to perform

¹³ https://waps.cfa.harvard.edu/MIST/interp_isos.html

¹⁴ https://waps.cfa.harvard.edu/MIST/README_overview.pdf

¹⁵ <https://stev.oapd.inaf.it/cgi-bin/cmd>

¹⁶ <https://stev.oapd.inaf.it/PARSEC/papers.html>

our analysis on I Zw 18’s main body region, for the sake of simplicity and to enable a more general evaluation of our galaxy of interest.

This way, we obtain Figure 14, which shows four different panels in which I Zw 18’s CMD is being overlaid with isochrones, corresponding to different stellar ages mapped as colored curves (going from the youngest to the oldest from top to bottom) and expressed in logarithmic scale. The top two panels display the isochrones retrieved from the MIST model generator, whereas the two bottom plots show those derived from the PARSEC models. Moreover, the primary distinction between the left and right panels lies in the applied V-band extinction values (A_V ; see Section 2.5).

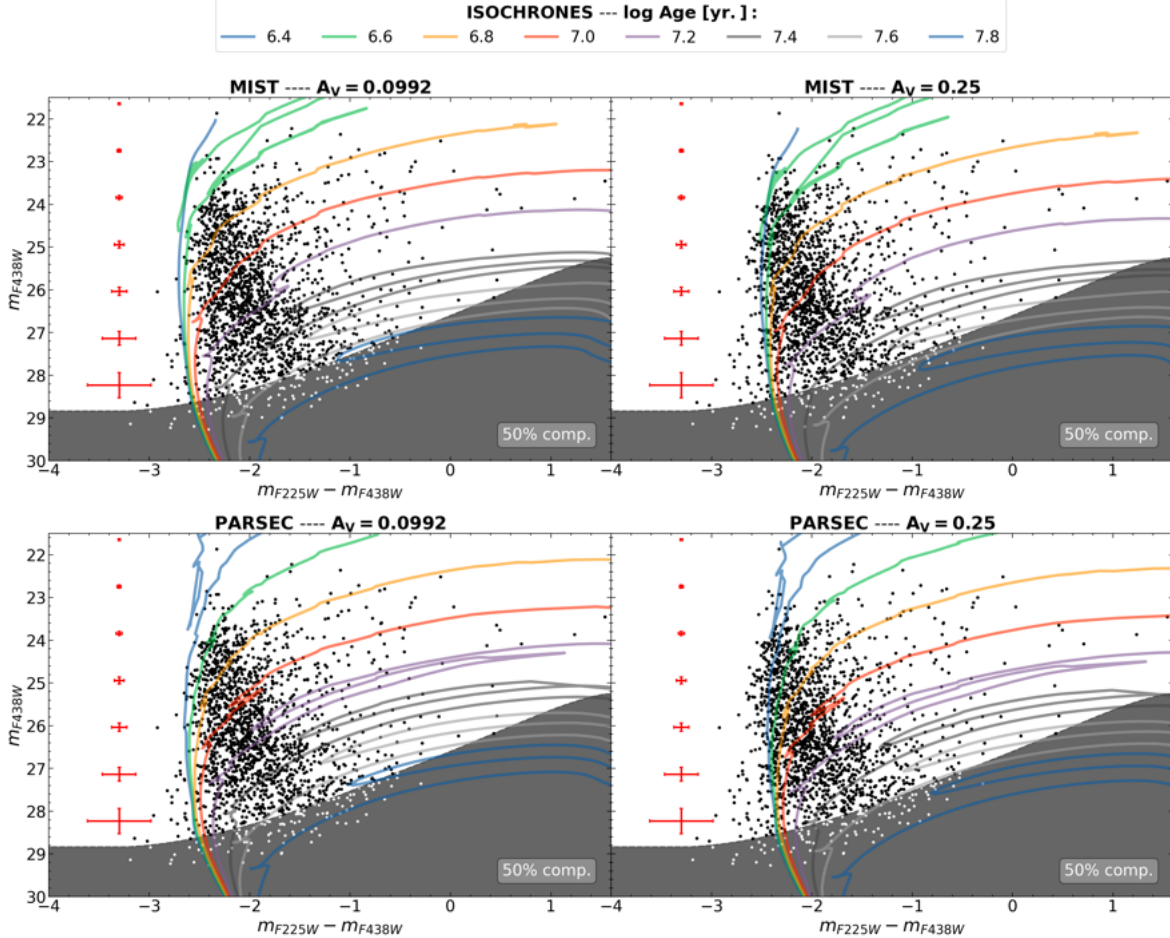


Figure 14: CMDs for the main body of I Zw 18, overlaid with stellar isochrones derived from two different stellar evolution frameworks. The top panels display isochrones from the MIST models, whereas the bottom panels show those retrieved from the PARSEC prototype. Different extinction assumptions are applied: the left-hand side panels adopt a foreground extinction value in the V-band of $A_V = 0.0992$ (assuming a Milky Way (MW) reddening law), while the right-hand side panels introduce an extinction value of $A_V = 0.25$, estimated by inspection to provide a better fit to the main sequence (MS) region. Isochrones are plotted as colored curves, representing stellar populations ranging above the 50% completeness level from approximately 2.5 Myr (top blue curve) to around (25 – 40) Myr (gray curves near the threshold), with age increasing from top to bottom and derived in logarithmic scale.

The panels to the left simply incorporate the foreground extinction correction, with value $A_V = 0.0992$ computed using Eq. 4 with $E(B - V) = 0.032$ and $R_V = 3.1$ (Schlafly & Finkbeiner (2011), Bortolini et al. (2024b)), with the latest being the average value of the gradient of the extinction curve in the Milky Way (Draine (2011)). In contrast, the isochrones shown in the right-hand side of the plot present a higher extinction with value $A_V = 0.25$. This increase in the extinction parameter consequently shifts the isochrones to redder colors, leading to a noticeably better alignment with the observed MS. In particular, this shift leads to a better alignment with the turn-off points – i.e. locations in each isochrone where the most massive MS stars are found, marked by a change in slope. Considering that the galaxy itself likely contributes with internal extinction due to the presence of its own interstellar dust, it seems reasonable that the extinction required to best fit the observed data exceeds that corresponding solely to the foreground contribution. For this reason, we believe that an extinction of $A_V = 0.25$ is a more appropriate choice in this case. Nevertheless, it is important to clarify that I Zw 18’s main dust properties differ considerably from those we expect to find in the Milky Way since our target is a metal-poor blue compact dwarf. Therefore, the initial extinction guess for the foreground reddening might not be the most appropriate and could introduce uncertainty. However, it served as an initial approximation from which we fine-tuned our final selected value (further discussion on the implications of alternative reddening laws is provided in Section 5).

Regarding the stellar populations revealed by the isochrone fitting, we find that I Zw 18 hosts stars ranging from around 2.5 Myr (top blue isochrone covering the bluest brightest sources in the CMD) up to about (25 – 40) Myr (grayish isochrones covering the stellar population right above the completeness threshold). This age spread highlights the overall presence of a very young stellar population within the galaxy, as was previously suggested by Bortolini et al. (2024b) but that had never been observed in the UV/blue bands before.

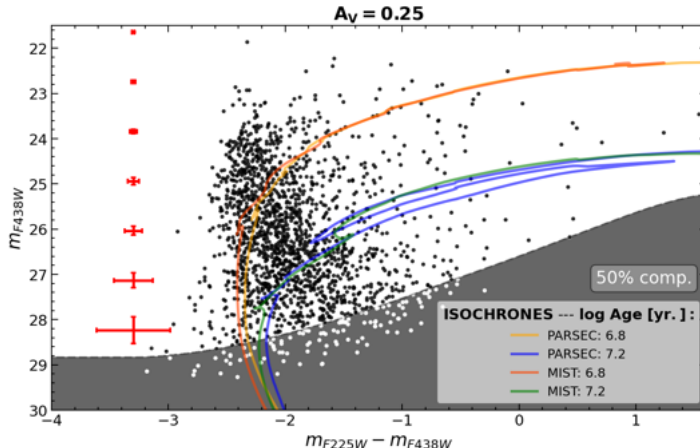


Figure 15: CMD for I Zw 18’s main body with an extinction value of $A_V = 0.25$, chosen to improve the fit of the MS. Overlaid are a couple selected isochrones from both the PARSEC (orange and blue) and the MIST (red and green) models, represented for comparison purposes, highlighting the potential differences between the two different frameworks.

We further examine the difference between the MIST and PARSEC fitting accuracy. At first glance, Figure 14 shows little difference between the two models. The only notable distinction is that the isochrone corresponding to the younger population fits the brightest magnitudes more properly in the PARSEC model compared to the MIST one. However, aside from this, the overall discrepancy remains minimal. Because of this, we decide to elaborate Figure 15, where we directly overlay a couple of isochrones from each of the models, allowing for a more straightforward visualization of their differences. We see that both sets provide a broadly

consistent representation of the stellar populations. Minor differences are likely attributable to variations in the underlying physical assumptions and input values required from each model during the isochrone construction (i.e. the difference in the metallicity definitions, see Eqs. 9 and 10), none of which appears to be substantial enough to significantly impact the results.

As a consequence, for the analysis that follow, we assume $A_V = 0.25$ as the preferred extinction value and we choose to focus on the MIST model – that is, the top-right panel in Figure 14. Knowing that the choice between one framework or the other does not result in a dramatic difference, we motivate the selection of MIST models as they allow for the introduction of stellar rotation (see Sections 4.3.2 and 4.3.3) as an adjustable variable. This feature is particularly interesting to take into account as rotation can have a significant influence on the interpretation of the models, especially in low-metallicity environments. PARSEC 1.2S does not support this feature, and the version that would allow it could not be used due to metallicity constraints.

4.3.2. MIST Isochrones Rotation Fitting

As previously mentioned, in this section we focus on the effects of stellar rotation in the retrieval of isochrones from the MIST model. MIST 1.2 version – which is the one available – includes a feature that allows for the introduction of rotation through a parameter called initial v/v_{crit} . It can be interpreted as the initial surface velocity of the star (initial v) compared to its critical surface linear velocity (v_{crit}) – which is the maximum speed of a star before its centrifugal force overcomes gravity at the equator. According to Choi et al. (2016), “*all rotating models are initialized with solid body rotation on the Zero Age Main Sequence (ZAMS)*”, which is why this parameter is also defined as $v_{\text{ZAMS}}/v_{\text{crit}}$, representing the fraction of the critical/break-up velocity that a star is rotating at when it reaches ZAMS phase – that is, when it starts burning hydrogen in the core. Consequently, this parameter gives us an idea of the percentage of the star’s initial rotational velocity relative to the maximum speed it can sustain before breaking apart. It can be set to either 0 or 0.4. Up to this point, in Figures 14 and 15 we had used the non-rotating version, setting the parameter to zero, so that we could compare the results with the PARSEC framework. However, along this current analysis we aim to assess the impact of rotation on our isochrone fitting procedure.

This can be seen in Figure 16, where we observe the difference of the fitting of MIST isochrones without rotation (left panel) – which is exactly the same plot as the top-right panel in Figure 14 – and those with the rotation parameter set to 0.4 (right panel). First, the most noticeable difference observed is the variation of the isochrones and how they fit the data, specially for the younger regime between (2.5 – 6.3) Myr – that is, the blue, green and orange curves. They seem to fail to properly fit the very blue, bright clump of stars in our dataset. At first glance, this might lead one to assume that the stars in I Zw 18, more particularly in this clump, are non-rotating, as rotating stars would be expected to be fitted in a reasonable way by the isochrones. However, this idea contradicts existing knowledge that stars do indeed rotate. In fact, as previously introduced in Section 2.3 studies such as those of Legrand et al. (1997) and Izotov et al. (1997) revealed the presence of Wolf Rayet (WR) stars in I Zw 18. These are characterized, among other features, by their strong stellar winds, which are partly driven by their high rotational speeds. Therefore, what might be happening is that this model is implementing a velocity that might not be as high as the one required to fit these peculiar stars. It is also possible that the models are poorly calibrated at very low metallicities. Another important point to consider is that these stars are not only very bright but also likely very massive (see Section 4.3.3). We know that massive stars are subject to intense stellar winds, which cause significant mass loss and drive rapid evolution through a sequence of brief and complex stages. In some cases, their evolution happens so quickly that their core and envelope become mechanically and even radiatively decoupled. This could result in the core rotating much faster than the envelope, making them particularly challenging to model. Moreover, their short lifespans make it difficult for us to observe these stars across all evolutionary stages, limiting our ability to properly disentangle the full range of their physical behavior.

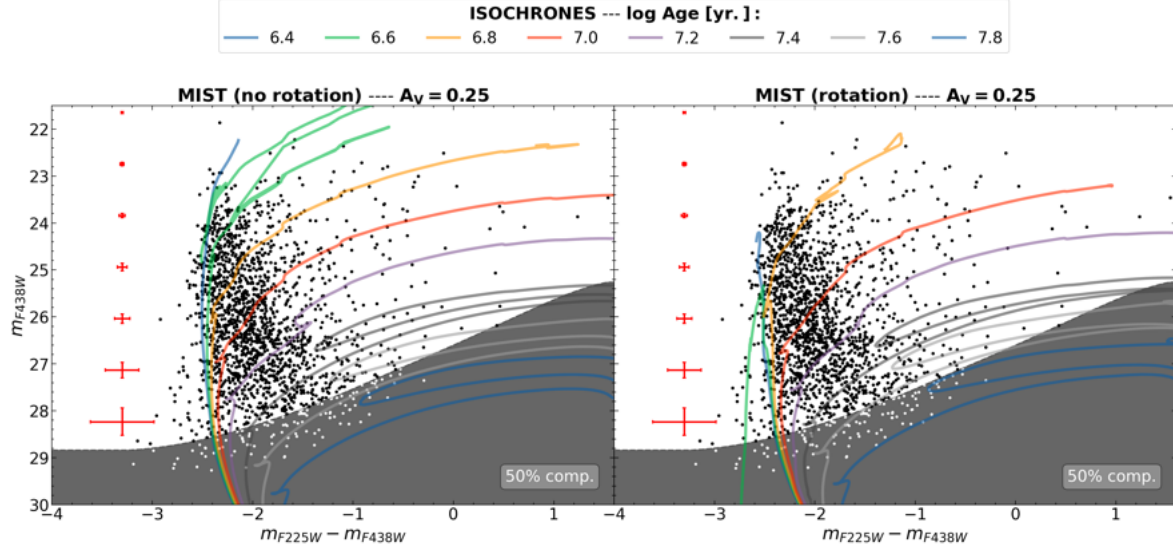


Figure 16: CMDs for the main body of I Zw 18, overlaid with MIST isochrones assuming an extinction value of $A_V = 0.25$. The left panel shows the isochrones with the rotation settings disabled (same plot as the top-right panel in Figure 14), while the right panel displays isochrones with activated rotation, highlighting the impact of this feature along the fitting analysis.

Therefore, MIST models, while valuable, may not be fully developed to be adjusted to the stellar component in galaxies as peculiar and metal-poor as I Zw 18. Instead, they are tested on nearby star clusters and galaxies located within or close to the Milky Way, which present completely different characteristics compared to I Zw 18. Thus, the observed discrepancy could either indicate something relevant about our stellar population that we still do not understand and/or reflect limitations in the isochrone models themselves. It could also mean that rotation alone is not sufficient to account for the characteristics of these very bright stars. While models may not perfectly fit our data, this discrepancy offers valuable insights into the stellar population of I Zw 18, opening new paths for further investigation.

4.3.3. MIST Evolutionary Tracks Fitting

For a more comprehensive analysis, we elaborate Figure 17, which is an analogous representation to the one shown in Figure 16, but instead of displaying isochrones it now shows some evolutionary tracks representing a series of stellar masses for the populations within I Zw 18. Similarly, we also interpret the differences between enabling and disabling the rotation parameter within the MIST framework.

Therefore, upon examining the left panel, which shows the tracks in the case of no rotation, we observe that the stellar population displays a mass distribution ranging from approximately $8 M_\odot$ (blue curve slightly extending beyond the shaded 50% completeness region) up to around $140 M_\odot$ (blue curve covering the brightest stellar sources), and potentially even higher values. Notably, when we examine the right-hand side plot, where rotation is introduced, this finding supports the idea that the most massive (as just retrieved) and youngest (as shown in Figure 16) stars are the brightest and bluest ones and at the same time the least well fitted by the models when adding rotation.

This is a particularly interesting observation. As we previously mentioned, more massive stars have shorter lifespans (see Section 3.2). Thus, it is reasonable to expect that models struggle to accurately represent these sources. Additionally, we are dealing with a very metal-poor environment with metal-deficient stars, which

tend to be more dense and compact, resulting in lower pressure support from radiation and consequently rotating faster than metal-rich sources. This is supported in Chiappini et al. (2006), where they show that metal-poor stars can reach rotational velocities of the order of (600 – 800) km/s. Moreover, the effects of stellar winds – contributing to stellar mass loss – could significantly impact the position of stars within the CMD. As a consequence, it might be challenging to adapt models so that they account for all these stellar features and behaviors when introducing rotation.

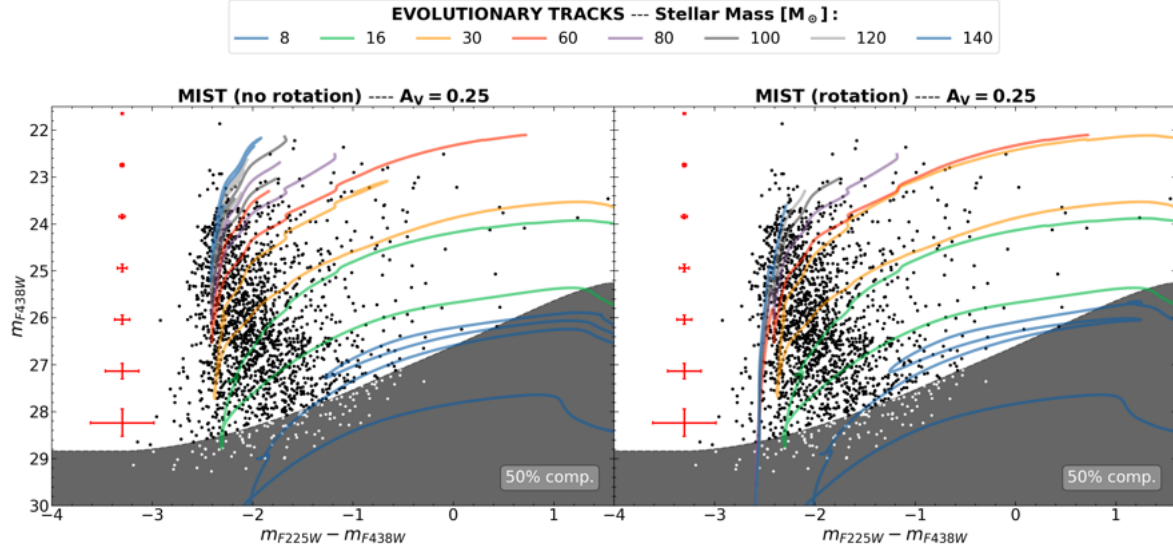


Figure 17: CMDs for the main body of I Zw 18, overlaid with MIST evolutionary tracks showing the stellar mass distribution within the galaxy, assuming an extinction value of $A_V = 0.25$. The different stellar masses are plotted as colored curves, characterizing stellar populations ranging above the 50% completeness level and covering a mass range from approximately $8 M_\odot$ (bottom blue curve) to around $140 M_\odot$ (top blue curve), with mass age increasing from bottom to top. The left panel shows the tracks with the rotation settings disabled, while the right panel displays tracks with activated rotation, highlighting the impact of this feature along the fitting analysis.

It is also interesting to mention that the remarkable number of very massive stars detected (reaching masses of around $140 M_\odot$ and perhaps even higher) are likely WR star candidates, as suggested in previous studies (see Section 2.3 and 4.3.2). It might be possible that, in order to explain the high number of massive stars, a typical Kroupa IMF (Kroupa (2002)) may not be well suited. Perhaps, the appearance of such massive stars comes from episodes with high SFRs or maybe even from a rather top-heavy IMF distribution (Lamers (2005), Smith et al. (2008)). However, due to our detection limit (reaching masses of around $8 M_\odot$) and the incomplete sampling of the full stellar mass range across the galaxy, we cannot conclude anything about the IMF, apart from the intriguing finding of the presence of very high massive stars and the need for future further studies on this topic.

4.4. CMD Segmentation: He-burning (HeB) Stars

According to stellar evolution theories, as a star ages it increases its core temperature, where it exhausts hydrogen (H) in order to counteract gravitational collapse. When central hydrogen is depleted, these stars leave the so-called MS phase and continue their stellar nucleosynthesis through the burning of heavier elements such as helium (He). Among other aspects, these stars evolve according to their initial mass. In low and

intermediate mass stars, helium ignition occurs at the red giant tip (see Figure 18a), whereas in more massive stars, helium burning starts once they leave the MS, while the star is still blue, having only partially evolved through the Hertzsprung–Russell (HR) diagram (see Figure 18b) – or, equivalently, the CMD. This latter scenario aligns well with our observations of I Zw 18, where we have been able to confirm through Figure 17 that the majority of the resolved stars above the completeness limit are significantly massive, with bright and blue features. For these type of stars, their luminosity – ergo, their magnitude – does not change significantly at the onset of He-burning since their H-burning still dominates in the shell.

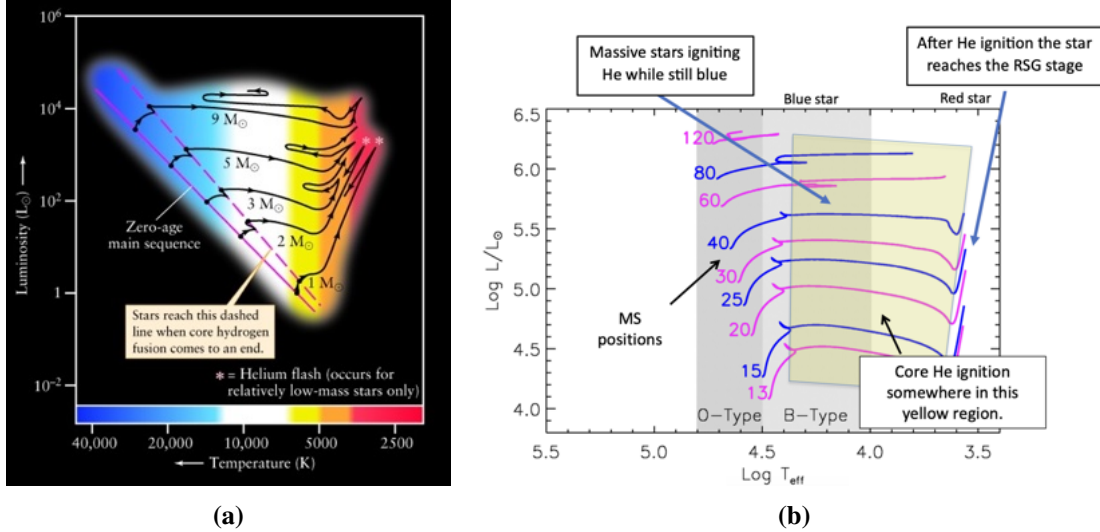


Figure 18: HR diagrams with evolutionary tracks showing the He-burning phase with respect to the mass range: (a) shows low and intermediate mass stars reaching He ignition at the red giant tip (figure retrieved from Geller et al. (2019)) and (b) showing high mass stars reaching He ignition after leaving the MS, having moved partially through the yellow-marked zone where they are still reasonably blue (figure retrieved from Limongi (n.d.)).

Throughout this next step, our primary goal is to characterize the stellar populations by differentiating them across age bins demarcated with the MIST isochrones. To achieve this, we focus on core He-burning (HeB) stars, which offer a distinct advantage over MS ones. This is related to the fact that age sequences become distinguishable only during latter evolutionary stages, such as the HeB phase. MS stars' positions on the CMD, on the other hand, significantly overlap across different stellar ages (see Figure 16 (left)), challenging the discretization process. In this way, we analyze the spatial distribution of HeB stars across the different age intervals by adopting a methodology similar to that in Cignoni et al. (2019), where they use a percentile-based selection criteria to define bona fide HeB stars. A percentile approach provides a statistical method for distinguishing between the two stellar phases, minimizing subjective selection and avoiding a direct reliance on the turn-off point of isochrones which, as just stated, are densely clustered around the MS, not easily separable. Percentiles, however, aid in the calculation of the real CMD distribution, ensuring a more accurate representation of the underlying population structure. In this study, we compute the 50th and 75th percentiles of the color distribution of I Zw 18 within magnitude bins along the y-axis, smoothing the results due to noise effects or the contribution of small sample sizes in each bin.

These results are shown in Figure 19. The 50th percentile (blue curve in the left panel) represents the typical or most frequent color in each bin and generally coincides with or closely resembles the position of the MS. The 75th percentile (orange curve in the right panel), on the other hand, indicates where only 25% of

the stars are redder (to the right of the curve), thus offering a more conservative boundary. For this reason and with the purpose of isolating HeB stars without adopting an overly cautious approach, we opted to use the 50th percentile cutoff. This decision may allow for a small degree of MS-star contamination along the most crowded area in the CMD. Additionally, it misses the introduction of the very bright clump of stars. However, although not completely confident about their nature – whether they truly belong to the MS or to the HeB phase – either way, these bright stars are subject to small photometric errors and so we expect their absence within this study not to be critical. Thus, even though the use of the 50th percentile might introduce a small number of interlopers, it provides a better balance between sample purity and statistical power. Apart from the segmentation introduced through the percentiles, we incorporated a series of MIST isochrones for the differentiation of age bins within the stellar population. We classified the galaxy into four groups: stars younger than ≈ 6.3 Myr (cyan), stars between $(6.3 - 10)$ Myr (green), those falling within the range of $(10 - 15.8)$ Myr (pink) and stars older than ≈ 15.8 Myr (red).

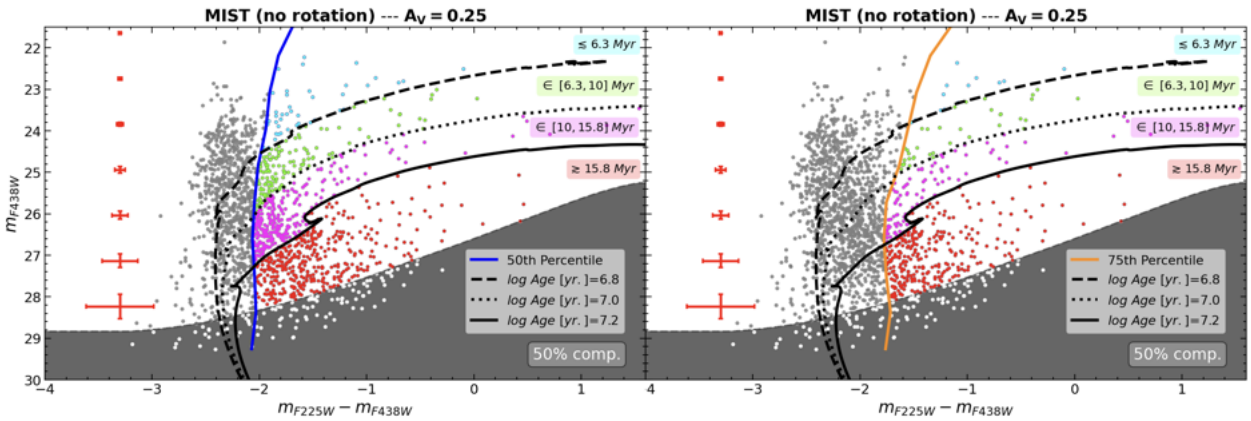


Figure 19: CMDs for the main body of I Zw 18, overlaid with three MIST isochrones assuming an extinction value of $A_V = 0.25$, with the purpose of discerning between MS and HeB stars through percentile demarcation curves and categorizing the stellar population according to age regimes. The isochrones divide the CMD into four age bins: stars younger than 6.3 Myr (cyan), stars ranging from $(6.3 - 10)$ Myr (green), those ranging between $(10 - 15.8)$ Myr (pink) and older than 15.8 Myr (red). The left panel shows the 50th percentile (blue curve) and the right panel displays the 75th percentile (orange curve).

The spatial distribution of these four age groups is shown in Figure 20. When comparing the differences between the two percentiles, we simply observed that the 75th percentile scenario drastically reduced the sample size of the population but presented no further distinctions, which is why we decided to stick with the 50th percentile case instead. This way, Figure 20 displays stellar spatial distributions that seem consistent with previous findings. On the one hand, the youngest stars (cyan and green) appear clustering in the expected NW and SE star-forming regions of I Zw 18, as previously mentioned by Bortolini et al. (2024b) (among other studies). It is relevant to state that the lack of stars older than 10 Myr in the NW (specially) and SE clumps – associated with Populations A and C (see Figure 7b) and most commonly referred to as the most recently star-forming regions – is not due to their actual absence, but rather to observational biases such as completeness effects. The intense brightness of the bluest, most luminous sources in these crowded regions makes it difficult to detect redder, fainter stars because they are often obscured by the brighter ones. Additionally, high crowding significantly limits both the telescope’s ability to detect individual sources and the performance of DOLPHOT 2.0 in reliably resolving them as distinct stars. Furthermore, as we go older in age (pink and red populations) – although still considerably young – stars distribute more into the outskirts, as expected from stellar migration.

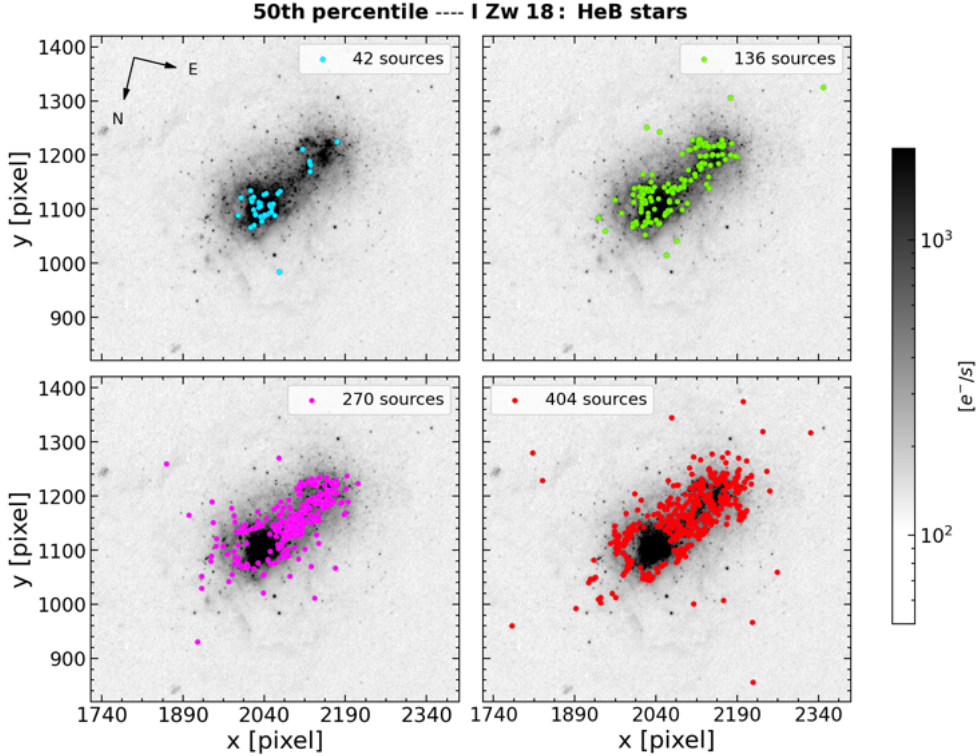


Figure 20: Spatial distribution of the stellar population in I Zw 18 based on age classifications and a 50th percentile selection. Stars younger than 6.3 Myr are represented in cyan, those between (6.3 – 10) Myr in green, between (10 – 15.8) Myr in pink and older than 15.8 Myr in red. The population shows an outward distribution with increasing age, from densely central regions crowded with young stars (particularly the NW and SE areas) to more extended outer regions populated with older generations. The lack of older populations in the NW (and even the SE) area is mainly due to completeness and crowding effects.

Furthermore, to ensure a more thorough analysis, we decided to conduct the same study for Component C, although introducing some slight changes. Component C's CMD is characterized by a smaller and more sparsely distributed stellar population compared to that of I Zw 18. Consequently, it shows a less clearly defined MS that is challenging to fit with the corresponding MIST isochrones. Besides, the limited sample size in this case prevents a robust percentile-based selection. As a result, we instead apply a cut at $m_{F225W} - m_{F438W} = -1.9$, based on an educated guess to roughly separate what seems to be the MS from evolved stars. We have decided to maintain the MIST isochrones employed for I Zw 18's analysis, with the same extinction value despite knowing that this assumption may not hold completely. While both systems are likely interacting and are positioned close to each other, extinction could still vary significantly between them. However, with the data we have we can not precisely know the variation of this value reliably, so we decide to stick with $A_V = 0.25$ instead, for simplicity purposes.

Figure 21 shows the segmentation between "MS" and HeB stars for Component C, as well as the age binning using the models. We can notably appreciate the striking absence of stars younger than 6.3 Myr (cyan; analogous to Figure 19), only being able to detect a bright source at around $m_{F438W} \approx 22.5$. This is a result that had not been detected in earlier studies, underscoring the strength of our HST/WFC3/UVIS dataset. The HeB population in Component C is rather distributed between (6.3 – 15.8) Myr (purple) or at ages older than 15.8 Myr (red; analogous to Figure 19).

It is immediately apparent that the stellar population here is significantly more spread towards "older" age-bins than what was previously observed for the main body. When examining its spatial distribution (see Figure 22), we note the following: what initially appeared to be a single, bright, blue star younger than 6.3 Myr (cyan source in Figure 21) appears to be a more extended yet unusually compact source located near the galaxy's center (see source indicated with a blue arrow in Figure 22). This could point towards the theory that it might be an open stellar cluster composed of young blue stars that we are unable to resolve given the resolution limits of HST at such great distances. We should also take into account that, in an ideal scenario, we would model the PSF using isolated point-like sources. However, in practice, observational effects – such as crowding and overlapping sources, especially in dense fields like those in I Zw 18 – can distort the PSF, making stars appear less round. The blending of light from one star to the other increases photometric uncertainties, making the reduction challenging even when using PSF fitting techniques. Besides, the somewhat older stellar populations (purple and red) appear to be widely distributed throughout the galaxy with no major differences between them, except for the number of stars in each group, which is almost 4 times greater for the older generation (red sources).

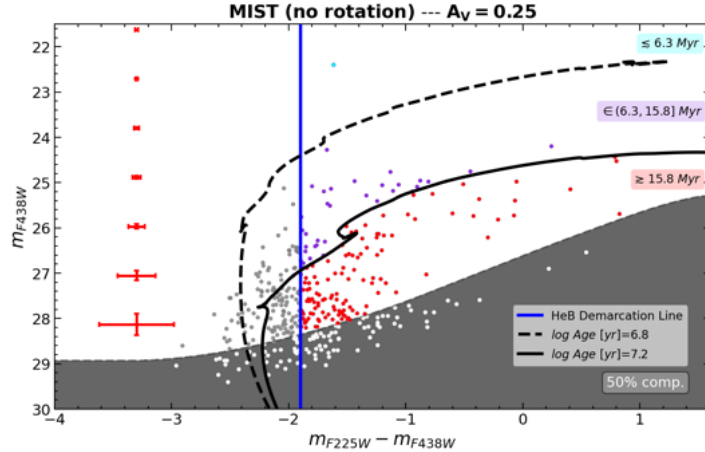


Figure 21: CMD for Component C, overlaid with two MIST isochrones assuming an extinction value of $A_V = 0.25$. It represents the discretization between MS and HeB stars through a demarcation line inferred by inspection and the categorization of the stellar population according to age regimes. The isochrones divide the CMD into three age bins: stars younger than 6.3 Myr (cyan), stars ranging from (6.3 – 15.8) Myr (purple) and those older than 15.8 Myr (red).

If the current starburst in I Zw 18 is driven by gravitational interactions between the two galaxies, as proposed by Bortolini et al. (2024b), it is puzzling that Component C does not exhibit a similar outburst. This lack of very young stars appreciated in Component C might suggest a quenching of recent star formation activity. This could be potentially explained by the lack of sufficient cold gas in Component C so as to fuel star formation. This scenario would be supported by the findings of Lelli et al. (2012), who reported that while Component C is embedded in I Zw 18's extended H_I structure, it does not show the same level of gas concentration or compactness as the main body, suggesting less gravitational potential and likely less star formation (see Section 6 and Figure 29 for further information). This could be due to prior starburst-driven feedback or tidal stripping, particularly given that Component C appears to be smaller and less massive. According to Cimatti et al. (2019), the proximity of a galaxy to a more massive one effectively removes the cold ISM from the former system through interactions such as the ones described above. It is also possible that I Zw 18 is accreting gas from Component C. Given the extremely low metallicity of the main body and its young stellar population, the inflow of pristine gas from its companion could explain both the metal deficiency nature of I

Zw 18 and the gas depletion from Component C. This interpretation is consistent with the current lack of very young stars in Component C and the more evolved nature of its stellar population.

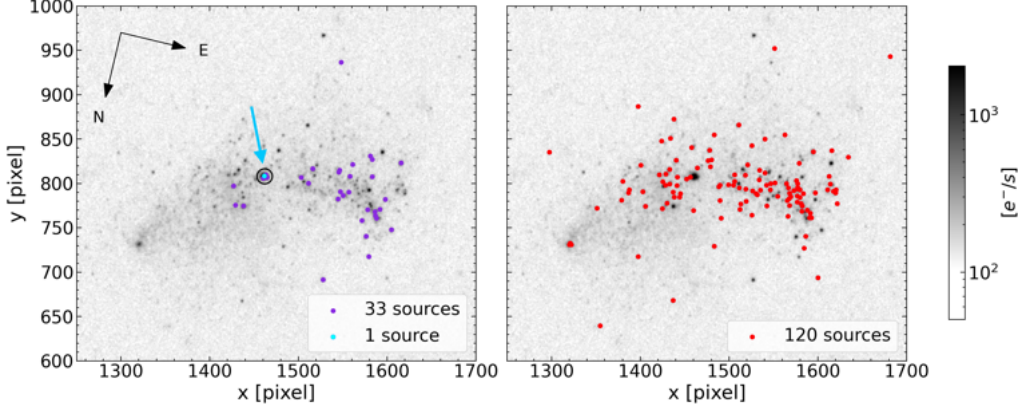


Figure 22: Spatial distribution of the HeB stellar population in Component C based on age classifications. The source younger than 6.3 Myr is indicated with a blue arrow and surrounded by a black circle, stars between (6.3 – 15.8) Myr are represented in purple and those older than 15.8 Myr are colored in red. The population is mainly scattered throughout the galaxy with the brightest source (potentially a cluster) located at the central part.

5. Color-Color Diagrams (CCDs)

Color-color diagrams (CCDs) are fundamental tools in astrophysics, elaborated through the combination of pairs of magnitudes between different filters. In this specific project, we decided to illustrate CCDs since they allow us to visualize how our stellar populations are distributed according to different color arrangements and how they are affected by reddening effects from dust. Here, we detect this impact through the analysis of the extinction behavior in different photometric bands according to two distinct extinction laws: one corresponding to the Milky Way (MW) and the other to the Small Magellanic Cloud (SMC). Our decision to compare these two models originates from a desire to evaluate how each affects our data when studying dust extinction. The SMC¹⁷ is a satellite dIrr galaxy of the MW, containing hot, massive blue stars and presenting a chemically primitive composition, resembling up to a certain extent how we envision our target, I Zw 18. The MW, on the other hand, is a barred spiral galaxy with a well-defined disk, bulge, bar and a surrounding extended stellar halo (Cimatti et al. (2019)). Therefore, it is particularly interesting to examine the differences and implications of applying a reddening examination to our data using two galaxies with such distinct characteristics.

As a first step, we generated Figure 23, which represents the normalized total extinction curves ($\frac{A_\lambda}{A_B - A_V}$) for the MW diffuse ISM (black solid line) – usually considered a standard reference – and the SMC bar (black dashed line) – reflecting the denser, star-forming region within the galaxy – as a function of wavelength (these curves were retrieved from the STScI Interstellar Extinction Curves¹⁸ archive). We also represented some transmission curves ($T(\lambda)$), also known as throughputs (colored curves). They describe how efficiently the filters transmit light for different wavelength ranges. Although we represented a few examples, we only worked with F225W, F336W and F438W, as stated in Sections 3.1 and 3.2 (throughput curves were retrieved

¹⁷ <https://www.stsci.edu/contents/media/images/2020/50/4759-Image>

¹⁸ <https://www.stsci.edu/hst/instrumentation/reference-data-for-calibration-and-tools/astronomical-catalogs/interstellar-extinction-curves>

from STScI System Throughput Tables⁷). This figure visually helps us identify how the extinction properties associated with the different models interact with the instrumental response of the filters, essential for estimating how dust affects real observations.

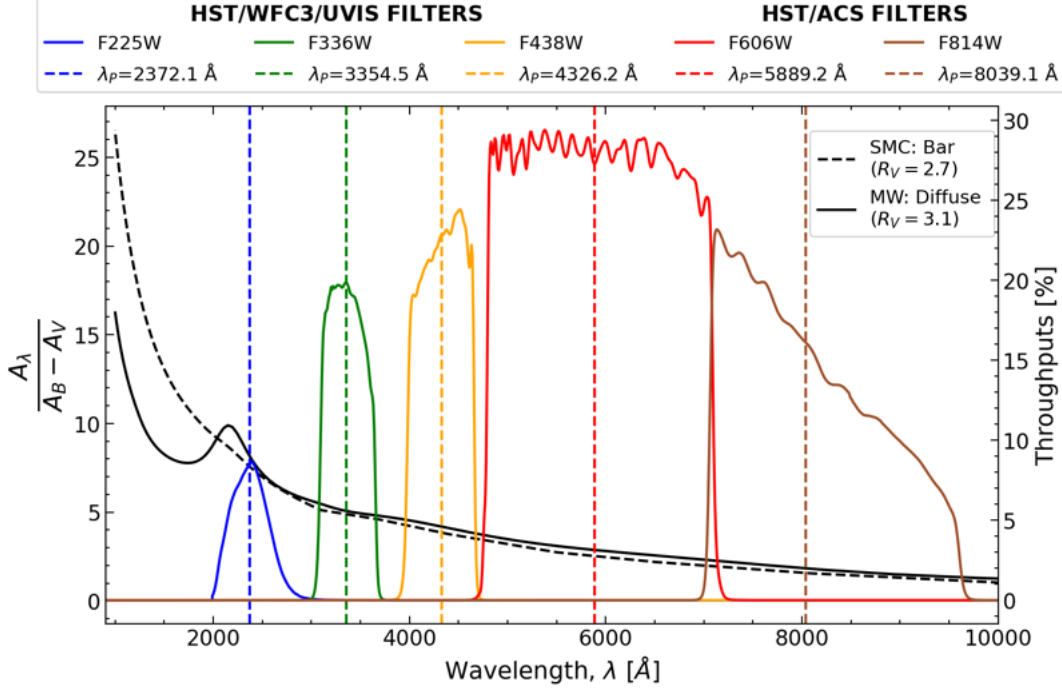


Figure 23: Representation of the extinction curves for the Milky Way (MW) diffuse ISM (solid black curve) and Small Magellanic Cloud (SMC) bar (dashed black curve), as well as the HST/WFC3/UVIS (red, green and orange curves) and HST/ACS (red and brown curves) filter throughputs as a function of wavelength. The vertical dashed colored lines indicate the pivot wavelength (λ_p) for each filter, labeled accordingly.

Extinction curves were retrieved from STScI Interstellar Extinction Curves¹⁸ and throughput profiles from STScI System Throughput Tables.⁷

The main goal of this part of the analysis, as previously mentioned, is to evaluate the effects of dust extinction. A way to proceed is through the evaluation of the reddening vectors associated with each extinction scenario. Reddening vectors, as outlined below, are constructed from the combination of color-excesses which, in turn, are defined as the subtraction of extinction values in different bands (see Eq. 3). Therefore, in order to accomplish this task, we required a precise evaluation of the extinction values for the wavelengths associated to each filter (A_λ). We started by using the filters' pivot wavelengths (λ_p^F) – i.e. the characteristic wavelengths of the filters (Tokunaga & Vacca (2005)) – and bandwidths (W^F) – defined as the equivalent widths of the filters, normalized by their peak throughputs – to define the maximum and minimum wavelength values for each filter (see Eq. 11). Both λ_p^F and W^F values were retrieved from Table 6.2¹⁹.

As shown in Figure 23, extinction curves show variations with wavelength. While the MW extinction law presents a prominent bump in the UV regime, the SMC bar not only lacks this bump but also shows a steeper rise in that same range, showing a stronger extinction at shorter wavelengths. This highlights the differences in dust grain properties and compositions of both galaxies. Additionally, this shows how certain regions

¹⁹<https://hst-docs.stsci.edu/wfc3ihb/chapter-6-uvvis-imaging-with-wfc3/6-5-uvvis-spectral-elements#id-6.5UVISSpectralElements-Table1footnote4>

in each extinction law contribute more than others to the observed signal depending on the filters and their sensitivity. Therefore, to properly account for this, we decided to compute a throughput-weighted average of the extinction curves over the wavelength range of each filter ($\langle \frac{A_\lambda}{E(B-V)} \rangle_F$). This was accomplished through Eq. 12, where we integrated the extinction curve weighted by the filter's throughput and normalized it by the total transmission. This yields an effective extinction value that reflects both the wavelength dependence of dust emission and the instrumental response of the filters (results can be found in Table 4).

$$\lambda_{\max, \min}^F = \lambda_p^F \pm \frac{W^F}{2} \quad (11)$$

$$\langle \frac{A_\lambda}{E(B-V)} \rangle_F \equiv \langle \frac{A_\lambda}{E(B-V)} \rangle_F = \frac{\int_{\lambda_{\min}^F}^{\lambda_{\max}^F} \left(\frac{A_\lambda}{E(B-V)} \cdot T(\lambda) \right) d\lambda}{\int_{\lambda_{\min}^F}^{\lambda_{\max}^F} T(\lambda) d\lambda} \quad (12)$$

	F225W	F336W	F438W
$\langle \frac{A_\lambda}{E(B-V)} \rangle_F :$	MW Diffuse ISM	≈ 8.288	≈ 5.107
	SMC Bar	≈ 7.621	≈ 4.894

Table 4: Rounded values of $\langle \frac{A_\lambda}{E(B-V)} \rangle_F$ for filters F225W, F336W and F438W under two different extinction laws: the MW diffuse ISM and the SMC bar.

However, to properly plot reddening vectors in CCDs, one needs to evaluate the extinction values in each filter (A_λ). During Section 2.5, we saw that the color excess ($E(B - V)$) was intimately related with the extinction in the V-band (A_V) and the slope of the extinction law (R_V) through Eq. 4. The MW diffuse ISM presents a value of $R_V = 3.1$ while that of the SMC bar is $R_V = 2.7$ ¹⁷. Assuming these R_V values, we infer the results for the color excess for each extinction law by presuming an extinction in the V-band of value $A_V = 0.1$. We can do this latter step because the A_V value here only affects the length of the reddening vector – that is, A_V simply scales the vector's magnitude in the diagram. Consequently, it is chosen purely based on visualization purposes. The actual direction and inclination of the vector is governed by the R_V of the extinction law chosen. Therefore, we end up obtaining the following results: $E(B - V) \approx 0.032$ for the MW diffuse ISM and $E(B - V) \approx 0.037$ for the SMC bar. Next, we apply Eq. 13 to determine the extinction in each filter ($A_\lambda \equiv A_F$ with $F \equiv F225W, F336W, F438W$) based on the interpolated weighted results (X , see Table 4) and the color excesses for each extinction law that we just derived. Once the A_λ values are computed for each filter, we can arrange them in pairs using Eq. 3 to evaluate different color excesses combinations (e.g. $E(F225W - F336W) = A_{F225W} - A_{F336W}$).

$$A_\lambda \equiv A_F \approx X \cdot E(B - V) \quad \text{with } X \equiv \frac{\int_{\lambda_{\min}^F}^{\lambda_{\max}^F} \left(\frac{A_\lambda}{E(B-V)} \cdot T(\lambda) \right) d\lambda}{\int_{\lambda_{\min}^F}^{\lambda_{\max}^F} T(\lambda) d\lambda} \quad (13)$$

After a series of tests, we ended up representing CCDs using the combination of $m_{F225W} - m_{F336W}$ (y-axis) versus $m_{F336W} - m_{F438W}$ (x-axis). Consequently, in order to compute the reddening vectors, we evaluated the sum of the color excesses along each axis. With this, we represented the CCDs for some of the most relevant spatial regions within our galaxy: I Zw 18 as a whole (see Figure 24) and its more relevant individual areas (Populations A, B, C and D; see Figure 25). Both plots show the stellar population distribution

in color (black dots), the reddening vectors for each of the extinction laws (MW in blue and SMC in red) and some overlaid MIST isochrones with no rotation (as justified in Section 4.3.2) and no pre-main sequence (PMS) contribution (in order to maintain clarity in the plot and facilitate a straightforward visual interpretation). Additionally, these isochrones account only for the foreground reddening ($A_V = 0.0992$). Throughout Section 4.3.1, we inferred the extinction by inspection, imposing a value of $A_V \approx 0.25$ in order to achieve a reasonable fit of the MS for I Zw 18's stellar population. In contrast, the analysis that we conduct here is specially aimed at studying and understanding the reddening effect itself. Therefore, aside from the foreground reddening value known, we do not assume any intrinsic extinction value *a priori*.

Moreover, each figure is divided into two panels: the ones to the left show the general CCDs whereas the ones to the right show the stellar population distribution after applying a SN cut in the F438W filter over 50 to highlight the brightest sources and thus the ones affected by the smallest photometric errors. We know this latter point, on one hand, from inspection of the results proposed in Section 4, where we could infer that the brightest sources were affected by the smallest photometric errors. Additionally, this can be easily demonstrated mathematically. From Eq. 14, we can derive that the apparent magnitude in a given filter (m_F) is defined according to the flux of the emitting source in that filter (\mathcal{F}_F) (see Eq. 14). Here, K is a calibration constant (Chromey (2016)). Using error propagation, we arrive to Eq. 15.

$$m_F = -2.5 \log_{10} (\mathcal{F}_F) + K \quad (14)$$

$$\sigma_{m_F} = \left| \frac{dm_F}{d\mathcal{F}_F} \right| \sigma_{\mathcal{F}_F} \underset{\text{Eq. 14}}{=} \frac{2.5}{\ln(10) \mathcal{F}_F} \sigma_{\mathcal{F}_F} \quad (15)$$

On the other hand, we define the SN – already introduced in Section 3.3.2 – as the ratio of the flux in each filter (\mathcal{F}_F) to its associated error ($\sigma_{\mathcal{F}_F}$). Introducing this in Eq. 15, we arrive to Eq. 16, where we have demonstrated that a SN = 50 for a given filter corresponds to a magnitude uncertainty of ≈ 0.02 . Furthermore, if we were to compute the color uncertainty for a couple of filters with the same SN threshold at 50 it would have a value of ≈ 0.03 via quadrature combination (see Eq. 17). As a result, this justifies the threshold imposition.

$$\sigma_{m_F} = \frac{2.5}{\ln(10) \text{SN}} \underset{\text{SN} = 50}{\approx} 0.02 \quad (16)$$

$$\sigma_{\text{color}} = \sqrt{2 \sigma_{m_F}^2} \underset{\text{Eq. 16}}{\approx} 0.03 \quad (17)$$

Additionally, the reason behind the decision of this SN cut in this particular filter is based on the fact that F438W, as previously mentioned throughout the project, is the most sensitive to redder stars compared to F225W or F336W. Therefore, by imposing that cut we are more likely to retain reliable sources without being unnecessarily too strict. This is so because if a star passes the SN condition, it is most probably also detected in the other two filters. Therefore, it allows for the inclusion of brighter sources even at longer wavelengths which would have been excluded had the cut been imposed on a bluer band. Consequently, it avoids compromising the sample size of stars that much while still imposing low photometric error data.

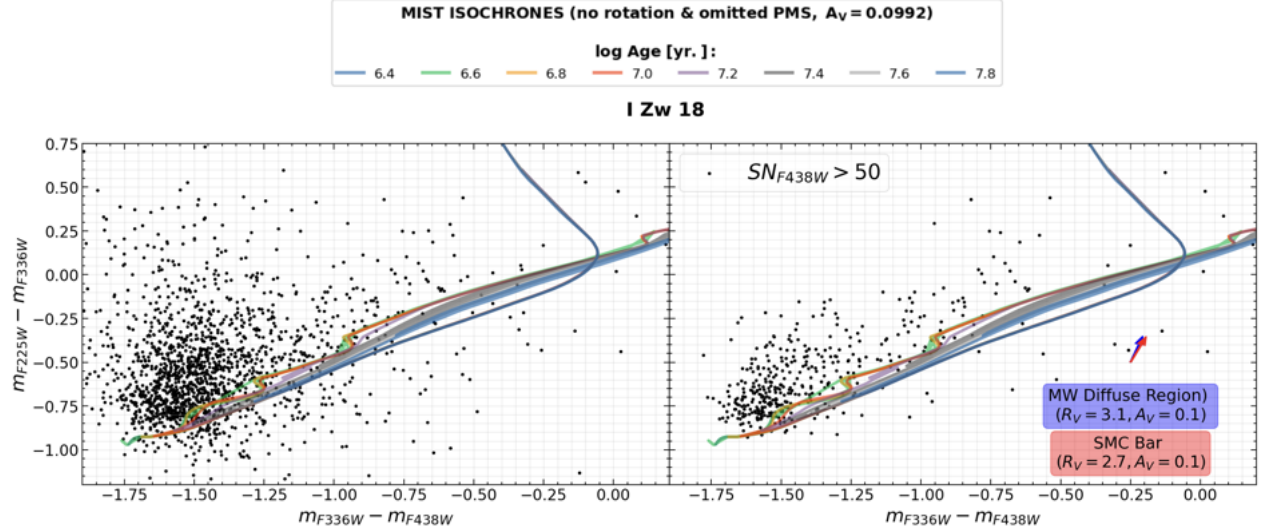


Figure 24: CCDs for I Zw 18 executed using colors $m_{F225W} - m_{F336W}$ and $m_{F336W} - m_{F438W}$, with overlaid MIST isochrones with no rotation, omitted PMS and foreground reddening $A_V = 0.0992$, color-coded by logarithmic age. The left panel shows all the recovered sources (above 50% completeness level) within the galaxy, whereas the right panel restricts the catalog by showing those that additionally pass a cut in SN in the F438W filter ($SN_{F438W} > 50$). The reddening vectors associated with the MW diffuse ISM (blue) and the SMC bar (red) extinction laws are shown in the right panel but they apply to both.

When analyzing the left-hand side panels in Figures 24 and 25, we can immediately appreciate a broadened distribution of the stellar sources. In the absence of internal dust, all stars would be expected to lie on or very close to the isochrones. Consequently, we can easily recognize that the positions of the stellar populations in our analysis are influenced by the combination of intrinsic stellar properties (i.e. brightness and colors of individual stars), their individual reddening by dust, crowding effects (especially in Populations A and C, and obviously present in the general view of I Zw 18) and photometric uncertainties (which scatter the sources, even sometimes below the theoretical isochrones). This dispersion complicates direct interpretation.

To analyze the dust reddening using reddening vectors, we usually place the tip of the vector at the position of one of the stars in the CCD. Then, we visually drag the star's position in the direction opposite to the arrow, by the same magnitude as the vector, until reaching the base of the arrow which indicates the intrinsic position of the star without reddening in the diagram. Therefore, this indicates that stars already below the isochrones would be dispersed even further downward if re-reddened, increasing their inconsistency with the model predictions. Consequently, we see that reddening alone does not explain the shift in the position of these stars in the CCDs and that many are most probably subject to photometric errors, specially at fainter magnitudes.

This is why we also display the stellar population distributions after applying a cut in SN_{F438W} (right-hand side panels). This threshold significantly reduces the scatter not only of the sources laying below the isochrones but also of those distributed in any direction very far from them. The resulting stellar samples in each spatial region, while smaller, provide a clearer picture and allow for a more reliable assessment of dust effects, due to a minimization of photometric noise. The stars that now present an offset from the isochrones are more prone to be principally affected by the internal reddening of each region, beyond the foreground component already assumed.

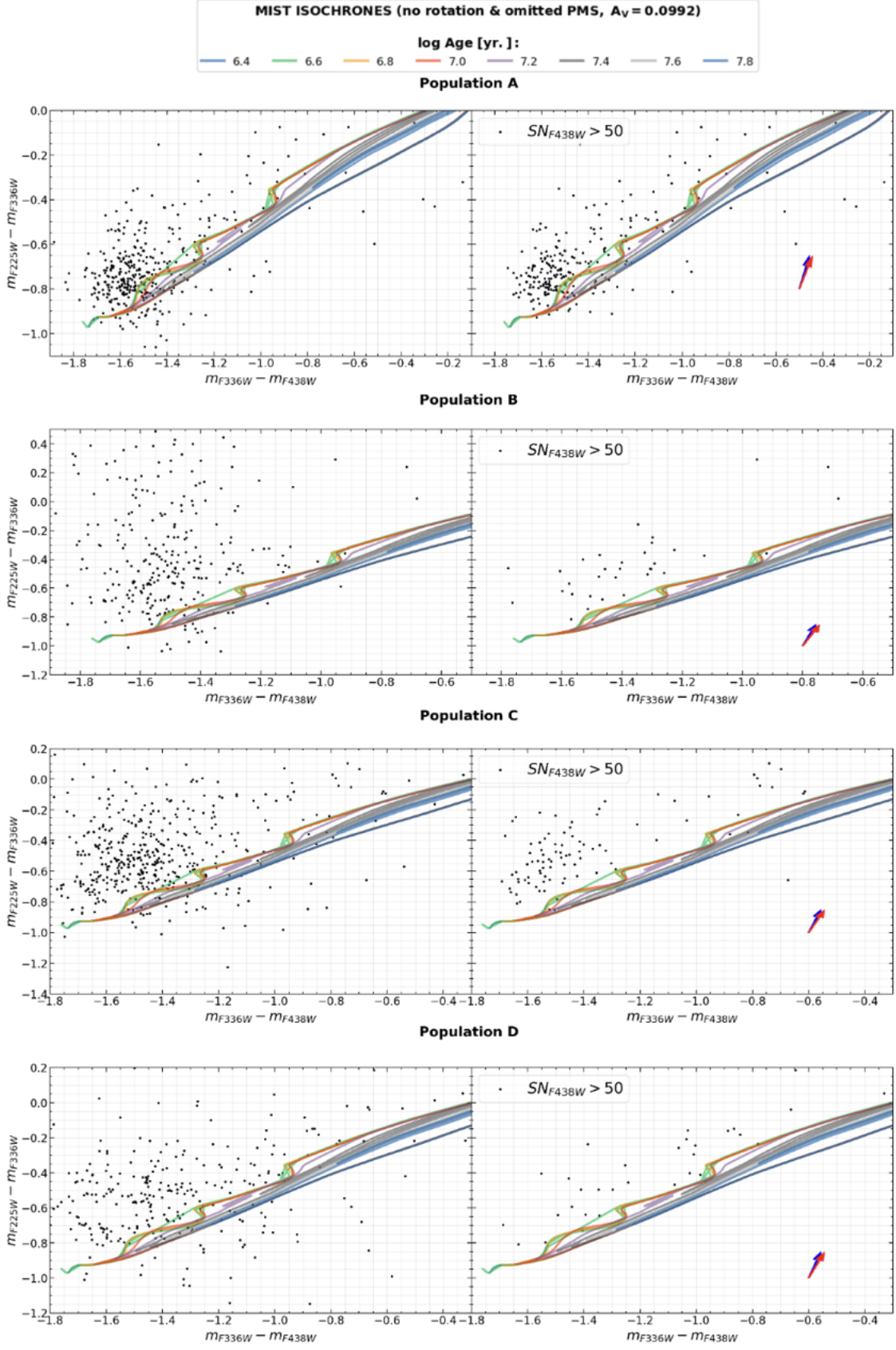


Figure 25: CCDs with reddening vectors for Populations A, B, C and D within I Zw 18 (see Figure 24 for a detailed description of each panel). Note that axis ranges vary between spatial regions.

In most cases, it can be visually inferred that the required extinction does not seem to exceed $A_V = 0.25$, agreeing with the imposed value in previous sections. For instance, in the case of I Zw 18's main body (see right panel in Figure 24), we can appreciate how most of the sources lay above the isochrones and how they all seem to be affected by an extinction value ranging between $A_V \in (0.1, 0.25)$, on average (with 0.1 referring to those stars laying just on top of the isochrones and thus subject solely to the foreground reddening, and 0.25 associated with those sources appearing more dispersed, accounting for extra intrinsic reddening). In the case of Population A (see first row, right panel in Figure 25), most of the sources are also distributed above the isochrones, covering the bluest colors (as expected due to the nature of its stellar population) and they are also generally affected by extinction coefficients ranging between the same values as stated before. According to Mateo (1998), some dwarf galaxies in the Local Group have uneven amounts of dust scattered around them, making some regions more affected by reddening than others. We additionally know that dust is important during the formation of H₂ clouds, which trigger star formation. Therefore, we would expect spatial regions such as Populations A and C (NW and SE areas) – which have the strongest star formation rates (as stated in Bortolini et al. (2024b) and further analyzed in Section 6) – to be subject to slightly higher reddening effects than the surrounding areas of the galaxy. More in particular, we would expect Population A to present a slightly higher reddening since it presents slightly younger stars compared to Population C. However, we can observe that the reddening seems to be somewhat higher in this latter region (see third row, right panel in Figure 25). A plausible interpretation could be that SN winds may have contributed to the dispersion of the dust within the galaxy. Moreover, the intense UV radiation from Population A could have led to an efficient dust destruction, reducing the reddening effect in that area. Furthermore, differences in the geometry of both regions could also be a key factor to consider, potentially influencing how dust is distributed within each one along the line-of-sight (LOS) to the observer. On the other hand, with respect to Populations B and D (second and fourth rows, right panels in Figure 25) we observe that the number of stars passing the SN cut and laying above or on top of the isochrones is rather low, challenging a proper analysis of the reddening effects in these regions. Nevertheless, we can overall conclude, for simplicity purposes, that the galaxy presents a rather constant reddening.

Interestingly, despite our initial assumption that the SMC would be significantly more distinct from the MW – and thus, provide a more accurate fit for I Zw 18 – we detect very little difference between the reddening vectors in both scenarios. While it is true that the extinction curve data used for the SMC corresponded specifically to its bar region – which could have influenced the outcome since it represented a very localized region – it is still quite striking to see such minimal variation. Therefore, the choice of extinction law has a rather limited impact on the qualitative interpretation of reddening in our case. Nevertheless, this study serves as a useful diagnostic.

6. Star Formation Histories (SFHs)

In astronomy, analyzing how the stellar populations in galaxies develop with time is one of the most intriguing disciplines, most commonly referred to as the study of the star formation history (SFH) of the source in question – which in our particular case is the dwarf galaxy I Zw 18. The SFR of galaxies changes with time due to multiple different effects – i.e. stellar feedback (Colling et al. (2018)) and gas accretion (Sánchez Almeida et al. (2014)) processes, which consequently alter the composition of the intergalactic and interstellar medium; the interaction with neighboring galaxies through mergers (Pearson et al. (2019)), etc. As a result, analyzing these changes enable us to piece together the galaxies' evolutionary paths, helping us reconstruct their history. Therefore, analyzing the SFH of a galaxy can be interpreted as an 'archaeological' approach (Cimatti et al. (2019)).

As inferred from the results presented in Section 4, the UV-CMD of I Zw 18 is dominated by young MS and blue loop (BL) HeB stars, spanning an age range of approximately (2.5 – 40) Myr for the resolved stellar population above the completeness level. Through the use of stellar evolution models and computational routines, we are able to reconstruct the SFH of the galaxy by modeling its observed CMD. We use a synthetic CMD fitting framework called SFERA2.0 (Star Formation Evolution Recovery Algorithm). Synthetic CMD fitting routines were originally used by Tosi et al. (1991). Later on, Cignoni et al. (2009) developed SFERA's code – used in works such as Cignoni et al. (2015), Cignoni et al. (2016), Cignoni et al. (2018) and Sacchi et al. (2018) – which has since been refined into its latest version: SFERA2.0. This updated version is the one we use in this analysis and has previously been tested in Bortolini et al. (2024a) and Bortolini et al. (2024b).

The synthetic CMD method is a powerful tool. Instead of assuming a functional SFH for the galaxy, the routine derives it empirically from a set of stellar evolutionary models, from which it generates a set of synthetic CMDs that are later on compared to the observed one. In our particular case, for consistency purposes, we maintained the MIST stellar evolutionary framework, containing a whole set of isochrones (with no rotation, see Section 4.3.2) and covering the whole range in ages and metallicities. However, for our run, we refined the selection by making it suitable for our galaxy. We choose a set of isochrones spanning from 10^6 yr to $10^{7.8}$ yr, and with two different metallicities ($[\text{Fe}/\text{H}] = -1.5$ and -1.6). On the other hand, this analysis assumes a Kroupa stellar mass distribution (Kroupa (2002)) between 0.2 M_\odot and 300 M_\odot and a series of stellar atmosphere models (Chen et al. (2019)). These latter ones enable the transformation from luminosities and temperatures to magnitudes and colors, respectively, for an appropriate construction of the synthetic CMDs. This framework also takes into account the potential presence of binary stars that, due to their close proximity to their companions, are unresolved. It does that by assuming that binaries contribute to 30% of the sample.

The age-range selection perfectly covered the whole CMD for our observed galaxy (recall from Sections 4.3.1 and 4.3.2). Moreover, we divided the age-range into five bins with progressively increasing, yet almost uniform, steps in the logarithmic space (the age boundaries were defined as: [6.00, 6.32, 6.65, 7.00, 7.37, 7.80]). This way, while the bins were almost equally spaced in logarithmic scale, their corresponding intervals in the linear scale grew exponentially, reflecting the increase in uncertainty as we increase the look-back time (see e.g. Cignoni & Tosi (2010)). Essentially, as we go to older epochs, we lose sensitivity and, thus, resolution. Stars become dimmer and they are increasingly affected by photometric errors, making the results less trustworthy than the ones detected for earlier epochs. This effect is even worsened for very distant galaxies as in the case of I Zw 18. As stated in Tolstoy (2009) “*The further the distance, the worse the crowding conditions and the shorter the look-back time reachable even with the deepest, highest resolution photometry*”. As a consequence, it seems reasonable to evaluate age bins that become broader towards the past, where sensitivity and reliability decrease. Additionally, we decided to relax the metallicity constraint by exploring a reasonable interval around the theoretical metallicity value (introduced in Eq. 9), derived from the results of previous authors who supported the idea that I Zw 18 has a surprisingly overall uniform metallicity (see Section 1).

The first step in this process consists of the use of the "Hess generator", which is essentially a routine that generates density maps of stars covering the CMD plane. In summary, the program relies on the statistical technique of Monte Carlo simulations. It randomly samples synthetic stellar masses from the assumed IMF, with ages and metallicities arbitrarily chosen from the intervals defined above. Based on stellar evolution models, these stars present different lifetimes and the program focuses on interpolating the properties of each star along the different isochrones. In the end, the main objective is to progressively populate the different isochrones with stars of different masses. We denote these CMDs "raw models" since, up to this point, they do not take into account the physics underlying our problem nor the observational uncertainties. For instance,

the galaxy's distance, its intrinsic reddening, the photometric errors, and the completeness limitations caused by crowding and observational distortions from the telescope all impact our observed data. However, these factors are not yet accounted for in these raw models. Therefore, next step consists of their convolution with the completeness thresholds and photometric errors inferred from the ASTs (see Section 4.1).

The results are the so-called “dirty-models”. As with the raw ones, dirty-models populate the different isochrones taking into account the real photometric limitations of our sample, as well as the distance modulus of our galaxy ($\mu_0 = 31.30$ mag, Aloisi et al. (2007)) and reddening effects. More specifically, given the confirmation in Section 5 that our galaxy presented an intrinsic extinction contribution, we assumed an extinction of $A_V = 0.25$ as a reasonable general value and the MW law for simplicity purposes, since previous results indicated minimal variation compared with the SMC model ($R_V(MW) = 3.1$). As a result, using Eq. 4 we defined the color excess as $E(B - V) = 0.0806$.

Consequently, up to this point, we presented a set of convolved synthetic CMD models (model Z, A) indexed by metallicity ($[\frac{Fe}{H}] \equiv Z$, to simplify the notation) and age (A). The following step consisted on utilizing the SFERA2.0 software. Our first approach began by dividing the observational CMD into a 2D grid, where each cell (identified as (i, j)) contained a specific number of observed stars. We defined the grid by allowing the color to range from $(m_{F225W} - m_{F438W}) \in [-4, 2]$ in steps of $\Delta\text{color} = 0.25$ and by allowing the magnitude to range from $m_{F438W} \in [20, 31]$ in steps of $\Delta\text{mag} = 0.5$. SFERA2.0’s primary goal consists in estimating the optimal combination of synthetic dirty models – hereafter referred to as "models" for the sake of notational simplicity – that best reproduced the number and characteristics of the stars in each of these cells. Therefore, the CMD models were binned in the exact same way as the observed one. The fitting procedure, on the other hand, involves adjusting how much each individual model contributes in each cell through the use of weights ($w_{Z, A}$). The weights specifically represent how much each individual model (model Z, A) contributes to the construction of the final combined model in each cell ($M_{i, j}$). In turn, after arranging all the cell’s final combinations ($M_{i, j}$), we can construct the final model for the galaxy’s CMD (M_{CMD}). Our objective is to properly reconstruct the detected stellar component of the observed CMD (see Eq. 18). For this reason, it is crucial to optimize the weights, since our goal is to minimize the difference between the observed CMD (O_{CMD}) and M_{CMD} .

$$M_{CMD} = \sum_{i, j} M_{i, j} = \sum_{i, j} \left(\sum_Z \sum_A (\text{model}_{Z, A} \cdot w_{Z, A}) \right) \quad (18)$$

Traditional gradient-based minimization methods are inadequate for these situations since they tend to get trapped in local minima and progressively get less efficient as we increase the size of the parameter space. Instead, genetic algorithms like PIKAIA, used in SFERA2.0 and inspired by the fundamentals of natural selection and genetics (Charbonneau (1995)), are considered a better suited type of optimization algorithm to explore our complicated parameter space. It is initialized with a randomly generated set of candidate solutions (a set of weights), analogous to a number of people in a population (N_{pop}). Then, the code tests different combinations of the weights, calculating how good or bad the matches with the observed data are (that is, the fitness) through a merit function, which in the case of SFERA2.0 is a Poissonian likelihood (see Eq. 19, where $O_{i, j}$ and $M_{i, j}$ represent the observed and modeled stellar counts per grid cell in the CMDs). This likelihood is chosen based on the fact that star counts in each of the cells of the 2D grid are discrete, typically following Poissonian statistics (Chromey (2016)).

As we were stating earlier, we require the merit function to be minimized in order to find the best-fitting set of weights. This is so because the lower the value of the merit function, the better the match is. Therefore, the candidates with poorer finesse are discarded, whereas the ones with a better one are selected for reproduction,

introducing a new generation of solutions (analogous to the offspring of the initial population). As in nature, random mutations are occasionally introduced in the code in between generations to maintain diversity and prevent a premature convergence to a local minima. This helps generate as reliable results as possible. These mutations may include replacing a weight value by a randomly selected one, or performing crossover between high and low fitness parents (Charbonneau (1995)). Therefore, this "breeding" process goes on for a set number of generations (N_{gen}) until convergence to an optimal solution is reached.

$$\chi_P = \sum_{i,j} O_{i,j} \ln \left(\frac{O_{i,j}}{M_{i,j}} \right) - O_{i,j} + M_{i,j} \quad (19)$$

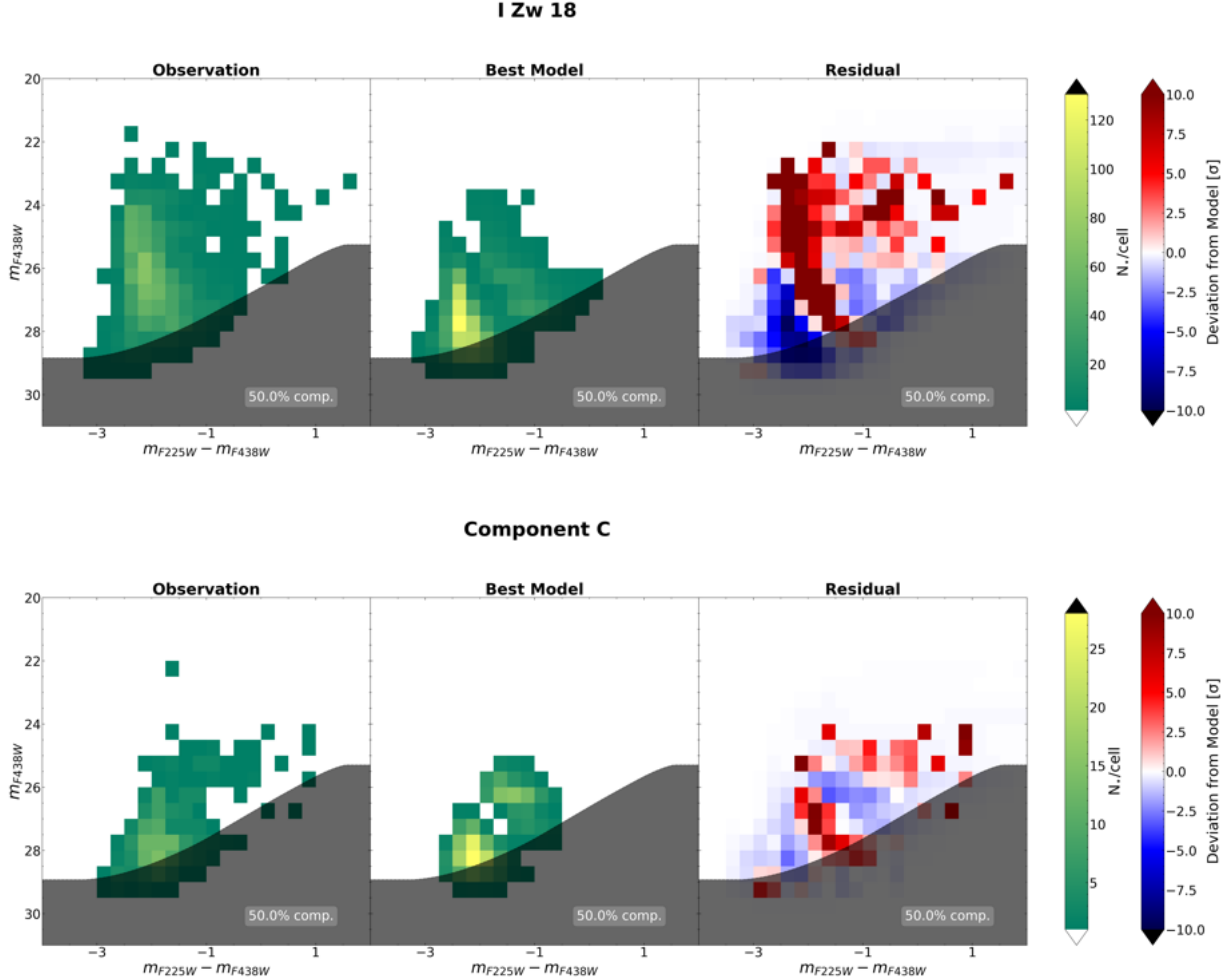


Figure 26: Comparison between the observational CMD and SFERA2.0's best fit CMD model. The top row belongs to I Zw 18's main body, whereas the bottom row displays the information for its companion galaxy, Component C. Each panel shows a density plot histogram, with the x-axis representing the color ($m_{F225W} - m_{F438W}$) and the y-axis the F438W magnitude (m_{F438W}). The left panel presents the observed data (inferred from photometric analysis and first analyzed in Section 4). The middle panel shows the synthetic model prediction. The right panel, on the other hand, displays normalized residuals following Eq. 20 pointing out the cells with the most significant difference in stellar counts with colors ranging from dark red (excess of observed stars compared to the model) to dark blue (deficit of "real stars"). The shaded gray areas show the 50% completeness estimations.

During this part of the project, we executed SFERA2.0 in order to estimate some preliminary results. More in particular, some CMD fits for I Zw 18's main body, its companion galaxy Component C, and I Zw 18's two main star-forming regions: Populations A and C. The first two are shown in Figure 26, whereas the last two are displayed in Figure 27. It is important to note that SFERA2.0 performs bootstrap resampling. This is a feature that consists of exploring the parameter space more exhaustively by re-running the code as many times as you want (we decided to do it for 5 times) while slightly perturbing the real CMD. For instance, the software could deliberately decide to omit some random real stars to check the consequences in the final fit, or even sometimes slightly decide to modify the cell sizes. In summary, bootstrapping is a technique that randomly shifts the nature of the real CMD. All of these examples introduce random Monte Carlo noise which actually helps the code to run smoothly. These bootstraps solutions are then averaged to produce what is referred to as the "best model", representing the fit that more accurately matches the observational data. Additionally, out of the best-fit model, the software provides some percentiles that later on serve as good estimates of the uncertainties.

Each figure is divided into three panels, each showing 2D histograms displaying cells color-coded by density, meaning that each cell shows the number of stars present there using a color scale. The panel on the left represents the observational data for each region of interest (analogous to the plots shown in Figures 11 and 12). The middle plot displays SFERA2.0's best fit model. For these two first panels, we represent the absence of stars in white and the increase of stellar density going from green to yellow, with densities exceeding the upper threshold color coded in black. The panel on the right, on the other hand, shows the normalized residuals, calculated using Eq. 20, where the significant differences between the observed data and the model are highlighted. Eq. 20 represents a standard statistical technique. According to Chromey (2016), if we assume our data to follow Poissonian statistics – which we can given its behavior as discrete events (stars) per cell – then we can say that its variance (σ^2) is equal to its mean ($\mu \equiv M_{i,j}$), with $M_{i,j}$ the number of counts per cell of the final model. This way, we can define the standard deviation as $\sigma = \sqrt{M_{i,j}}$ and standardize the residuals by multiplying them by the expected fractional uncertainty ($M_{i,j}^{-1/2}$). This way, the color-map for this panel attributes redder colors when there is an excess of stars in the observed data cells compared to the model, and blue colors when there is a deficit. Here, white cells also show the absence of stars and the very dark colors exhibit densities that exceed the upper and lower limits. Additionally, all the panels show overlaid 50% completeness estimations as shaded regions, as studied along Section 4, with all the sources laying below the threshold being excluded from the following analysis.

$$\text{Residual} = \frac{O_{i,j} - M_{i,j}}{\sqrt{M_{i,j}}} \quad (20)$$

It is immediately evident from the middle panels in Figures 26 and 27 that the model fits are not ideal, particularly in their failure to reproduce the brightest sources seen in the observational panels to the left. Instead, the models tend to overpopulate the lower part of the CMD. However, it is relevant to mention that although this can be appreciated in the four spatial regions analyzed, it seems more evident for I Zw 18's main body and the companion dwarf galaxy Component C (see Figure 26). It seems that the key factor influencing these discrepancies is the treatment of completeness across the entire FOV. Both I Zw 18's main body and, to a lesser extent, Component C, exhibit significant variations in stellar density since they represent the overall galactic regions. Consequently, fitting a single model across such heterogeneous regions leads to poor completeness corrections, especially in the most crowded areas in the CMDs where it is harder to detect faint stars. Therefore, this might be the principal reason why the models underestimate the brightest clump in the CMDs and mistakenly overestimate the lower end. In contrast, Populations A and C (see Figure 27) represent more localized regions within I Zw 18, with relatively uniform stellar densities, which is why here the fits improve noticeably, providing a better (although still not perfect) match to the observed CMD.

Moreover, as had already been discussed, the brightest – also most massive – sources were intimately related with strong stellar winds and potentially intense rotations. These characteristics, together with their short lifespan features, makes these stars hard to model. This, together with the completeness phenomena described above, might be an additional reason why these stars are not that well-fitted.

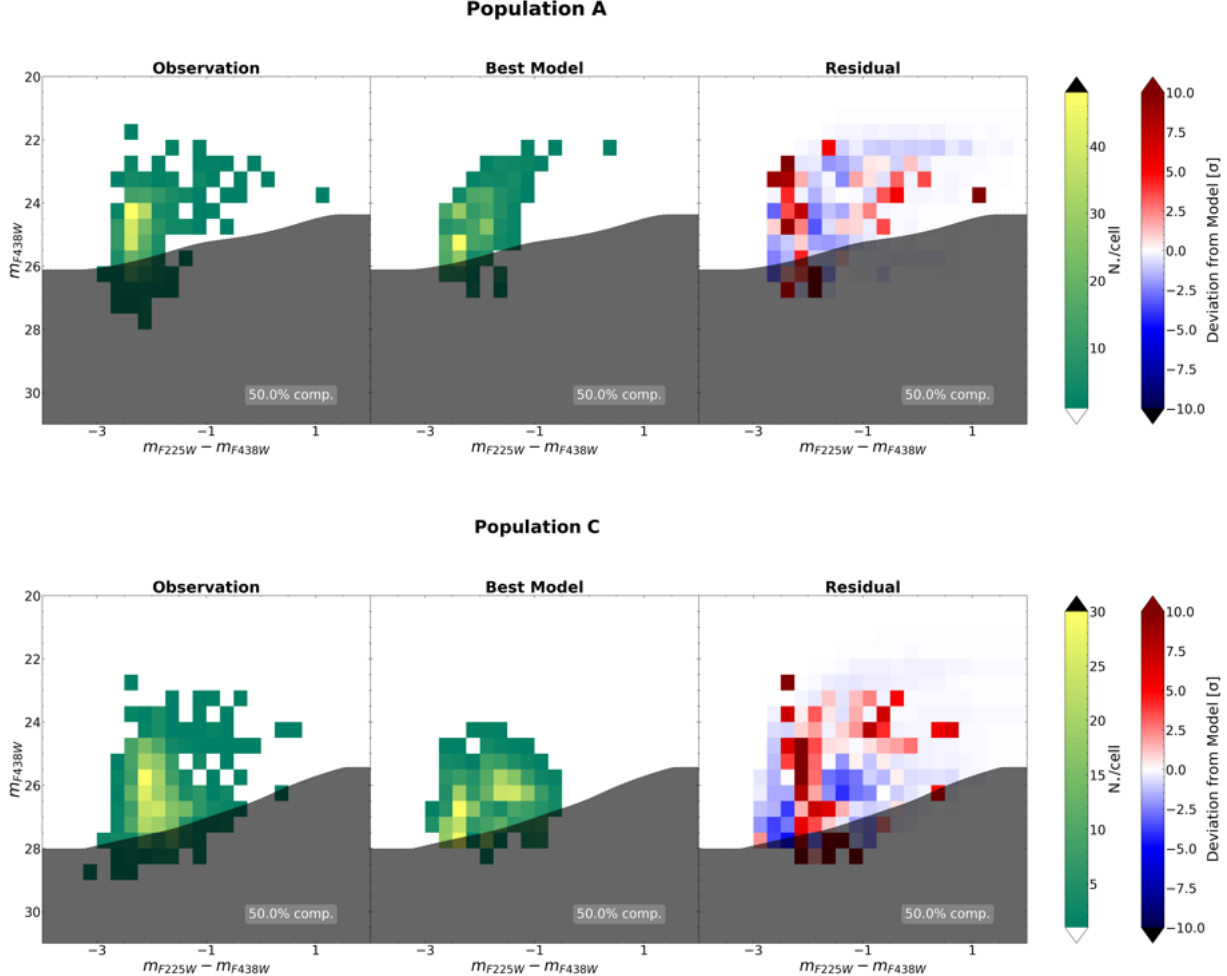


Figure 27: Comparison between the observational CMD and SFERA2.0’s best fit CMD model. The top row belongs to Population A, whereas the bottom row displays the information for Population C, both representing the highest star forming regions (see Figure 26 for a detailed description of each panel).

On the other hand, when analyzing the panels to the right, we can easily detect an interesting behavior. Ideally, we would want the histograms to display random distributions of red and blue shaded cells with different intensities, representing random noise. However, the sharp blue and red areas shown are mainly attributed to the completeness phenomena recently introduced. In fact, this characteristic structure remaining in the data is much more evident in Figure 26 than in Figure 27 as previously commented. Apart from having difficulty accurately characterizing the bright clump, the model also seems to struggle when trying to fit the color of the MS properly. An explanation for this could be related with the age-metallicity degeneracy. We know that metal-rich stars are usually red and can sometimes be mistaken for older, cooler sources. The same happens with metal-poor stars, which tend to be bluer and can be misclassified as younger, hotter sources (Cignoni & Tosi (2010), Cimatti et al. (2019)). As a consequence, it is complicated to discern between different stellar types. A proper solution might involve resolving the MS turn-off point. When fitting the MIST isochrones

(see Section 4.3), we could see that all the different isochrones were tightly displayed around the MS turn-off, meaning it was difficult to differentiate between their different temperature/color properties. This is already difficult to solve for galaxies within the Local Group, so at the distance of I Zw 18 it is impossible with the current state-of-the-art telescopes.

Additionally, we imposed two different metallicity values to allow for the software to evaluate the best model. However, it is possible that for the software this was not enough, probably requiring a more precise value in order to fit the data more accurately. Another possibility might be that the metallicity range we chose was fairly tight and it might have been more favorable to provide the software with a more distinct value such as $[Fe/H] = -2$. Moreover, we also assumed an extinction value of $A_V = 0.25$. This, although consistent with the results presented in Section 5, is likely to vary between the different spatial regions (as already mentioned during that analysis), and even from star to star. Therefore, this choice could have also affected the accuracy of the model during its construction. We should not forget about our IMF definition and the percentage of binary systems allowed. Perhaps these values could benefit from some refinement, potentially improving the precision of the models.

We should also mention that, when using SFERA2.0, we initialized the program by introducing $N_{pop} = 50$ (initial random set of candidate solutions) and let it perform these runs for $N_{gen} = 150,000$ generations. While reasonable as a first attempt, some better analysis could be pursued, perhaps increasing the number of generations. The selection of a proper grid size during the analysis is also key. As previously stated, the software is fundamentally based on the count of stars per grid cell and the subsequent comparison between the observational and model results. Consequently, enabling a suitable grid size is key to allow for a reasonable number of stars to fall in each cell. We require cells which are sufficiently big so that a reasonable number of stars are present but still sufficiently small so that the CMD details are not omitted. Keeping a balance is, however, challenging. Even when choosing an adequate grid size, the stellar population distribution within the CMD is not homogeneous and some areas are more crowded than others, meaning that those with less stellar density can trigger the fit. Especially within the brightest clump, we are more prone to having underpopulated cells. These low numbers lead to Poisson noise, which introduces random fluctuations and reduces the reliability of the model, compromising the fit. As a result, improvements in the binning could be introduced. We conclude that all of the above are some of the main reasons why we expect the model not only to fail when fitting the brightest clump, but also to struggle when characterizing the different colors within each stellar population.

When running SFERA2.0, the software not only returns the best model for fitting the observational CMD but also a set of parameters, among which we have the mean SFR and some percentiles per age bin, derived from the bootstrapping technique introduced above. This way we can construct the panels shown in Figure 28. These show the mean SFR distribution in each defined age bin as a function of the look-back time (going to older epochs from left to right), represented with a solid black line. Additionally, we plot the shaded region between the 16th and 84th percentiles of the distribution in red. These serve as a good estimate of the uncertainties, representing a confidence interval.

At first glance, we can observe very distinctive differences. I Zw 18's main body presents a mild SFR ($\approx 0.017 M_\odot/\text{yr}$) around (23.4 – 63) Myr ago, which progressively increases until reaching a peak of star formation activity ($\approx 0.057 M_\odot/\text{yr}$) around (4.5 – 10) Myr ago. Then after a brief period which seems to be characterized by inactivity a second burst occurs, this time slightly weaker ($\approx 0.039 M_\odot/\text{yr}$) around (1 – 2) Myr ago. This behavior could be expected, given the variety of stellar populations present, which covered different stellar isochrones as previously analyzed (see Section 4.3). Component C, on the other hand, shows a different character. To begin with, it presents a noticeable drop in its SFRs. It goes through a rather quiescent star-formation episode ($\approx 0.0026 M_\odot/\text{yr}$) about (23.4 – 63) Myr ago, that is radically increased, reaching a SFR of $\approx 0.019 M_\odot/\text{yr}$ from (10 – 23.4) Myr ago. Although still considerably low

compared to I Zw 18's main body, it is still remarkable given its inactive behavior. When comparing these two main galaxies we can infer that despite distinct, they follow analogous tendencies until 10 Myr ago. For the last 10 Myr, there is no sign of SF within the companion.

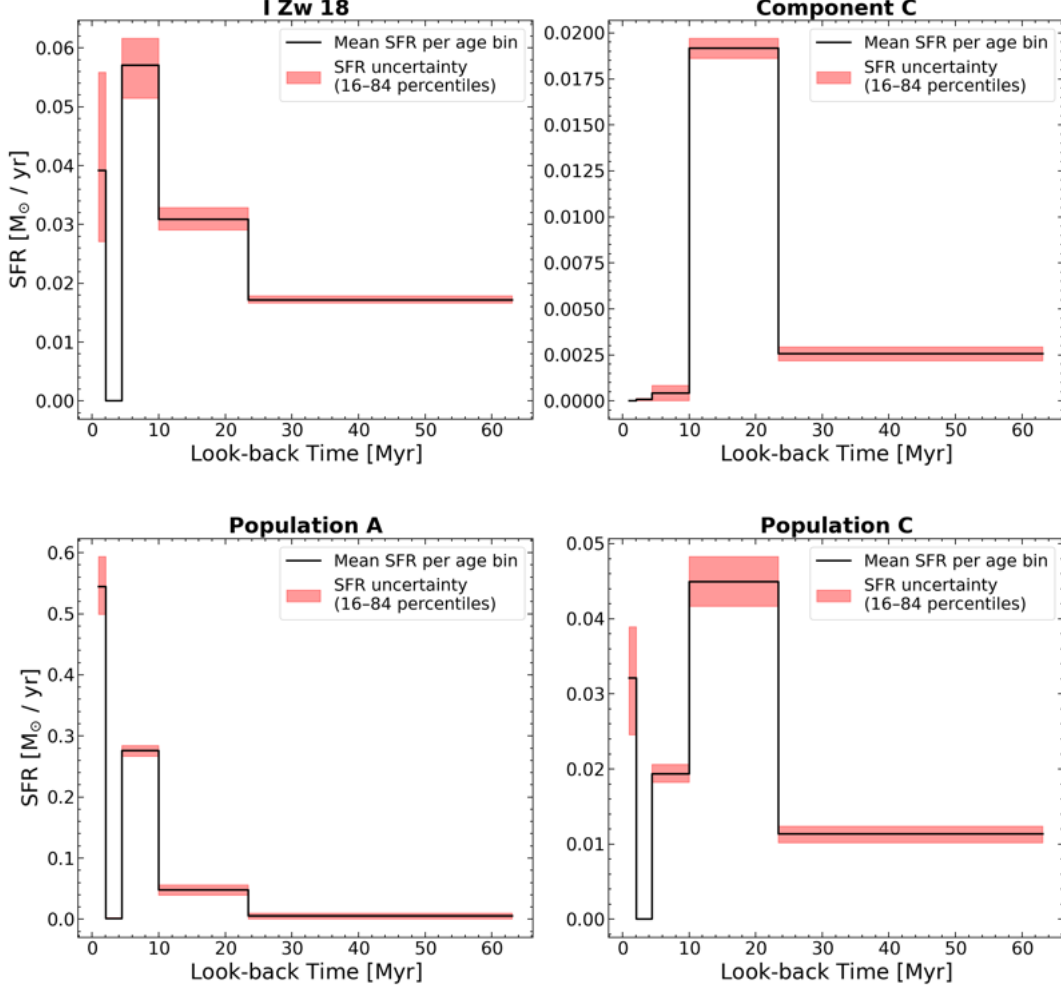


Figure 28: Representation of the SFHs of I Zw 18's main body (top-left), Component C (top-right), Population A (bottom-left) and Population C (bottom-right). These are shown through the representation of the SFRs of each region per age bin (black solid line) as a function of look-back time. The corresponding uncertainty ranges are shown as red-shaded areas between the 16th and 84th percentiles in each age bin. All the panels reveal variations in the SFR over the past ≈ 63 Myr.

This behavior is in agreement with the idea that Component C's stellar formation got truncated because of a starvation period where the main body started consuming its companion pristine gas. This is perfectly shown in the diagrams, where I Zw 18 doubles its SFR exactly when Component C gets quenched, at about 10 Myr ago. Additionally, according to Lelli et al. (2012), the central H_I column density in I Zw 18 is an order of magnitude higher than in Component C. This can be verified in the right panel of Figure 29, where we can appreciate that Component C (indicated with a letter C at the top right corner) is embedded into an H_I density contour of $6 \cdot 10^{20}$ atoms/cm², whereas I Zw 18 (indicated with a letter A at the bottom left corner) quadruples the value ($\approx 24 \cdot 10^{20}$ atoms/cm²) for the its main body, even reaching values of $48 \cdot 10^{20}$ atoms/cm² for its two highest star-forming regions (Populations A and C, represented as inner top

and bottom contours within I Zw 18, respectively). Consequently, this lack of gas concentration in Component C is most probably the main reason for the recent inactivity in the companion galaxy. These results were already anticipated during the HeB star discretization analysis (see Section 4.4), where we detected that Component C's stellar population was considerably "older" than that present in I Zw 18's main body.

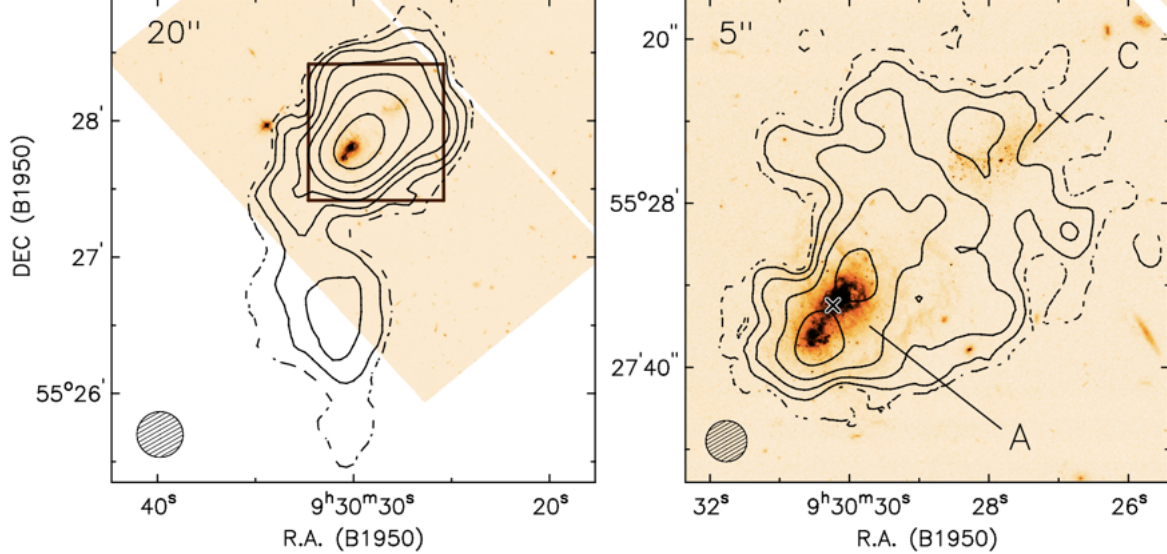


Figure 29: Figure retrieved from Lelli et al. (2012) showing the maps of the integrated H_1 emission within the FOV of interest surrounding both galaxies: I Zw 18 (bottom left corner of the black box) and Component C (top right corner of the black box). The panel to the left displays the area at a resolution of $20''$ whereas the right-hand side panel zooms into the black square region, with a resolution of $5''$. As stated in Lelli et al. (2012), the contours in the higher resolution map (right panel) are at 3 (dashed), 6, 12, 24, $48 \cdot 10^{20}$ atoms/cm 2 .

On the other hand, when comparing Populations A and C we can also detect some interesting features. These two regions encompass the NW and SE areas within the main body, respectively, characterizing what has previously been defined as the regions with the highest SFRs. This can be perfectly seen in Figure 28. Prior to 23.4 Myr ago, the stellar formation activity both in Population A and C was minimal, with Population C presenting a slightly higher and steady rate ($\approx 0.006 M_{\odot}/\text{yr}$ and $\approx 0.011 M_{\odot}/\text{yr}$, respectively). Between (10 – 23.4) Myr ago, the SFRs in both regions increased to comparable levels ($\approx 0.048 M_{\odot}/\text{yr}$ for Population A and $\approx 0.045 M_{\odot}/\text{yr}$ for Population C). Since then, we can appreciate that Population C has experienced what appears like a moderate SFR decline while Population A experienced its first star-formation peak ($\approx 0.276 M_{\odot}/\text{yr}$) around (4.5 – 10) Myr ago, followed by its latest, most current outburst ($\approx 0.544 M_{\odot}/\text{yr}$) around (1 – 2) Myr ago. This is consistent with the results provided by Bortolini et al. (2024b).

As we can see, both populations undergo a reasonable rate of stellar formation at rather young epochs, with Population A being the most recent and most intense and Population C being the next one in relevance, although considerably weaker. It is important to mention that it is possible that the lack of SF in Population A at ages older than 23.4 Myr might be due to completeness and crowding effects. This means that there could potentially be more stars being formed at those epochs but that we are unfortunately unable to resolve and therefore go unnoticed in our study. Inversely, the crowding and completeness are not as severe for Population C, which can be the reason why the SFR sensitivity is slightly enhanced towards older epochs for this region. Nevertheless, we had already analyzed that Population A presented the bulk of the youngest,

bluest sources present in the galaxy during the isochrone-fitting procedure (see Section 4.3), which we now verify. Moreover, the discrepancy between I Zw 18’s main body and Population A highlights the relevance of completeness estimates. I Zw 18’s completeness represents the full FOV coverage of the galaxy, which logically fails to accurately represent the conditions within Population A. As a result, a significant portion of the most recent stellar formation activity in this latter region is underestimated in I Zw 18 by a factor of 10 approximately.

It is important to note that, due to the limitations in the photometric data and our decision to focus on the UV/blue region of the spectrum, we are unable to retrieve information or place any constraints to the stellar-formation properties within the galaxies at epochs older than about ≈ 63 Myr ago. Of course, this does not imply that star formation did not occur at earlier epochs. In fact, the SFRs inferred along this analysis most probably just indicate the latest activity detected within the galaxies. With the use of filters extending along the near-infrared (NIR) (as in the study carried out by Bortolini et al. (2024b), where they probe star formation at epochs older than 1 Gyr) it is possible to gain further sensitivity into older epochs where evolved stars are still bright. Likewise, with the advancement of technology and observational instruments, we hope that in the future we will achieve an improved resolution power, enough to explore older epochs of such distant galaxies in more detail. We should not forget that these results have been inferred from the execution of the SFERA2.0 routine. As have previously been discussed, there were certain assumptions we had to make in order to execute the program. These may have affected the accuracy of the results up to a certain extent. Therefore, we conclude that the findings presented in this section should be regarded as preliminary while, ideally, further analysis should be required to obtain more precise and reliable results in future studies.

7. Conclusions and Future Work

Along this thesis, we examined I Zw 18, a blue compact dwarf galaxy of great interest within the scientific community, primarily due to its recent SFRs despite its low metal-abundance. Despite having been studied through photometric analysis by previous researchers, mainly focusing on the optical (Hunter & Thronson Jr (1995), Aloisi et al. (1999)) and NIR range (Östlin (2000), Bortolini et al. (2024b)), in this project we decided to target the UV-blue part of the spectrum by analyzing the galaxy using the HST/WFC3 detector. More specifically, we employed the UVIS (UV and visible) channel to ensure a more precise detection of the youngest, bluest and brightest stellar portion of the galaxy. This approach had not been explored before and could be accounted as a complimentary study to previous works.

We mainly used a PSF fitting routine called DOLPHOT2.0, which enabled us to characterize the potential point-like sources within our galaxy, and after a series of parameters constraints and spatial region characterization processes (see Section 3.2), we arrived at a series of catalogs with our final data. On the one hand, we executed CMDs (see Section 4) with the filters F225W and F438W and proceeded to investigate the stellar populations present within I Zw 18’s main body and its companion galaxy, Component C (see Figure 11). Moreover, we dedicated some time to analyze specific spatial regions inside I Zw 18, more specifically those associated with the strongest and most recent stellar formation episodes – clearly more crowded in appearance – denoted as Populations A and C (see Figure 12). To do this, we implemented an analysis where we overlaid some isochrones – retrieved from the MIST and PARSEC frameworks – on top of the CMDs (see Section 4.3). The similarities between both models (see Figure 14) and the possibility of studying the stellar rotation feature led us to stick with the MIST models instead.

Using them, we observed that overall I Zw 18 hosted a stellar population above a 50% completeness level – indicating resolved stars – with ages ranging from ≈ 2.5 Myr to ≈ 40 Myr. This confirmed that, through these filters, we were indeed able to focus on the youngest and bluest stellar population within the galaxy.

We saw that a significant fraction of stars reached magnitudes of around $m_{F438W} \approx 22$, indicating genuinely luminous sources. Furthermore, to improve the isochrone fitting with respect to the MS population we decided to introduce an extinction parameter of $A_V = 0.25$ – selected based on visual inspection.

Moreover, through evolutionary track fitting (see Figure 17), we observed that these resolved stars spanned a mass range from around $8 M_\odot$ up to $140 M_\odot$ (potentially reaching higher values). This pointed to a substantial number of massive stars within the stellar population. Additionally, when evaluating the effects of rotation, both in the isochrone and track fitting, we found that when the feature was habilitated, the models became less capable in reproducing the most luminous, youngest, and most massive stars within the CMDs. This discrepancy, along with the possibility that these sources could potentially be WR stars, on the one hand, suggested that the velocity implemented might not be high enough to account for the characteristics of these stellar type. We additionally argued, based on Chiappini et al. (2006), that metal-poor stars could reach rotational velocities of the order of $(600 - 800)$ km/s, supporting this idea. Moreover, stellar winds in massive stars could contribute to the difficulty in accurately fitting these sources. Such winds could lead to mechanical and radiative decoupling of the stellar core and envelope, and this, together with the shorter lifespans of blue massive stars, could hinder proper modeling for these stars. We also noted that the distance at which this galaxy is located and its low metallicity could present a challenge, especially when trying to fit it with frameworks that had only been calibrated with systems from the Local neighborhood, presenting completely different characteristics.

Later, during the project, we aimed to evaluate the spatial distribution of stars differentiated by age. To do so, we mainly focused on those slightly more evolved from the MS: HeB stars (see Section 4.4). The reason to make this age distinction for HeB stars was due to the fact that the isochrones appeared quite indistinct near the MS region, making the age classification more challenging. For the case of I Zw 18’s main body, we identified HeB stars by applying a discretization method based on the 50th percentile of the population’s distribution in the CMD (see Figure 19). This roughly separated both stellar phases (MS and HeB) based on where most of the stars laid, which was around the MS since it represents the stable phase were they spend the majority of their lifetimes. For Component C, on the contrary, due to its much lower stellar density, we executed the division by applying a color cut at $m_{F225W} - m_{F438W} = -1.9$, since the percentile technique was less appropriate in this case (see Figure 21). Therefore, we then divided their stellar populations into different age groups.

I Zw 18’s stars were color-coded in cyan when they were younger than 6.3 Myr, in green when ranging between $(6.3 - 10)$ Myr, in pink when ranging between $(10 - 15.8)$ Myr and in red when representing those stars older than 15.8 Myr. This way, we could confirm that the two youngest stellar groups (cyan and green) were spatially distributed around the NW and SE regions within the galaxy, as expected since these regions were known to host the most recent and active star formation within the galaxy. We also saw that, as the stellar ages increased (pink and red) – though still considerably young overall – the stars became more spatially dispersed around the outskirts, consistent with the expected patterns of stellar evolution (see Figure 20).

In the case of Component C, we were only able to distinguish between those stars ranging around $(6.3 - 15.8)$ Myr (purple) and those older than 15.8 Myr (red), unable to categorize them in more precise age bins due to the lack of resolved sources available. This already suggested a generally "older" stellar population compared to that of I Zw 18. In fact, only one source was identified as possibly younger than 6.3 Myr (cyan). However, upon analysis, it appeared to be a stellar cluster rather than a single point-like source (see Figure 22), requiring further future studies.

Subsequent analysis involved the study of the reddening effects from dust within the galaxy (see Section 5). Throughout previous results, we had been assuming a fixed extinction value of $A_V = 0.25$ based purely on inspection when fitting the isochrones to the MS. However, we now wanted to inspection the relevance

of dust extinction within the galaxy and evaluate its real value. To do so, we analyzed the impact of two distinct reddening laws – one associated with the MW diffuse ISM ($R_V = 3.1$), and the other to the SMC bar ($R_V = 2.7$) – on the instrumental response (throughputs) of a series of filters: F225W, F336W and F438W (see Figure 23). After computing the extinction values associated with each filter and evaluating the color excesses, we generated CCDs where we displayed the reddening vectors associated to each law together with I Zw 18’s stellar population and some overlaid isochrones with foreground extinction (see Figure 24). This way, we could analyze the impact of the shift of the stars’ position with respect to the isochrones due to dust effects. For a more precise analysis, we decided to study the CCDs after applying a cut in SN of $SN_{F438W} > 50$ in order to solely account for those stars with the lowest photometric errors. We eventually concluded that the point-like sources were, overall, shifted a value ranging around $A_V \in (0.1, 0.25)$, in agreement with previous assumptions. Although differences were observed with respect to the extinction values across the various spatial regions of the galaxy (see Figure 25), we oversimplified the situation by assuming a rather uniform reddening. Consequently, the diversity of the extinction behavior could be further explored in future work. Finally, although the two reddening laws yielded very similar results in our particular case, incorporating an additional UV filter (i.e. F140LP) in future analysis could help to better distinguish between them.

We finished our project by executing some SFH models for our galaxies through the use of SFERA2.0 (see Section 6). We used this routine with the objective of fitting the observational CMDs associated with I Zw 18, Component C and Populations A and C. After presuming a Kroupa IMF with masses ranging between $(0.2 - 300) M_\odot$, and providing the routine with a pair of metallicity values ($[Fe/H] = -1.5, -1.6$), as well as a series of MIST isochrones covering the range in age for our stellar population ($(10^6 - 10^{7.8})$ yr), the program got initialized by generating some synthetic CMDs through the population of these isochrones with fake stars. Eventually, it took into account the distance modulus of the galaxy ($\mu_0 = 31.30$ mag), the percentage of potential binary systems (30%), an estimate for the extinction within the galaxy – which we assumed to be $A_V = 0.25$ for simplicity purposes, while imposing the MW reddening law – and the completeness and photometric errors inferred from ASTs in order to properly account for the physics inherent in each galaxy. These individual CMD models were divided into 2D grids, together with the observational one, and were latter on weighted and assembled through Eq. 18, generating final CMD configurations estimating the optimal combination of synthetic models that best reproduced the real stars in each cell. During this process, SFERA2.0 – grounded in genetic algorithms that simulate natural selection and involve the introduction of random mutations – tested the different combinations that returned the best fit (best model) based on a minimization technique through a Poissonian likelihood function (see Eq. 19).

Therefore, we reconstructed histograms showing the comparison between the observational CMDs and the best models provided by the framework, as well as the residual structure (see Eq. 20) – highlighting the significant differences between the observed data and the models (see Figures 26 and 27). On average, we observed that the genetic code worked reasonably well although the fits were not ideal. The issue when trying to fit the brightest sources was most pronounced in I Zw 18’s main body due to its heterogeneous stellar density across the FOV, which complicated the completeness corrections. In contrast, Populations A and C seemed less affected by this effect. Additionally, the complex nature of these short-lifespan sources, together with their potential strong stellar winds as mentioned previously, could be further contributing to the discrepancies. Moreover, the age-metallicity degeneracy could also play a relevant role during the model fitting procedure. It could have led to blue, metal-poor stars being confused with younger ones and the other way around with the red, metal-richer sources. This could have made it hard to accurately classify the different stellar populations by color. Reddening could have also challenged the fitting of the reddest sources since we had assumed a rather constant value for all the regions when in reality A_V changed throughout the galaxy and among each point-like source, as previously demonstrated.

Further improvements could have been implemented for a better fit of the observational CMDs. For instance, broadening the metallicity range could have improved the model's effectiveness. Same occurs with the number of initial weights and generations assumed, which could need refinement. Additionally, we saw that CMD inhomogeneities affected the fitting, especially in terms of the binning. However, balancing resolution and ensuring enough stellar counts per cell is a complex task.

We finalized our thesis project by elaborating some SFHs diagrams (see Figure 28), where we evaluated and characterized the star formation evolution within each region. Since the SFRs were derived from the SFERA2.0 routine, the results were also affected by the same effects and parameter selection as mentioned above. However, overall the SFHs within I Zw 18, Component C and Populations A and C where is good agreement with previous studies (Lelli et al. (2012), Bortolini et al. (2024b), and references therein). On the one hand, we observed that both I Zw 18 and Component C followed mild SFRs from around (23.4 – 63) Myr ago. Then, Component C presented a modest burst at around (10 – 23.4) Myr ago, followed by a quiescent period, which aligns perfectly with the moment in which I Zw 18 presents its first remarkable stellar outburst (around (4.5 – 10) Myr ago), followed by its second most recent one (around (1 – 2) Myr ago). This suggests a potential gas transfer from the companion towards the main body, supporting gravitational interaction between both sources. Additionally, I Zw 18's much higher H_I gas density (see Figure 29) together with the HeB spatial distribution analysis carried out before already indicated an "older" population for Component C, which we now demonstrated.

Lastly, when analyzing Populations A and C we confirmed that they encompass the higher SFR regions within I Zw 18. Before 23.4 Myr ago, both regions presented a rather low stellar formation that significantly increased to $\approx 0.04 M_{\odot}/\text{yr}$ in both of them around (10 – 23.4) Myr ago. Later, while the SFR in Population C moderately declined, that of Population A peaked, first around (4.5 – 10) Myr ago with a SFR of $\approx 0.3 M_{\odot}/\text{yr}$ and later around (1 – 2) Myr ago with a SFR of $\approx 0.5 M_{\odot}/\text{yr}$, in agreement with Bortolini et al. (2024b). We also argued that the lack of older stellar populations in Population A compared to Population C could be due to completeness and crowding effects. Additionally, the underestimation of Population A's recent SFR when analyzing I Zw 18's main body as a whole could be intimately related to the failure in accounting for the varying completeness over regions with very different stellar densities.

Before concluding this project, we should mention that all of the above are results influenced by the assumption of a series of parameters. Therefore, they are open to potential improvements in future works, serving as preliminary results for now. More specifically, those obtained during the analysis of the SFHs were somewhat constrained given the limited time available and the use of an externally developed code. Consequently, the SFH results emerged from a rather direct and immediate procedure, contrary to the previous ones presented when analyzing the isochrones and stellar populations, which were the product of iterative refinement processes. Nevertheless, these latter ones were also influenced by assumptions. For instance, we applied the same extinction effects to I Zw 18 and Component C, despite knowing that they presented different properties, simply for a matter of simplicity and time efficiency. It could have also been interesting to detect the brightest sources within I Zw 18 and Component C. Probably, through the execution of spectral energy distribution (SED) fitting techniques, where we could have been able to infer a more precise estimation of the stars' intrinsic properties (i.e. effective temperatures and luminosities), helping us gain knowledge about the youngest, most massive and bluest clump within the galaxies, which had been less accurately fitted before. For all this, we stress the importance of improving and further expanding the results presented throughout this thesis in future studies.

Acknowledgements

In the first place, I would like to express my profound gratitude to Göran Östlin and Giacomo Bortolini – both playing the role of my mentor and co-supervisor, respectively – for their involvement throughout this project. Their willingness to answer my endless questions and to nurture my insatiable desire to learn has been invaluable. I sincerely appreciate your patience and how you have provided me with a foundation that will hopefully shape my future career far beyond this first solid project of mine. Further acknowledgments are given to the collaborators working in the GO program 17129 (PI: G. Östlin), for kindly sharing their progress during the online meetings and always making me feel welcomed.

I would especially like to thank my family and my lifelong friends who, despite the distance and the long-awaited journey of two years, have always supported me, making me feel accompanied and proud of me and my work, no matter what. Namely, I want to thank my mom, my partner Maxi, my sister Paula, and my uncle Luismi. This achievement is as much yours as it is mine since none of this would have been possible without you. Thank you for not letting me give up and for always having faith in me. Lastly, I would like to express my gratitude to my classmates, as well as some of the Ph.D. students with whom I have had the pleasure to cross paths and who now I consider my friends. I truly admire you all. Thank you for your support and kindness on days filled with frustration, for the motivation and helping hand when I needed it the most, and especially for reminding me that taking breaks and resting were necessary too. My heartfelt thanks to each of you.

Appendix

This project is developed as part of the GO 17129 program (PI: Göran Östlin), from which the photometric data was retrieved. `DOLPHOT2.0` software was downloaded with the help of Giacomo Bortolini and executed following his indications, as well as the manual. During the CMD analysis, the estimation of completeness levels and photometric error bars was conducted following Giacomo's code as a technical foundation. The generation of artificial stars was also carried out under the guidance and instructions provided by Giacomo Bortolini, who later on executed the PSF fitting software for their detection. The `SFERA2.0` routine was also provided to me through private communications by Giacomo Bortolini, who also taught me the basic principles behind it and guided me on how to use the codes to carry out the analyses.

All the results shown in this work were computed using a range of analysis tools such as `Python` (with the use of libraries such as `numpy`, `astropy`, `pandas` and `scipy`, among others) and `SAOImageDS9`. Additionally, `TOPCAT` was occasionally employed for rapid, preliminary visualizations rather than for executing final results. Eventually, I was also given access to the cluster `G3` to execute bigger datasets with `DOLPHOT2.0` and `SFERA2.0`. Moreover, the present manuscript was produced using `Overleaf` – an online document editor.

The overall work carried out during this thesis and the consequent conclusions drawn in previous sections were all subject to continuous discussions and revisions, which took place in weekly meetings (and sometimes several times a week) with the two main supervisors (Göran Östlin and Giacomo Bortolini), and occasionally guided by feedback from some members at the Galaxy Group of the Astronomy Department at Stockholm University (SU), as well as from collaborators on the GO 17129 program during online meetings.

References

- Aloisi, A., Clementini, G., Tosi, M., et al. 2007, *The Astrophysical Journal*, 667, L151
- Aloisi, A., Tosi, M., & Greggio, L. 1999, *The Astronomical Journal*, 118, 302
- Anders, E. & Grevesse, N. 1989, *Geochimica et Cosmochimica acta*, 53, 197
- Annibali, F., Cignoni, M., Tosi, M., et al. 2013, *The Astronomical Journal*, 146, 144
- Annibali, F. & Tosi, M. 2022, *Nature Astronomy*, 6, 48
- Armas, M. C., Ramos, A. A., & Socas-Navarro, H. 2020, *Astronomy & Astrophysics*, 643, A142
- Asplund, M., Grevesse, N., Sauval, A. J., Prieto, C. A., & Kiselman, D. 2004, *Astronomy & Astrophysics*, 417, 751
- Asplund, M., Grevesse, N., Sauval, A. J., & Scott, P. 2009, *Annual review of astronomy and astrophysics*, 47, 481
- Bertolini, G., Cignoni, M., Sacchi, E., et al. 2024a, *Monthly Notices of the Royal Astronomical Society*, 527, 5339
- Bertolini, G., Östlin, G., Habel, N., et al. 2024b, *Astronomy & Astrophysics*, 689, A146
- Bressan, A., Marigo, P., Girardi, L., et al. 2012, *Monthly Notices of the Royal Astronomical Society*, 427, 127
- Charbonneau, P. 1995, *Astrophysical Journal Supplement* v. 101, p. 309, 101, 309
- Chen, Y., Girardi, L., Fu, X., et al. 2019, *Astronomy & Astrophysics*, 632, A105
- Chiappini, C., Hirschi, R., Meynet, G., et al. 2006, *Astronomy & Astrophysics*, 449, L27
- Choi, J., Dotter, A., Conroy, C., et al. 2016, *The Astrophysical Journal*, 823, 102
- Chromey, F. R. 2016, *To measure the sky: an introduction to observational astronomy* (Cambridge University Press)
- Cignoni, M., Sabbi, E., Nota, A., et al. 2009, *The Astronomical Journal*, 137, 3668
- Cignoni, M., Sabbi, E., Van Der Marel, R., et al. 2016, *The Astrophysical Journal*, 833, 154
- Cignoni, M., Sabbi, E., Van Der Marel, R., et al. 2015, *The Astrophysical Journal*, 811, 76
- Cignoni, M., Sacchi, E., Aloisi, A., et al. 2018, *The Astrophysical Journal*, 856, 62
- Cignoni, M., Sacchi, E., Tosi, M., et al. 2019, *The Astrophysical Journal*, 887, 112
- Cignoni, M. & Tosi, M. 2010, *Advances in Astronomy*, 2010, 158568
- Cimatti, A., Fraternali, F., & Nipoti, C. 2019, *Introduction to galaxy formation and evolution: from primordial gas to present-day galaxies* (Cambridge University Press)
- Colling, C., Hennebelle, P., Geen, S., Iffrig, O., & Bournaud, F. 2018, *Astronomy & Astrophysics*, 620, A21
- Crowther, P. A. 2007, *Annu. Rev. Astron. Astrophys.*, 45, 177
- Diehl, R., Korn, A., Leibundgut, B., Lugaro, M., & Wallner, A. 2022, *Progress in Particle and Nuclear Physics*, 127, 103983

- Dolphin, A. 2016, Astrophysics Source Code Library, ascl
- Dolphin, A. E. 2000, Publications of the Astronomical Society of the Pacific, 112, 1383
- Dotter, A. 2016, The Astrophysical Journal Supplement Series, 222, 8
- Draine, B. T. 2011, Physics of the interstellar and intergalactic medium, Vol. 19 (Princeton University Press)
- Dufour, R. J. & Hester, J. J. 1990, Astrophysical Journal, Part 1 (ISSN 0004-637X), vol. 350, Feb. 10, 1990, p. 149-154., 350, 149
- Ferrara, A. 2016, Understanding the Epoch of Cosmic Reionization, 163
- Frenk, C. S., White, S. D., Davis, M., & Efstathiou, G. 1988, Astrophysical Journal, Part 1 (ISSN 0004-637X), vol. 327, April 15, 1988, p. 507-525. Research supported by the Nuffield Foundation and SERC., 327, 507
- Garnett, D., Skillman, E., Dufour, R., & Shields, G. 1997, The Astrophysical Journal, 481, 174
- Geller, R. M., Freedman, R. A., & Kaufmann, W. J. 2019, Universe (Macmillan International Higher Education)
- Giallongo, E., Grazian, A., Fiore, F., et al. 2015, Astronomy & Astrophysics, 578, A83
- Goswami, S., Silva, L., Bressan, A., et al. 2022, Astronomy & Astrophysics, 663, A1
- Heasley, J. N. 1999, in Astronomical Society of the Pacific Conference Series, Vol. 189, Precision CCD Photometry, ed. E. R. Craine, D. L. Crawford, & R. A. Tucker
- Hirschauer, A. S., Crouzet, N., Habel, N., et al. 2024, The Astronomical Journal, 168, 23
- Hopkins, P. F., Quataert, E., & Murray, N. 2012, Monthly Notices of the Royal Astronomical Society, 421, 3522
- Hunter, D. A. & Thronson Jr, H. A. 1995, Astrophysical Journal v. 452, p. 238, 452, 238
- Izotov, Y., Thuan, T., Guseva, N., & Liss, S. 2018, Monthly Notices of the Royal Astronomical Society, 473, 1956
- Izotov, Y. I., Foltz, C. B., Green, R. F., Guseva, N. G., & Thuan, T. X. 1997, The Astrophysical Journal, 487, L37
- Izotov, Y. I. & Thuan, T. X. 2004, The Astrophysical Journal, 616, 768
- Jang, I. S. 2023, Monthly Notices of the Royal Astronomical Society, 521, 1532
- Kaur, K. P. & Joshi, P. S. 2022, arXiv preprint arXiv:2209.03015
- Kravtsov, A. V., Gnedin, O. Y., & Klypin, A. A. 2004, The Astrophysical Journal, 609, 482
- Kroupa, P. 2002, Science, 295, 82
- Kunth, D. & Östlin, G. 2000, The Astronomy and Astrophysics Review, 10, 1
- Lamers, H. J. 2005, Proceedings of the International Astronomical Union, 1, 303
- Lebouteiller, V., Heap, S., Hubeny, I., & Kunth, D. 2013, Astronomy & Astrophysics, 553, A16
- Legrand, F. 1999, arXiv preprint astro-ph/9912115
- Legrand, F., Kunth, D., Roy, J., Mas-Hesse, J., & Walsh, J. 2000, arXiv preprint astro-ph/0001302

- Legrand, F., Kunth, D., Roy, J.-R., Mas-Hesse, J., & Walsh, J. 1997, arXiv preprint astro-ph/9707279
- Legrand, F., Tenorio-Tagle, G., Silich, S., Kunth, D., & Cerviño, M. 2001, *The Astrophysical Journal*, 560, 630
- Lelli, F., Verheijen, M., & Fraternali, F. 2014, *Monthly Notices of the Royal Astronomical Society*, 445, 1694
- Lelli, F., Verheijen, M., Fraternali, F., & Sancisi, R. 2012, *Astronomy & Astrophysics*, 537, A72
- Limongi, M. n.d., Lecture slides, private communication. INAF, Rome
- Longair, M. 2008, *Galaxy Formation* (Springer Berlin, Heidelberg)
- Mac Low, M.-M. & Ferrara, A. 1999, *The Astrophysical Journal*, 513, 142
- Mariño, P. 2001, *Astronomy & Astrophysics*, 370, 194
- Mateo, M. 1998, *Annual Review of Astronomy and Astrophysics*, 36, 435
- McClure-Griffiths, N. M., Stanimirović, S., & Rybczak, D. R. 2023, *Annual Review of Astronomy and Astrophysics*, 61, 19
- Östlin, G. 2000, *The Astrophysical Journal*, 535, L99
- Pearson, W., Wang, L., Alpaslan, M., et al. 2019, *Astronomy & Astrophysics*, 631, A51
- Petrosian, A., Boulesteix, J., Comte, G., Kunth, D., & Coarer, E. L. 1996, arXiv preprint astro-ph/9612079
- Petrosian, A., Comte, G., Boulesteix, J., et al. 1995, *Astrophysics*, 38, 335
- Ramos, R. C., Annibali, F., Fiorentino, G., et al. 2011, *The Astrophysical Journal*, 739, 74
- Sacchi, E., Aloisi, A., Correnti, M., et al. 2021, *The Astrophysical Journal*, 911, 62
- Sacchi, E., Cignoni, M., Aloisi, A., et al. 2018, *The Astrophysical Journal*, 857, 63
- Sánchez Almeida, J., Elmegreen, B. G., Muñoz-Tunón, C., & Elmegreen, D. M. 2014, *The Astronomy and Astrophysics Review*, 22, 1
- Sargent, W. L. & Searle, L. 1970, *Astrophysical Journal*, vol. 162, p. L155, 162, L155
- Schlafly, E. F. & Finkbeiner, D. P. 2011, *The Astrophysical Journal*, 737, 103
- Searle, L. & Sargent, W. 1972, *Astrophysical Journal*, vol. 173, p. 25, 173, 25
- Shenar, T., Gilkis, A., Vink, J., Sana, H., & Sander, A. 2020, *Astronomy & Astrophysics*, 634, A79
- Simon, J. D. & Geha, M. 2007, *The Astrophysical Journal*, 670, 313
- Skillman, E. & Kennicutt, R. 1993, *Astrophysical Journal-Part 1 (ISSN 0004-637X)*, vol. 411, no. 2, p. 655-666., 411, 655
- Smith, B., Sigurdsson, S., & Abel, T. 2008, *Monthly Notices of the Royal Astronomical Society*, 385, 1443
- Stahler, S. W. & Palla, F. 2008, *The formation of stars* (John Wiley & Sons)
- Steffen, M., Prakapavičius, D., Caffau, E., et al. 2015, *Astronomy & Astrophysics*, 583, A57
- Stonkutė, R. & Vansevičius, V. 2015, *Open Astronomy*, 24, 314
- Thilker, D. A., Whitmore, B. C., Lee, J. C., et al. 2022, *Monthly Notices of the Royal Astronomical Society*, 509, 4094

- Tokunaga, A. & Vacca, W. 2005, Publications of the Astronomical Society of the Pacific, 117, 1459
- Tolstoy, E. 2009, Proceedings of the International Astronomical Union, 5, 119
- Tosi, M., Greggio, L., Marconi, G., & Focardi, P. 1991, Astronomical Journal (ISSN 0004-6256), vol. 102, Sept. 1991, p. 951-974., 102, 951
- Valluri, M. & Anupama, G. 1996, arXiv preprint astro-ph/9607138
- van Zee, L., Westpfahl, D., & Haynes, M. P. 1998, The Astronomical Journal, 115, 1000
- Vink, J. S. & de Koter, A. 2005, Astronomy & Astrophysics, 442, 587
- Weistrop, D., Hintzen, P., Liu, C., et al. 1995, Astronomical Journal (ISSN 0004-6256), vol. 109, no. 3, p. 981-989, 109, 981
- Weisz, D. R., Dolphin, A. E., Savino, A., et al. 2024, The Astrophysical Journal Supplement Series, 271, 47
- Wheeler, J. C., Sneden, C., & Truran Jr, J. W. 1989, IN: Annual review of astronomy and astrophysics. Volume 27 (A90-29983 12-90). Palo Alto, CA, Annual Reviews, Inc., 1989, p. 279-349., 27, 279
- White, S. D. & Frenk, C. S. 1991, Astrophysical Journal, Part 1 (ISSN 0004-637X), vol. 379, Sept. 20, 1991, p. 52-79. Research supported by NASA, NSF, and SERC., 379, 52
- White, S. D. & Rees, M. J. 1978, Monthly Notices of the Royal Astronomical Society, 183, 341
- Williams, B. F., Lang, D., Dalcanton, J. J., et al. 2014, The Astrophysical Journal Supplement Series, 215, 9
- Woosley, S. & Heger, A. 2006, The Astrophysical Journal, 637, 914
- Woosley, S. E., Heger, A., & Weaver, T. A. 2002, Reviews of modern physics, 74, 1015
- Yoon, S.-C., Langer, N., & Norman, C. 2006, Astronomy & Astrophysics, 460, 199
- Zwicky, F. 1965, Astrophysical Journal, vol. 142, p. 1293, 142, 1293
- Zwicky, F. 1966, Astrophysical Journal, vol. 143, p. 192, 143, 192
- Zwicky, F. & Zwicky, M. 1971, Catalogue of selected compact galaxies and of post-eruptive galaxies (Cite-seer)